

## Chapter 7

# Rod, Beam, Plate and Shell Models

Chapters 2–6 focus on the development of models which characterize both the approximately linear low drive behavior and the nonlinear and hysteretic high drive properties of ferroelectric, relaxor ferroelectric, ferromagnetic and shape memory alloy compounds. In this chapter, we employ the linear and nonlinear constitutive relations to construct distributed models for wire, rod, beam, plate and shell-like structures arising in smart material applications. To motivate issues associated with model development, we summarize several applications detailed in Chapter 1 in terms of these five structural classes.

### Shells

Shells comprise the most general structural class that we consider and actually subsume the other material classes. A fundamental attribute of shell-like structures is the property that in-plane and out-of-plane motion are coupled due to curvature. This adds a degree of complexity and yields systems of coupled equations in resulting models.

Several applications from Chapter 1 which exhibit shell behavior are summarized in Figure 7.1. The cylindrical actuator employed as an AFM stage is wholly comprised of PZT whereas the cylindrical shell employed as a prototype for noise control in a fuselage is constructed from aluminum with surface-mounted PZT patches utilized as actuators and possible sensors. Whereas both involve cylindrical geometries, the latter requires that models incorporate the piecewise inputs and changes in material properties associated with the patches. The THUNDER transducer and SMA-driven chevron involve more general shells having noncylindrical reference surfaces. THUNDER transducers constructed with wide PZT patches have a doubly-curved final geometry due to the mismatch in thermal properties of the PZT and steel or aluminum backing material. Within the region covered by the patch, the device exhibits an approximately constant radius of curvature in the coordinate directions whereas the uncovered tabs remain flat. The geometry of the chevron is even more complex and is ultimately governed by the design of the underlying jet engine.

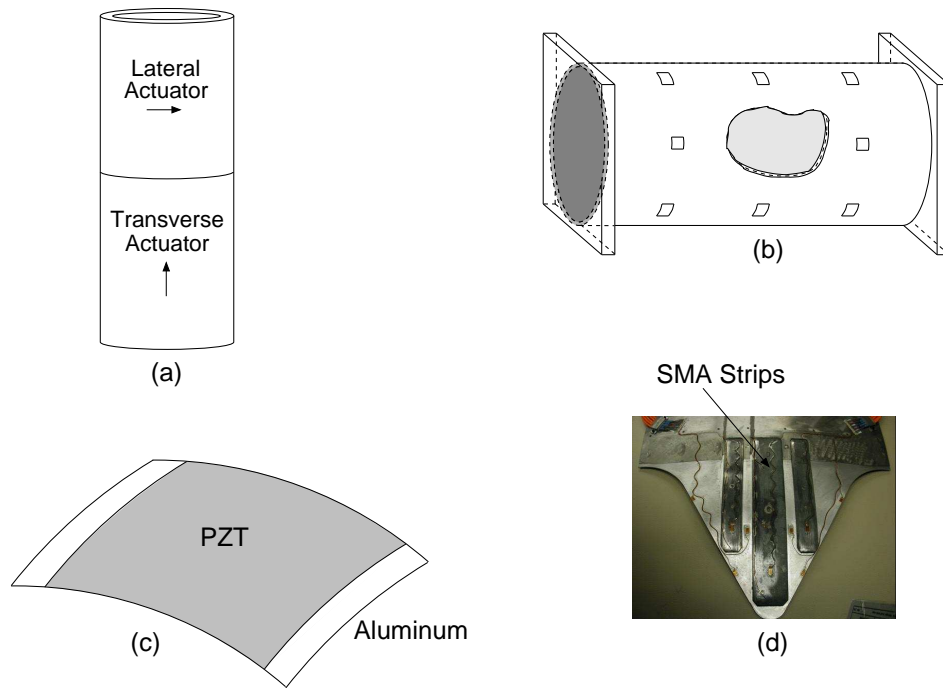


**Figure 7.1.** (a) Cylindrical PZT actuator employed for nanopositioning in an atomic force microscope (AFM). (b) Structural acoustic cavity used as a prototype for noise control in a fuselage. (c) THUNDER transducer considered for flow control, synthetic jets and high speed valve design. (d) SMA-driven chevron employed to reduce jet noise and decrease drag.

For the drive levels employed in the structural acoustic application, linear approximations to the  $E$ - $\varepsilon$  behavior prove sufficiently accurate and models are constructed using the linear constitutive relations developed in Section 2.2. Present AFM designs with cylindrical stages also use linear constitutive relations with robust feedback laws employed to mitigate hysteresis and creep. This proves successful at low drive frequencies but the push to very high drive frequencies for applications involving real-time product diagnostics or biological monitoring has spawned research focused on model-based control design in a manner which accommodates the inherent hysteresis. Finally, the nonlinear and hysteretic behavior illustrated in Figures 1.6 and 1.23 demonstrate that nonlinear models are required to achieve the high drive capabilities of THUNDER transducers and SMA-drive chevrons.

### Plates

Plates can be interpreted as shells having infinite radius of curvature — equivalently, zero curvature — and hence they comprise a special class of shell structures. Thus plate models can be employed as an approximation for shells when the curvature is negligible or for characterizing inherently flat structures whose width is

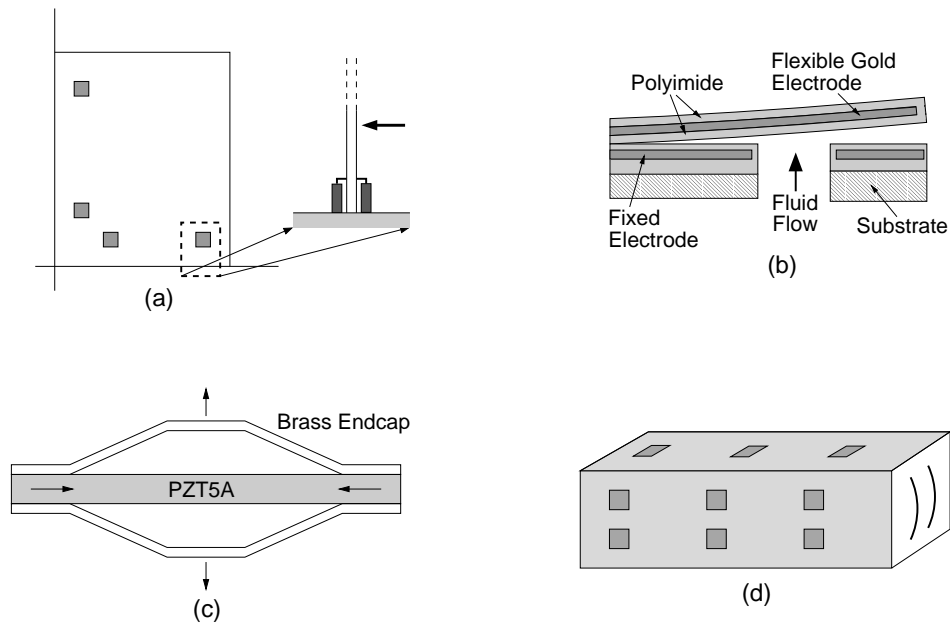


**Figure 7.2.** (a) Control of a plate using Terfenol-D transducers as a prototype for general vibration control. (b) Cross-section of the MEMs actuator depicted in Figure 1.27 for microfluidic control and (c) cross-section of the PZT cymbal actuator depicted in Figure 1.7. (d) PZT patches employed for attenuating structure-borne noise in a duct.

significant compared with the length. For flat plate structures that are symmetric through the thickness, in-plane and out-of-plane motion are inherently decoupled which simplifies both the formulation and approximation of resulting models.

Several smart material applications involving plate-like structures are depicted in Figure 7.2. Because plates incorporate 2-D behavior while avoiding curvature-induced coupling between in-plane and out-of-plane motion, they provide an intermediate level prototype for formulating and testing vibration reduction or control strategies as depicted for magnetostrictive transducers in Figure 7.2(a). The MEMs and cymbal actuators in (b) and (c) typically have widths that are significant when compared with the length and hence exhibit plate-like dynamics. The structural acoustic system depicted in Figure 7.2(d) is analogous to its cylindrical counterpart in Figure 7.1(a) and is employed as a prototype for flat ducts.

As with shells, these applications involve PZT, Terfenol-D, and potentially PMN and SMA, operating in both linear and highly nonlinear and hysteretic regimes. It will be shown in subsequent sections that the same kinematic equations can be employed in both cases, with the linear or nonlinear constitutive behavior incorporated through the models developed in Chapters 2–6.

**Membranes**

Membranes are a special case of shell or plate constructs in which stiffness effects are approximated in various senses or are considered negligible. Hence the resulting models are generalized 2-D analogues of familiar 1-D string models.

Due to their thinness, several of the semicrystalline, amorphous, and ionic polymers discussed in Section 1.5 yield structures that exhibit membrane behavior. To illustrate, consider the use of ionic polymers for biological or chemical detection or PVDF for membrane mirror design as depicted in Figure 7.3. A third example is provided by the SMA films and membranes discussed in Section 1.4 for use in MEMS and biomedical applications. In all three cases, membrane models which incorporate constitutive nonlinearities and hysteresis are necessary for device characterization. It is expected that as the focus on polymers and SMA thin films continues to grow, an increasing number of smart material systems will be characterized by linear and nonlinear membrane models.

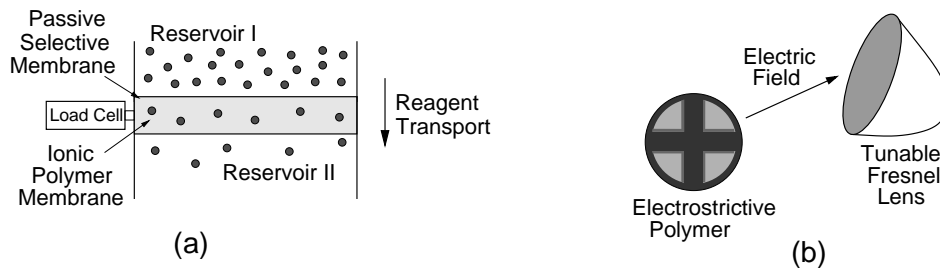


**Figure 7.3.** (a) Chemical detection using chemical-specific permeable ionic polymer membranes. (b) Membrane mirror constructed from PVDF.

**Beams**

Beams comprise a subset of shells and plates whose widths are small compared with lengths. This permits motion in the width direction to be neglected which reduces the dimensionality of models.

Some smart material applications involving flat and curved beam dynamics are depicted in Figure 7.4. The thin beam depicted in Figure 7.4(a) provides a theoretical, numerical and experimental prototype for model development and control design as well as a technological prototype for evolving unimorph designs. The polymer unimorph depicted in Figure 7.4(b) is presently being considered for applications ranging from pressure sensing to flow control and it represents a geometry where the reference surface differs from the middle surface [122]. The THUNDER transducer in Figure 7.4(c) exhibits negligible curvature or motion in the width direction and hence is modeled by curved beam relations in the region covered by PZT coupled with a flat beam model for the tabs. As noted in Section 1.5, the electrostrictive MEMS device depicted in Figure 7.4(d) is being investigated for use in electrical relays and switches, optical and infrared shutters, and microfluidic valves.

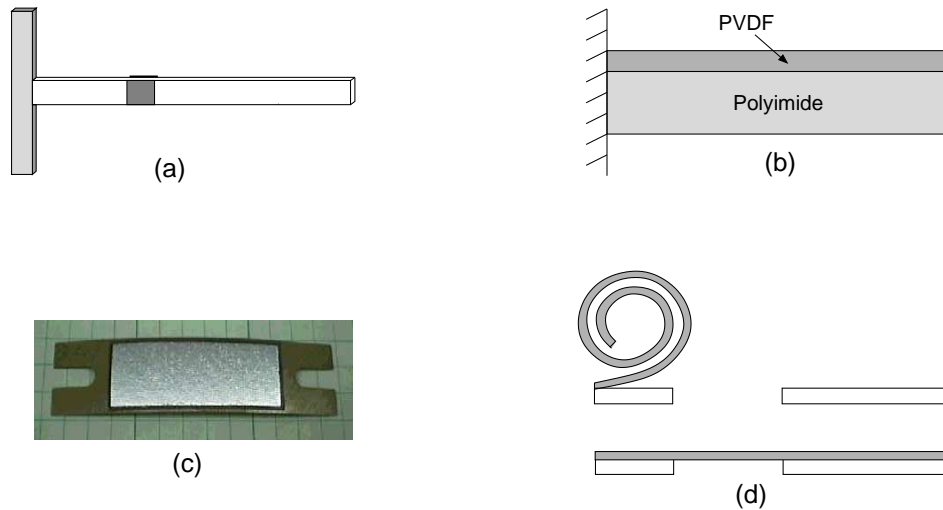


**Figure 7.4.** (a) Thin beam with surface-mounted PZT patches employed as a prototype for vibration control. (b) Polymer unimorph comprised of PVDF and polyimide presently considered for pressure sensing and flow control. (c) Curved THUNDER transducer whose width is small compared with the length. (d) Electrostrictive MEMs actuator employed as a high speed shutter.

As with shells and plates, both linear and nonlinear input behavior must be accommodated in the constitutive relations. Furthermore, both the THUNDER and MEMs actuators can exhibit very large displacements in certain drive regimes. This necessitates consideration of nonlinear kinematic models which incorporate both high-order strain-displacement terms and consider force and moment balancing in the context of the deformed reference line.

### Rods

In both beams and rods, motion is considered with respect to the reference or neutral line and hence models are 1-D. The difference is that beams exhibit out-of-plane motion whereas rod dynamics are solely in-plane. From the perspective of model development, beam models are constructed using both moment and force balancing whereas in-plane force balancing is required when constructing rod models. Due to the geometric coupling associated with curved beams, resulting models have a rod component quantifying in-plane dynamics. We summarize here several smart material applications which solely exhibit rod dynamics without the bending (transverse or out-of-plane) motion associated with beams.

PZT, SMA, and magnetostrictive transducers employed in rod configurations are depicted in Figure 7.5. The stacked PZT actuators employed as  $x$ - and  $y$ -stages in atomic force microscopes (AFM) provide the highly repeatable set point placement required for positioning the sample to within nanometer accuracy. In this configuration,  $d_{33}$  or in-plane motion is utilized thus motivating the development of rod models having boundary conditions commensurate with the device design. As

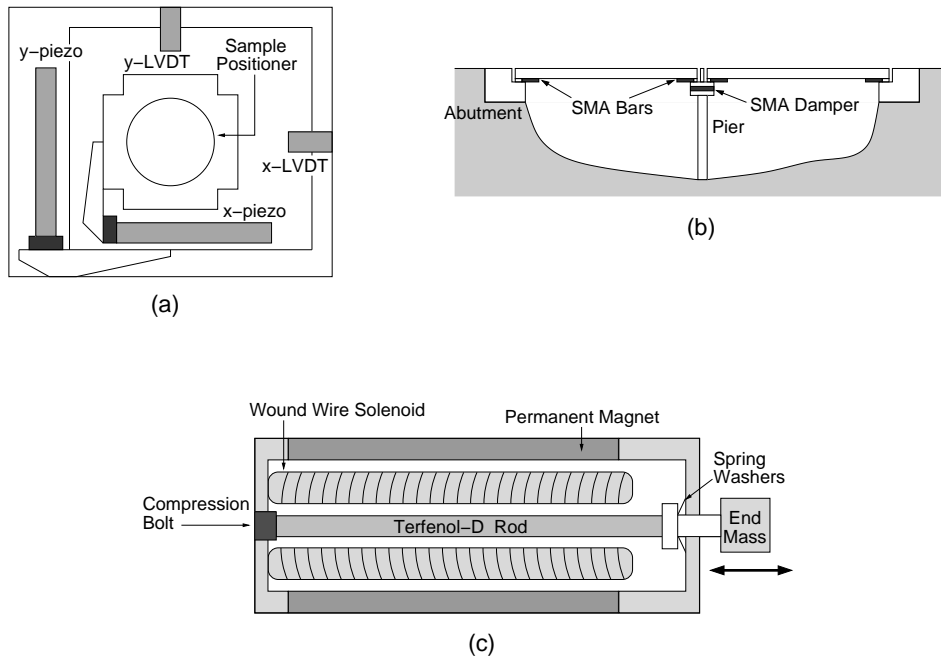


**Figure 7.5.** (a) Stacked PZT actuator employed as  $x$ - and  $y$ -stages in an AFM. (b) SMA bars to reduce lateral displacements in a bridge and (c) cross-section of a magnetostrictive transducer employing a Terfenol-D rod.

illustrated in Figure 1.10, the field-displacement relation exhibits hysteresis which is incorporated via the constitutive relations developed in Chapter 2.

The SMA rod employed to reduce displacements and vibrations in bridge abutments relies on energy dissipated in the pseudoelastic phase and hence is designed for maximal hysteresis. In this case, the constitutive relations from Chapter 5 are used to quantify the  $\sigma$ - $\varepsilon$  behavior when constructing rod models.

Finally, present magnetostrictive transducer designs employ field inputs to a solenoid to rotate moments and produce in-plane motion in a Terfenol-D rod. This produces significant force capabilities but necessitates the use of the constitutive relations developed in Chapter 4 to incorporate the hysteresis and constitutive nonlinear shown in Figure 1.13.

### Wires and Tendons

The final structural family that we mention are wires or tendons. Like rods, the wire motion under consideration is due to in-plane forces or stresses. The difference lies in the property that unlike rods, wires maintain their geometry only when subjected to tensile stresses — compressive stresses cause them to crumple in the manner depicted in Figure 5.7.

In present smart material systems, wires or tendons occur primarily in SMA constructs, but there they are very common. Two prototypical examples illustrat-

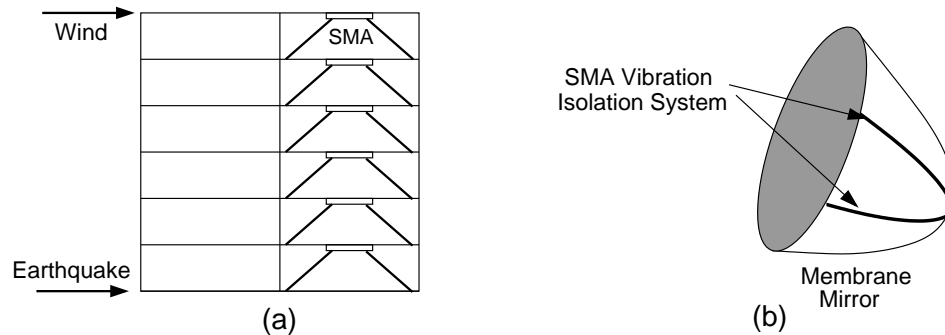


**Figure 7.6.** (a) SMA tendons to attenuate earthquake or wind-induced vibrations in a building and (b) SMA tendons for vibration suppression in a membrane mirror.

ing their use for vibration attenuation in civil or aerospace structures are illustrated in Figure 7.6. In both cases, maximal energy dissipation occurs when the design ensures maximal pseudoelastic hysteresis loops thus necessitating the use of non-linear constitutive relations when constructing distributed models. As detailed in Section 1.4, SMA wires and tendons exploiting the shape memory effect (SME) are presently employed in numerous biomedical applications including orthodontics and catheters, and are under consideration for a wide range of future biomedical, aeronautic, aerospace and industrial applications. A crucial component necessary for the continued developed of SMA devices is the formulation and efficient numerical approximation of distributed models which accommodate the inherent hysteresis and constitutive nonlinearities.

### Model Hierarchies

The cornerstones of distributed wire, rod, beam, plate and shell models are the linear and nonlinear constitutive relations developed in Chapters 2–6 and we summarize these in Section 7.1 as a prelude to subsequent model development. In Section 7.2, we summarize the four assumptions established by Love which provide the basis for constructing linear moment and force relations and strain-displacement relations.

When constructing distributed models for the various structural classes, there are several strategies. The first is to develop the models in a hierarchical manner starting with the simplest case of rods and finishing with shells. Alternatively, one can employ the fact that shell models subsume the other classes and consider first this very general regime — rod, beam and plate models then follow as special cases. The latter strategy emphasizes the unified nature of the development but obscures the details. For clarity, we thus employ a third strategy. We consider the development of rod models in Section 7.3 from both Newtonian and Hamiltonian perspectives. This illustrates the use of the linear and nonlinear constitutive relations from Chapters 2–6 when constructing distributed models from force balance or energy principles. In Sections 7.4 and 7.5, we summarize the development of flat beam and plate models to illustrate the manner through which moment balancing

yields fourth-order models. The coupling between in-plane and out-of-plane motion, inherent to curved structures are addressed in Section 7.6 in the context of general shell models. Special cases, which include cylindrical shells and curved beams are addressed in Section 7.7. Additionally, we summarize the manner in which the general shell framework encompasses rod, beam, and plate models. In Section 7.8, we relax the Love criteria to obtain linear Timoshenko and Mindlin-Reissner models and nonlinear von Kármán relations. The chapter concludes with the formulation of an abstract analysis framework in Section 7.9. Numerical approximation techniques for various structural models are presented in Chapter 8.

## 7.1 Linear and Nonlinear Constitutive Relations

The linear and nonlinear constitutive relations developed in previous chapters provide the basis for incorporating the coupled and typically nonlinear hysteretic behavior inherent to ferroelectric, ferromagnetic and shape memory alloy compounds. We summarize relevant constitutive relations as a prelude to distributed model development in later sections.

### 7.1.1 Ferroelectric and Relaxor Ferroelectric Materials

We summarize linear constitutive relations developed in Section 2.2 and nonlinear hysteretic relations resulting from the homogenized energy framework of Section 2.6. Additional nonlinear relations resulting from Preisach and domain wall theory can be found in Sections 2.4 and 2.5.

#### Linear Constitutive Relations

For low drive regimes, linear constitutive relations for 1-D and 2-D geometries were summarized in Section 2.2.5. We summarize the relations for voltage inputs derived through the approximation  $V = EL$  where  $L$  denotes the distance through which the field is propagated. For  $d_{31}$  motion,  $L = h$  is the thickness of the actuator whereas  $L = \ell$  is the actuator length for  $d_{33}$  inputs. Note that linear constitutive relations for alternative input variables can be found in Tables 2.1 and 2.2.

#### 1-D Relations: Beams

Damped linear constitutive relations appropriate for beam models are

$$\begin{aligned}\sigma &= Y\varepsilon + c\dot{\varepsilon} - Y\frac{d_{31}}{h}V \\ P &= Yd_{31}\varepsilon + \chi\frac{V}{h}\end{aligned}\tag{7.1}$$

where  $Y$  and  $c$  denote the Young's modulus and Kelvin-Voigt damping coefficients and  $\chi$  is the dielectric susceptibility.

#### 1-D Relations: Rods

Rods employ  $d_{33}$  inputs so one employs  $\frac{d_{33}}{\ell}$  rather than  $\frac{d_{31}}{h}$  in the converse relation.

*2-D Relations: General Shells*

For general shell models, we let  $\varepsilon_\alpha, \sigma_\alpha$  and  $\varepsilon_\beta, \sigma_\beta$  denote normal strains and stresses in the  $\alpha$  and  $\beta$  directions and let  $\varepsilon_{\alpha\beta}, \sigma_{\alpha\beta}$  denote shear strains and stresses. The Poisson ratio is denoted by  $\nu$ . Linear constitutive relations for this regime are

$$\begin{aligned} \sigma_\alpha &= \frac{Y}{1-\nu^2}(\varepsilon_\alpha + \nu\varepsilon_\beta) + \frac{c}{1-\nu^2}(\dot{\varepsilon}_\alpha + \nu\dot{\varepsilon}_\beta) - \frac{Yd_{31}}{1-\nu} \frac{V}{h} \\ \sigma_\beta &= \frac{Y}{1-\nu^2}(\varepsilon_\beta + \nu\varepsilon_\alpha) + \frac{c}{1-\nu^2}(\dot{\varepsilon}_\beta + \nu\dot{\varepsilon}_\alpha) - \frac{Yd_{31}}{1-\nu} \frac{V}{h} \\ \sigma_{\alpha\beta} &= \frac{Y}{2(1+\nu)}\varepsilon_{\alpha\beta} + \frac{c}{2(1+\nu)}\dot{\varepsilon}_{\alpha\beta} \\ P &= Yd_{31}\varepsilon + \chi \frac{V}{h} \end{aligned} \tag{7.2}$$

— see [33] for details. For homogeneous, isotropic materials, electromechanical coupling does not produce significant twisting and hence piezoelectric effects are neglected in the shear relation. Note that  $d_{33}$  effects can be incorporated in the manner described for rods.

*2-D Relations: Cylindrical Shell and Plates*

The relations for cylindrical shells and plates are special cases of (7.2). For cylindrical shells in which  $x$  and  $\theta$  delineate the longitudinal and circumferential coordinates, one employs  $\alpha = x$  and  $\beta = \theta$ . For flat plates, we will use the coordinates  $\alpha = x$  and  $\beta = y$ .

**Nonlinear Constitutive Relations**

As detailed in Section 2.1, constitutive nonlinearities and hysteresis are inherent to the  $E$ - $P$  relation due to dipole rotation and energy dissipation during domain wall movement. Moreover,  $90^\circ$  dipole switching due to certain stress inputs can produce the ferroelastic hysteresis depicted in Figures 2.11 and 2.12. We restrict our discussion to stress levels below the coercive stress  $\sigma_c$  but note that ferroelastic switching must be accommodated in certain high stress regimes — e.g., THUNDER in various configurations exhibits ferroelastic switching. Initial extensions to the theory to incorporate  $90^\circ$  ferroelastic switching are provided in [24].

*1-D Relations: Rods and Beams*

For poled materials operating about the bias polarization  $P_0 = P_R$ , extension of (2.135) to include Kelvin–Voigt damping yields the 1-D constitutive relations

$$\begin{aligned} \sigma &= Y\varepsilon + c\dot{\varepsilon} - a_1(P - P_R) - a_2(P - P_R)^2 \\ [P(E, \varepsilon)](t) &= \int_0^\infty \int_{-\infty}^\infty \nu_1(E_c)\nu_2(E_I)[\bar{P}(E + E_I, \varepsilon; E_c, \xi)](t) dE_I dE_c \end{aligned} \tag{7.3}$$

where  $\nu_1$  and  $\nu_2$  are densities satisfying the conditions (2.113). For moderate strain levels, the kernel  $\bar{P}$  is given by (2.89), (2.90) or (2.99) whereas the relations in Section 2.6.9 can be employed if strains are significant. The elastic constitutive relation incorporates both linear piezoelectric and quadratic electrostrictive effects and hence characterizes a broad range of ferroelectric and relaxor ferroelectric behavior. Furthermore, the coefficients  $a_1$  and  $a_2$  can be chosen to incorporate either the longitudinal or transverse inputs analogous to  $d_{33}$  or  $d_{31}$  inputs in linear regimes. Finally, we note that one can employ more general bias polarizations  $P_0$ , including  $P_0 = 0$ , if operating about points other than the remanence.

**Remark 7.1.1.** *The inclusion of strain behavior in the polarization model yields nonlinear stress-strain relations and hence will yield distributed models having a nonlinear state-dependence. For actuator applications, the strain-dependence in  $\bar{P}$  and hence  $P$  is typically small compared with the field-dependence and is generally neglected — this yields constitutive relations and distributed models have a linear state-dependence but a nonlinear and hysteretic input-dependence. For sensor applications, this direct effect is retained to incorporate the effects of  $\varepsilon, \sigma$  on  $E, P$  or  $V$ .*

### 2-D Relations: Shells

The development of constitutive relations for shells combines the linear elastic relations (7.2) and nonlinear inputs from (7.3). For  $\tilde{P} = P - P_R$ , this yields

$$\begin{aligned} \sigma_\alpha &= \frac{Y}{1-\nu^2}(\varepsilon_\alpha + \nu\varepsilon_\beta) + \frac{c}{1-\nu^2}(\dot{\varepsilon}_\alpha + \nu\dot{\varepsilon}_\beta) - \frac{1}{1-\nu} \left[ a_1\tilde{P} + a_2\tilde{P}^2 \right] \\ \sigma_\beta &= \frac{Y}{1-\nu^2}(\varepsilon_\beta + \nu\varepsilon_\alpha) + \frac{c}{1-\nu^2}(\dot{\varepsilon}_\beta + \nu\dot{\varepsilon}_\alpha) - \frac{1}{1-\nu} \left[ a_1\tilde{P} + a_2\tilde{P}^2 \right] \\ \sigma_{\alpha\beta} &= \frac{Y}{2(1+\nu)}\varepsilon_{\alpha\beta} + \frac{c}{2(1+\nu)}\dot{\varepsilon}_{\alpha\beta} \end{aligned} \tag{7.4}$$

$$[P(E, \varepsilon)](t) = \int_0^\infty \int_{-\infty}^\infty \nu_1(E_c)\nu_2(E_I)[\bar{P}(E + E_I, \varepsilon; E_c, \xi)](t) dE_I dE_c$$

where  $\alpha = x, \beta = \theta$  for cylindrical shells and  $\alpha = x, \beta = y$  for flat plates.

## 7.1.2 Ferromagnetic Materials

The development of constitutive relations for ferromagnetic materials is analogous to that for ferroelectric compounds and we summarize here only the 1-D relations employed for rod models.

### Linear Constitutive Relations

Linear constitutive relations formulated in terms of the input variable pair  $(\varepsilon, H)$  can be obtained by posing the elastic relation in (4.23) as a function of  $\varepsilon$

or by employing a magnetic Gibbs energy relation analogous to the electric Gibbs energy in Table 2.1 of Section 2.2. Inclusion of Kelvin–Voigt damping yields

$$\begin{aligned}\sigma &= Y\varepsilon + c\dot{\varepsilon} - aM \\ M &= Yd_{31}\varepsilon + \chi H\end{aligned}\tag{7.5}$$

where  $\chi$  is the magnetic susceptibility. These piezomagnetic relations should be employed only in low to moderate drive regimes where hysteresis and quadratic magnetostrictive effects are negligible.

### Nonlinear Constitutive Relations

For the homogenized energy model, incorporation of Kelvin–Voigt damping, operation about a bias magnetization  $M_0$  — which can be the remanence value  $M_R$  — and inclusion of linear  $\sigma$ - $M$  behavior in (4.96) yields the constitutive relations

$$\begin{aligned}\sigma &= Y\varepsilon + c\dot{\varepsilon} - a_1(M - M_0) - a_2(M - M_0)^2 \\ [M(H)](t) &= \int_0^\infty \int_{-\infty}^\infty \nu_1(H_c)\nu_2(H_I)[\overline{M}(H + H_I; \varepsilon, H_c, \xi)](t) dH_I dH_c.\end{aligned}\tag{7.6}$$

Here  $\xi$  denotes the initial moment distribution and the kernel  $\overline{M}$  is given by (4.71), (4.72) or (4.78). As noted in Remark 7.1.1, the general kernel depends on  $\varepsilon$ , thus producing nonlinear constitutive relations and nonlinear rod models. For actuator models, this direct effect can be neglected since it is small compared with the field-dependence.

We note that if employing the Preisach or Jiles–Atherton models, one would replace the  $H$ - $M$  model in (7.6) by (4.34) or (4.62).

### 7.1.3 Shape Memory Alloys

Like ferroelectric and ferromagnetic compounds, the constitutive behavior of shape memory alloys can be characterized through a number of techniques including high-order polynomials which quantify the inherent first-order transition behavior, Preisach models, domain wall theory, and homogenized free energy theory. The use of polynomial-based stress-strain relations to derive a 1-D distributed model for an SMA rod was illustrated in Section 5.2.1 with details given in [57]. We summarize here the macroscopic homogenized energy relations from Section 5.5 and we refer the reader to Chapter 5 for details regarding the other theories.

For densities  $\nu_1$  and  $\nu_2$  satisfying the decay criteria (5.27), the dependence of strains on stresses and temperature is quantified by (5.26),

$$[\varepsilon(\sigma, T)](t) = \int_0^\infty \int_{-\infty}^\infty \nu_1(\sigma_R)\nu_2(\sigma_I)[\overline{\varepsilon}(\sigma + \sigma_I, T; \sigma_R, \xi)](t) d\sigma_I d\sigma_R,\tag{7.7}$$

where  $\sigma_R = \sigma_M - \sigma_A$  denotes the relative stress and the kernel  $\overline{\varepsilon}$  is given by (5.15) or (5.20). The temperature evolution is governed by (5.21).

For a number of 1-D applications, (7.7) can be directly employed to characterize the pseudoelastic behavior and shape memory effects inherent to SMA wires and rods. For applications in which SMA is employed an actuator or is coupled to

an adjacent structure, the relation quantifies the nonlinear and hysteretic constitutive behavior in a manner which can be coupled with structural constitutive relations to construct system models.

## 7.2 Linear Structural Assumptions

Whereas the input-dependence is often nonlinear and hysteretic as characterized by the constitutive relations, classical theory can often be employed when balancing forces and moments, and constructing the strain-displacement relations employed in distributed models. We summarize here four assumptions established by Love which form the foundation of classical shell theory [301] — and hence are fundamental for the subclasses of rods, beams and plates. Relaxation of these assumptions yields the coupled and nonlinear models summarized in Section 7.8.

1. *The shell thickness  $h$  is small compared with the length  $\ell$  and radius of curvature  $R$ .* This permits the development of thin shell models and encompasses a broad range of civil, aerospace, aeronautic, industrial and biomedical structures and devices. As detailed in [145,364], this criterion is generally satisfied if  $h/R < \frac{1}{20}$  to  $\frac{1}{10}$ .
2. *Small deformations.* For small deformations, higher powers in strain-displacement relations can be neglected and kinematic and equilibrium conditions are developed in relation to the unperturbed shell neutral surface. This condition may not hold for large displacements of the type depicted in Figure 1.29 and 7.4 for an electrostatic MEMs actuator. Relaxation of this condition yields the nonlinear von Kármán model summarized in Section 7.8.
3. *Transverse normal stresses  $\sigma_z$  are negligible compared to the normal stresses  $\sigma_\alpha, \sigma_\beta$ .* As detailed in [292], this assumption leads to certain contradictions regarding the retention of stresses but yields models which provide reasonable accuracy for a wide range of applications.
4. *Lines originally normal to the reference or neutral surface remain straight and normal during deformations as depicted in Figure 7.7(a).* This is referred to as the Kirchhoff hypothesis and is a generalization of the Euler hypothesis for thin beams which asserts that plane sections remain plane. For coupled in-plane and out-of-plane motion, this implies that strains  $\varepsilon$  at a point  $z$  in the thickness direction can be expressed as

$$\varepsilon = e + \kappa(z - z_n) \quad (7.8)$$

where  $z_n$  denotes the position of the neutral surface and  $e, \kappa$  are the in-plane strain and curvature changes at the neutral surface as depicted in Figure 7.8. For moderate to thick structures, the relaxation of this hypothesis yields the Timoshenko beam model and Mindlin–Reissner plate model which include rotational effects and shear deformation.

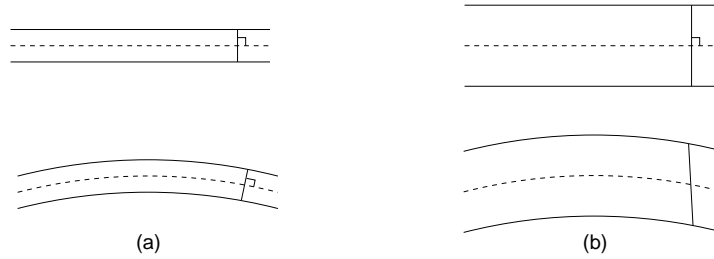


**Figure 7.7.** Behavior of normal lines to the neutral surface during bending. (a) Lines remain normal in thin structures in accordance with Assumption 4 and (b) non-normal response in thick structures due to transverse shear strains.

**Remark 7.2.1.** Through Assumptions 3 and 4, the second-order 3-D elasticity problem is reduced to a 2-D problem formulated in terms of a reference or neutral surface. This yields fourth-order models for the transverse motion and leads to an imbalance with the in-plane relations which remain second-order. However, the efficiency gained by reducing dimensions typically dominates the added complexity associated with approximating the fourth-order relations in weak form.

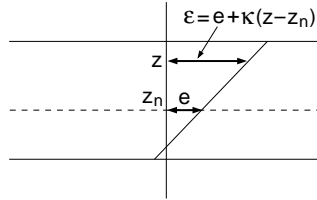


**Figure 7.8.** Strain profile posited by Assumption 4 and comprised of an in-plane component  $e$  and bending component  $\kappa z$ .

### 7.3 Rod Models

To illustrate the construction of distributed models from both Newtonian and Hamiltonian principles, we consider first models which quantify the in-plane dynamics of the rod structures depicted in Figure 7.5. A prototypical geometry comprised of a homogeneous rod of length  $\ell$  and cross-sectional area  $A$  is shown in Figure 7.9. The density, Young's modulus and Kelvin–Voigt damping coefficient are denoted by  $\rho$ ,  $Y$  and  $c$ .<sup>29</sup> The longitudinal displacement in the  $x$ -direction and distributed force per unit length are denoted by  $u$  and  $f$ . Finally, the end at  $x = 0$  is considered fixed whereas we consider a mass  $m_\ell$  and boundary spring with stiffness  $k_\ell$  and

<sup>29</sup>From Tables 1.1 and 4.1 on pages 28 and 165, it is noted that representative Young's moduli for PZT and Terfenol-D are 71 GPa and 110 GPa whereas representative densities are 7600 kg/m<sup>3</sup> and 9250 kg/m<sup>3</sup>. However, parameter values for a specific device, including damping coefficients, are typically estimated through a least squares fit to data.

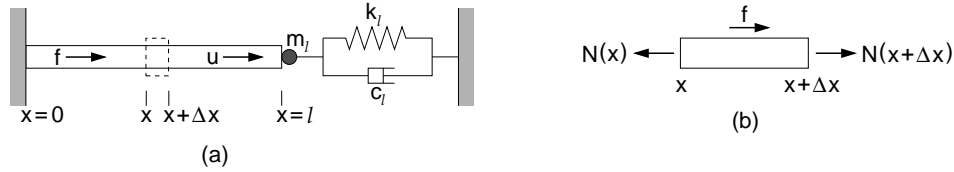


**Figure 7.9.** (a) Rod of length  $l$  and cross-sectional area  $A$  with a fixed end at  $x = 0$  and energy dissipating boundary conditions at  $x = l$ . (b) Infinitesimal element considered when balancing forces.

damping coefficient  $c_l$  at  $x = l$ . The latter incorporates the energy dissipation and mass associated with prestress mechanisms and loads in a Terfenol-D transducer or elastic mechanisms connected to AFM stages.

### 7.3.1 Newtonian Formulation

To quantify the dynamics of the rod, we consider a representative infinitesimal element  $[x, x + \Delta x]$  as depicted in Figure 7.9(b). In-plane force resultants are denoted by  $N(t, x)$  and  $N(t, x + \Delta x)$  where

$$N(t, x) = \int_A \sigma dA = \sigma(t, x)A \quad (7.9)$$

since the rod is assumed uniform and homogeneous.

The balance of forces for the element gives

$$\begin{aligned} \int_x^{x+\Delta x} \rho A \frac{\partial^2 u}{\partial t^2}(t, s) ds &= N(t, x + \Delta x) - N(t, x) + \int_x^{x+\Delta x} f(t, s) ds \\ \Rightarrow \lim_{\Delta x \rightarrow 0} \frac{1}{\Delta x} \int_x^{x+\Delta x} \rho A \frac{\partial^2 u}{\partial t^2}(t, s) ds &= \lim_{\Delta x \rightarrow 0} \frac{N(t, x + \Delta x) - N(t, x)}{\Delta x} \\ &\quad + \lim_{\Delta x \rightarrow 0} \frac{1}{\Delta x} \int_x^{x+\Delta x} f(t, s) ds \end{aligned}$$

which yields

$$\rho A \frac{\partial^2 u}{\partial t^2} = \frac{\partial N}{\partial x} + f \quad (7.10)$$

as a strong formulation of the model. The resultant is evaluated using (7.9) with  $\sigma$  specified by the various linear and nonlinear constitutive relations summarized in Section 7.1.

A necessary step when evaluating these relations is to relate in-plane strains  $\varepsilon$  and the longitudinal displacements  $u$ . For the geometry under consideration, the relation follows directly from the definition of the strain as the displacement relative to the initial length of an infinitesimal element; hence

$$\varepsilon = \lim_{\Delta x \rightarrow 0} \frac{\Delta u}{\Delta x} = \frac{\partial u}{\partial x}. \quad (7.11)$$

### Boundary and Initial Conditions

It follows from the assumption of a fixed-end condition at  $x = 0$  that

$$u(t, 0) = 0. \quad (7.12)$$

The balance of forces at  $x = \ell$ , in the manner detailed in [120], yields the second boundary condition

$$N(t, \ell) = -k_\ell u(t, \ell) - c_\ell \frac{\partial u}{\partial t}(t, \ell) - m_\ell \frac{\partial^2 u}{\partial t^2}(t, \ell). \quad (7.13)$$

Note that this energy-dissipating boundary condition reduces to the free-end condition

$$N(t, \ell) = 0$$

in the absence of an end mass and damped, elastic restoring force. Moreover, it is observed that if one divides by  $k_\ell$  and takes  $k_\ell \rightarrow \infty$  to model an infinite restoring force, the dissipative boundary condition (7.13) converges to the fixed-end condition (7.12). The boundary conditions can thus be summarized as

$$\begin{aligned} u(t, 0) &= 0 \\ N(t, \ell) &= -k_\ell u(t, \ell) - c_\ell \frac{\partial u}{\partial t}(t, \ell) - m_\ell \frac{\partial^2 u}{\partial t^2}(t, \ell). \end{aligned}$$

Finally, initial conditions are specified to be

$$\begin{aligned} u(0, x) &= u_0(x) \\ \frac{\partial u}{\partial t}(0, x) &= u_1(x). \end{aligned}$$

### Strong Formulation of the Model

We summarize here rod models for stacked PZT actuators operating in linear and nonlinear input regimes with constitutive behavior quantified by (7.1) and (7.3). The magnetic models are completely analogous and follow directly from the constitutive relations (7.5) and (7.6).

#### *PZT Rod Model — Linear Inputs*

$$\begin{aligned} \rho A \frac{\partial^2 u}{\partial t^2} - Y A \frac{\partial^2 u}{\partial x^2} - c A \frac{\partial^3 u}{\partial x^2 \partial t} &= f - Y A \frac{d_{31}}{h} \frac{\partial V(t)}{\partial x} \\ P &= Y d_{31} \frac{\partial u}{\partial x} + \chi \frac{V}{h} \end{aligned} \quad (7.14)$$

*PZT Rod Model — Hysteretic and Nonlinear Inputs*

$$\begin{aligned} \rho A \frac{\partial^2 u}{\partial t^2} - Y A \frac{\partial^2 u}{\partial x^2} - c A \frac{\partial^3 u}{\partial x^2 \partial t} &= f - a_1 A \frac{\partial(P(t) - P_R)}{\partial x} - a_2 A \frac{\partial(P(t) - P_R)^2}{\partial x} \\ [P(E, \frac{\partial u}{\partial x})](t) &= \int_0^\infty \int_{-\infty}^\infty \nu_1(E_c) \nu_2(E_I) [\bar{P}(E + E_I, \frac{\partial u}{\partial x}; E_c, \xi)](t) dE_I dE_c. \end{aligned} \tag{7.15}$$

In the polarization relation, the densities  $\nu_1$  and  $\nu_2$  satisfy the conditions (2.113) with a possible choice given by (2.117). The kernel  $\bar{P}$  is given by (2.89), (2.90) or (2.99). As detailed in Remark 7.1.1, the strain-dependence in the polarization is typically neglected in actuator models but may need to be retained for sensor characterization.

**Weak Formulation of the Model**

The strong formulation of the model, derived via force balancing or Newtonian principles, illustrates in a natural manner the forced dynamics of the rod. However, it has two significant disadvantages from the perspective of approximation. First, the second derivatives in  $x$  necessitate the use of cubic splines, cubic Hermite elements, or high-order difference methods to construct a semi-discrete system. Secondly, the neglect of direct electromechanical/magnetomechanical effects to create a linear model in  $u$  leads to spatial derivatives of *spatially invariant* voltage and polarization terms  $V(t)$  and  $P(t)$ . This produces a Dirac distribution at  $x = \ell$  which will curtail the convergence of modal methods applied to the strong formulation of the model.

Both problems can be alleviated by considering a weak or variational formulation of the model developed either via integration by parts or Hamiltonian energy principles as summarized in Section 7.3.2. We emphasize that the designation “weak form” refers to the fact that underlying assumptions regarding differentiability are weakened in the sense of distributions rather than indicating a form having diminished utility. Conversely, the energy basis provided by the Hamiltonian formulation, in combination with the fact that reduced differentiability requirements make the weak form a natural setting for numerical approximation, imbues the weak model formulation with broader applicability than the strong formulation in a number of applications.

To construct a weak formulation of the model via integration by parts, we consider states  $\xi(t) = (u(t, \cdot), u(t, \ell))$  in the state space

$$X = L^2(0, \ell) \times \mathbb{R}$$

with the inner product

$$\langle \Phi_1, \Phi_2 \rangle_X = \int_0^\ell \rho A \phi_1 \phi_2 dx + m_\ell \varphi_1 \varphi_2 \tag{7.16}$$

where  $\Phi_1 = (\phi_1, \varphi_1), \Phi_2 = (\phi_2, \varphi_2)$  with  $\varphi_1 = \phi_1(\ell), \varphi_2 = \phi_1(\ell)$ . Test functions  $\phi$  are required to satisfy the essential boundary condition (7.12) at  $x = 0$  but not the

natural condition (7.13) at  $x = \ell$  so the space of test functions is taken to be

$$V = \{ \Phi = (\phi, \varphi) \in X \mid \phi \in H^1(0, \ell), \phi(0) = 0, \phi(\ell) = \varphi \}$$

with the inner product

$$\langle \Phi_1, \Phi_2 \rangle_V = \int_0^\ell Y A \phi_1' \phi_2' dx + k_\ell \varphi_1 \varphi_2. \quad (7.17)$$

Consider the general relation (7.10). Multiplication by  $\phi \in H_0^1(0, \ell) = \{ \phi \in H^1(0, \ell) \mid \phi(0) = 0 \}$  and integration by parts in space yields the weak form

$$\int_0^\ell \rho A \frac{\partial^2 u}{\partial t^2} \phi dx + \int_0^\ell N \frac{d\phi}{dx} dx - N(t, \ell) \phi(\ell) = \int_0^\ell f \phi dx$$

where  $N(t, \ell)$  is given by (7.13). For nonlinear and hysteretic inputs, the weak formulation of the model is thus

$$\begin{aligned} & \int_0^\ell \rho A \frac{\partial^2 u}{\partial t^2} \phi dx + \int_0^\ell \left[ Y A \frac{\partial u}{\partial x} + c A \frac{\partial^2 u}{\partial x \partial t} \right] \frac{d\phi}{dx} dx \\ &= \int_0^\ell f \phi dx + A [a_1(P - P_R) + a_2(P - P_R)^2] \int_0^\ell \frac{d\phi}{dx} dx \\ & \quad - \left[ k_\ell u(t, \ell) + c_\ell \frac{\partial u}{\partial t}(t, \ell) + m_\ell \frac{\partial^2 u}{\partial t^2}(t, \ell) \right] \phi(\ell) \end{aligned} \quad (7.18)$$

which must hold for all  $\phi \in V$ . The polarization is specified by (7.15) or (2.114).

Equivalent analysis is used to construct the weak formulation of the PZT model with linear inputs or equivalent models for rods in ferromagnetic transducers.

### 7.3.2 Hamiltonian Formulation

Alternatively, one can employ calculus of variations and fundamental energy relations to derive a weak formulation of the model. This is most easily motivated in the case of conservative forces so we consider initially a regime for which  $c = m_\ell = k_\ell = c_\ell = 0$  as well as  $F = P = 0$ . Hence we consider an elastic rod that is fixed at  $x = 0$  and free at  $x = \ell$ . The space of test functions is  $V = H_0^1(0, \ell)$  with the inner product (7.17) employing  $k_\ell = 0$ .

As detailed in Appendix C, two fundamental energy relations are the Lagrangian

$$\mathcal{L} = K - U$$

and the total energy

$$\mathcal{H} = K + U \quad (7.19)$$

where  $K$  and  $U$  respectively denote the kinetic and potential energies. It is shown in Section C.3 that for conservative systems, the Hamiltonian — which is the Legendre transform of  $\mathcal{L}$  — is exactly the total energy specified in (7.19) thus providing one of the correlations between Lagrangian and Hamiltonian theory.

Lagrangian mechanics, which we will employ here, is based on variational principles — extremals of functionals — whereas Hamiltonian mechanics relies directly on total energy principles. The former leads to natural computational frameworks whereas the latter provides a basis for developing some of the deeper theoretical results associated with celestial, quantum and statistical mechanics. The combined field of Lagrangian and Hamiltonian mechanics provides one of the pillars of classical physics and we refer the reader to [15,319] for details regarding the fundamental physics and Weinstock [505] for application of Lagrangian theory to elastic systems analogous to that considered here.

The reader is cautioned that terminology can be confusing. For example, Hamilton’s principle formulated in terms of the Lagrangian  $\mathcal{L}$  is fundamental to Lagrange dynamics, the variational basis for which was discovered by Hamilton [204]!

For the rod, the kinetic and potential energies are

$$K = \frac{1}{2} \rho A \int_0^\ell u_t^2(t, x) dx \tag{7.20}$$

$$U = \frac{1}{2} A \int_0^\ell \sigma \varepsilon dx = \frac{1}{2} Y A \int_0^\ell u_x^2(t, x) dx$$

so that

$$\mathcal{L} = \frac{1}{2} A \int_0^\ell [\rho u_t^2 - Y u_x^2] dx.$$

The integral of  $\mathcal{L}$  over an arbitrary time interval  $[t_0, t_1]$ ,

$$\mathcal{A}[u] = \int_{t_0}^{t_1} \mathcal{L} dt,$$

is termed the *action* or *action integral* and provides the functional at the heart of Hamilton’s principle.

### Hamilton’s Principle

Hamilton’s principle can be broadly state in this context as follows: “for the arbitrary time interval  $[t_0, t_1]$ , the motion  $u$  of the rod renders the action integral stationary when compared with all admissible candidates  $\hat{u} = u + \epsilon \Theta$  for the motion.” As detailed in Section C.2, this yields the requirement that

$$\left. \frac{d}{d\epsilon} \mathcal{A}[u + \epsilon \Theta] \right|_{\epsilon=0} = 0 \tag{7.21}$$

for all admissible  $\Theta$ .

To quantify the class of admissible perturbations, consider variations of the form

$$\hat{u}(t, x) = u(t, x) + \epsilon \eta(t) \phi(x)$$

where  $\eta$  and  $\phi$  satisfy

$$\begin{aligned} \text{(i)} \quad & \eta(t_0) = \eta(t_1) = 0 \\ \text{(ii)} \quad & \phi \in V = H_0^1(0, \ell). \end{aligned} \tag{7.22}$$

The first criterion guarantees that

$$\widehat{u}(t_0, x) = u(t_0, x), \quad \widehat{u}(t_1, x) = u(t_1, x),$$

as depicted in Figure 7.10, whereas the second assumption guarantees that  $\widehat{u}(t, \cdot) \in H_0^1(0, \ell)$  so that candidates satisfy the essential boundary condition and have sufficient smoothness to permit evaluation of the potential energy.

The condition (7.21) then yields

$$\begin{aligned} 0 &= \int_{t_0}^{t_1} \int_0^\ell [\rho A u_t \Theta_t - Y A u_x \Theta_x] dx dt \\ &= - \int_{t_0}^{t_1} \eta(t) \int_0^\ell [\rho A u_{tt} \phi + Y A u_x \phi_x] dx dt \end{aligned} \tag{7.23}$$

which implies that

$$\rho A \int_0^\ell u_{tt} \phi dx + Y A \int_0^\ell u_x \phi_x dx = 0 \tag{7.24}$$

for all  $\phi \in V$ . Integration by parts, in combination with condition (i) of (7.22), was employed in the second step of (7.23).

We first note that (7.24) is identical to (7.18) if one takes  $c = P = f = 0$  and  $m_\ell = c_\ell = k_\ell = 0$  in the latter formulation. Moreover, if  $u$  exhibits the additional smoothness  $u(t, \cdot) \in H_0^1(0, \ell) \cap H^2(0, \ell)$ , integration by parts yields the strong form (7.14) or (7.15) with the simplifying parameter choices. However, the weakened smoothness requirement  $u(t, \cdot) \in H_0^1(0, \ell)$  is natural from an energy perspective and advantageous for approximation.

Secondly, inclusion of the elastic and inertial boundary components  $k_\ell, m_\ell$ , distributed force  $f$  and nonlinear polarization components  $a_1(P - P_R)$  and  $a_2(P - P_R)^2$  can be accomplished using an augmented action integral

$$\mathcal{A}[u] = \int_{t_0}^{t_1} [K - U + F_{nc}] dt \tag{7.25}$$

and *extended Hamilton's principle* as detailed in Section 6-7 of Weinstock [505]. Here  $F_{nc}$  directly incorporates the nonconservative distributed force  $f$  and linear or nonlinear polarization inputs when low-order strain effects are neglected in the polarization model.

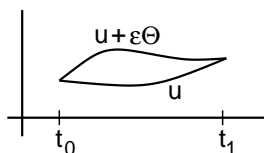


**Figure 7.10.** Admissible variations of the motion considered in Hamilton's principle.

The incorporation of Kelvin–Voigt and boundary damping is more difficult in the variational formulation since they involve derivatives of the displacement which constitutes a generalized coordinate. Hence the incorporation of nonconservative internal damping provides an example of when integration of the strong formulation obtained through force balancing proves an easier strategy for obtaining a weak formulation of the model than direct application of variational principles. Even in this case, however, the consideration of energy or variational principles provides the natural function spaces for constructing the weak formulation and developing approximation techniques as detailed in Section 8.2.

### 7.3.3 Device Characterization

We illustrate here the performance of the rod model (7.18) for characterizing the displacements shown in Figures 7.11 and 7.12 which were generated by the AFM stage depicted in Figure 7.5. The nonlinear field-polarization relation is characterized by the homogenized energy model (7.15) or (2.114) with general densities  $\nu_1$  and  $\nu_2$  identified via the parameter estimation techniques detailed in Section 2.6.6. The polarization  $P_k$  at each measured field value  $E_k = E(t_k)$  was subsequently input to the rod model (7.18) approximated in the manner discussed in Section 8.1.

Figures 7.11 and 7.12 illustrate the data and model fits obtained at four drive levels and four input frequencies. The behavior in Figure 7.11 represents nested mi-

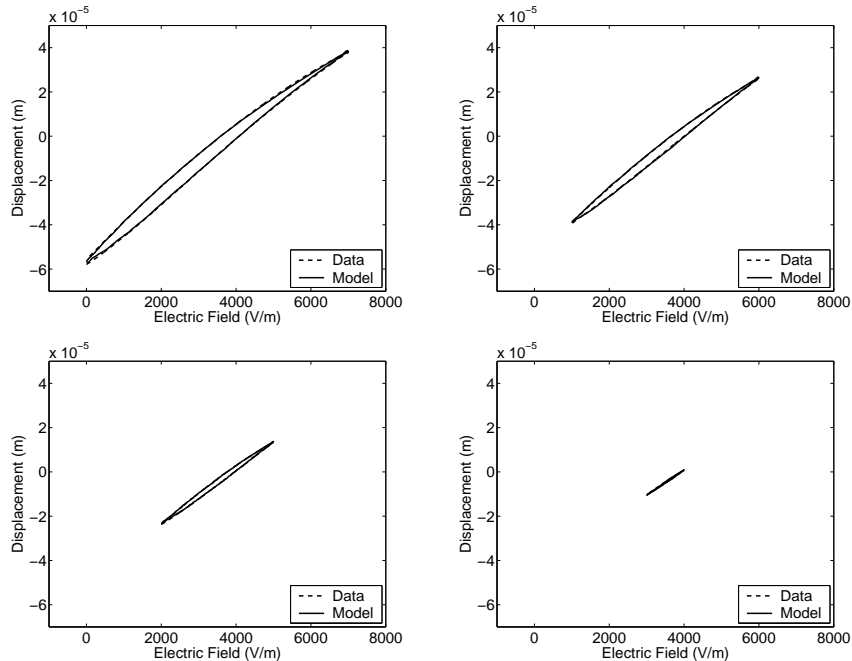


**Figure 7.11.** Data and model fit for a stacked PZT actuator employed in the AFM stage depicted in Figure 7.5 at 0.1 Hz.

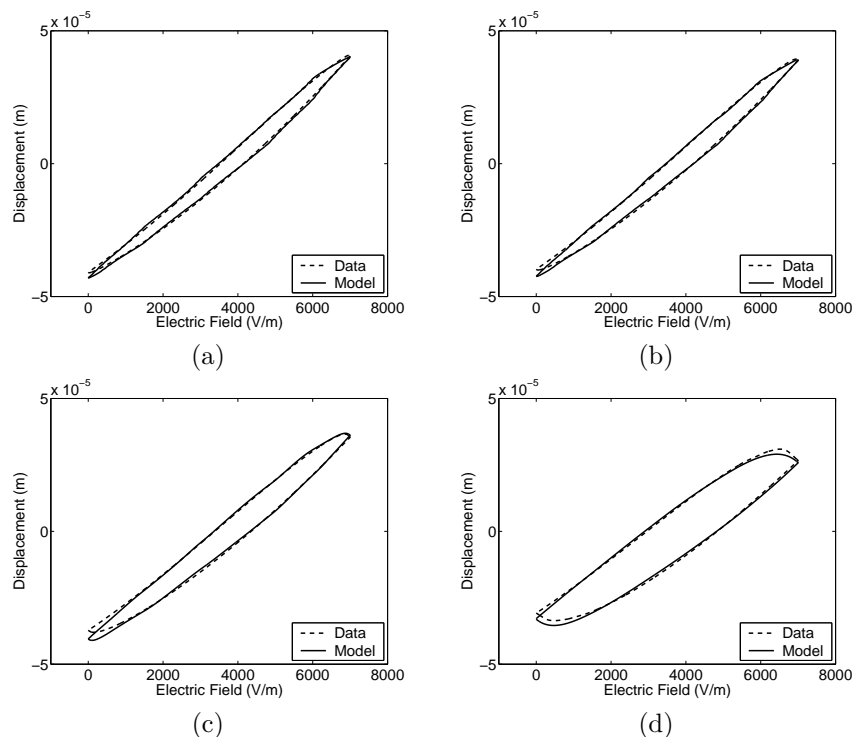


**Figure 7.12.** Use of the polarization model (7.15) and rod model (7.18) to characterize the frequency-dependent behavior of a stacked PZT actuator employed in the AFM stage: (a) 0.28 Hz, (b) 1.12 Hz, (c) 5.58 Hz, and (d) 27.9 Hz.

nor loop behavior which is plotted separately to demonstrate the model's accuracy. Figure 7.12 illustrates that the hysteretic PZT behavior exhibits frequency and rate-dependence even within the 0.1–0.5 Hz range. This necessitates the incorporation of dynamic input behavior — which is one of the hallmarks of the homogenized energy framework — when characterizing and developing model-based control designs for broadband applications. Details regarding the characterization and robust control design for this AFM application can be found in [210].

## 7.4 Beam Models

Beam models are similar to rod models in the sense that through the assumptions of Section 7.2, they quantify motion as a function of one spatial coordinate. However, beam dynamics are characterized by out-of-plane or transverse motion which necessitates balancing both moments and shear stresses to construct a strong formulation of the model. For homogeneous rods subject to uniform in-plane forces or stresses, any line suffices as 1-D reference line on which to represent dynamics. This is untrue for beams and one typically employs the *neutral line*, characterized by zero stress in pure bending regimes, as the reference line.

To provide prototypes that illustrate a number of the modeling issues associated with beams, plates and shells, we consider the structures depicted in Figure 7.13. The thin beam with surface-mounted patches exhibits effective or homogenized material parameters and piecewise inputs in the region covered by the patches but is simplified by the fact that the reference line and middle line coincide due to symmetry. This is not the case for the *asymmetric* polymer unimorph which motivates its use as a prototype for demonstrating the computation of the reference line as an initial step prior to moment computation.

In both cases, we let  $w$  and  $f$  respectively denote the transverse displacement and distributed out-of-plane force. The effective linear density (units of kg/m), Young's modulus, and Kelvin–Voigt damping coefficients for the composite structure are denoted by  $\rho$ ,  $Y$  and  $c$  whereas material properties for constituent components are delineated by subscripts. Finally, we assume fixed-end conditions at  $x = 0$  and free-end conditions at  $x = \ell$ .

As a point of notation, the thin beam model developed here is referred to as an Euler–Bernoulli model. The Timoshenko model which incorporates shear deformations and rotational inertia is developed in Section 7.8.

### 7.4.1 Unimorph Model

The unimorph model illustrates a number of issues associated with model development for beams so we consider it first. For simplicity, we frame the discussion in the context of the linear constitutive relations (7.1) and simply summarize the nonlinear input model resulting from (7.3) at the end of the section. Furthermore, while the in-plane and out-of-plane displacements are coupled due to the geometry, we will focus here on uncoupled out-of-plane displacements. The coupling will be discussed in Sections 7.6 and 7.7 in the context of shell, curved beam, and THUNDER models.

The geometric and material properties for the active PVDF layer and inactive polyimide layer are respectively delineated by the subscripts  $A$  and  $I$ . Both layers are assumed to have width  $b$  and the unimorph is assumed to have length  $\ell$ .

#### Force and Moment Balancing

To establish equations of motion, we balance forces and moments associated with an infinitesimal beam element using the convention depicted in Figure 7.13.<sup>30</sup>

##### Force Balance

We first balance the forces associated with the shear resultants  $Q$ , distributed forces  $f$ , and viscous air damping which is assumed proportional to the transverse velocity with proportionality constant  $\gamma$ . Newton's second law then yields

$$\int_x^{x+\Delta x} \rho \frac{\partial^2 w}{\partial t^2}(t, s) ds = Q(t, x + \Delta x) - Q(t, x) + \int_x^{x+\Delta x} \left[ f(t, s) - \gamma \frac{\partial w}{\partial t}(t, s) \right] ds$$

<sup>30</sup>We note that the moment and curvature conventions are opposite to those employed by some authors. The association of positive moments with negative curvature is consistent with the convention employed for general shells in Section 7.6 which in turn is consistent with 3-D elasticity relations. Both conventions yield the same final model as long as consistency is maintained.

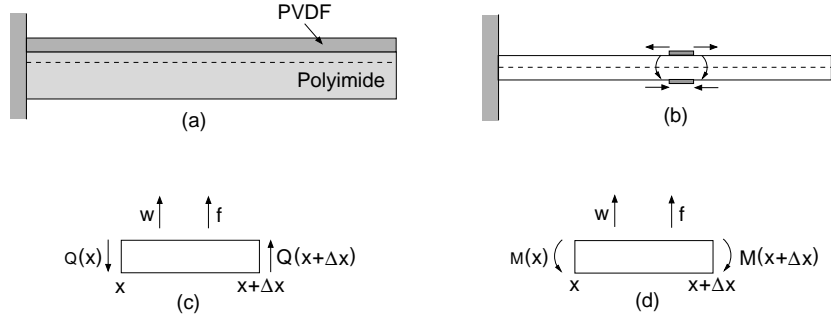


**Figure 7.13.** (a) Asymmetric polymer unimorph comprised of an active PVDF layer and an inactive polyimide layer. (b) Cross-section of the beam from Figure 7.4 with symmetric, surface-mounted PZT patches. (c) and (d) Convention for the force and moment results employed when constructing the strong formulation of Euler-Bernoulli beam models.

where the composite linear density is

$$\rho = h_A b \rho_A + h_I b \rho_I. \tag{7.26}$$

Dividing by  $\Delta x$  and taking  $\Delta x \rightarrow 0$  yields

$$\rho \frac{\partial^2 w}{\partial t^2} + \gamma \frac{\partial w}{\partial t} = \frac{\partial Q}{\partial x} + f.$$

**Moment Balance**

We next balance moments about the left end of the element to obtain

$$M(t, x + \Delta x) - M(t, x) - Q(t, x + \Delta x)\Delta x + \int_x^{x+\Delta x} f(t, s)(s - x)dx = 0.$$

The retention of first-order terms after dividing by  $\Delta x$  and taking  $\Delta x \rightarrow 0$  gives the relation

$$Q = \frac{\partial M}{\partial x} \tag{7.27}$$

relating the moment and shear resultant. This then yields

$$\rho \frac{\partial^2 w}{\partial t^2} + \gamma \frac{\partial w}{\partial t} - \frac{\partial^2 M}{\partial x^2} = f$$

as a strong formulation of the beam model.

**Moment Evaluation**

To complete the model, it is necessary to formulate the moment  $M$  in terms of geometric properties of the unimorph. To accomplish this, we must first determine the reference line which is defined to be the neutral line  $z_n$  that exhibits zero stress during bending — recall that through Assumptions 1–4 of Section 7.2, beam motion is defined in terms of the reference line dynamics — thus yielding 1-D models.

*Neutral Line Specification*

For linear inputs, (7.1) yields

$$\sigma = \begin{cases} Y_A \varepsilon + c_A \dot{\varepsilon} - Y_A \frac{d_{31}}{h_A} V & , \text{Active layer} \\ Y_I \varepsilon + c_I \dot{\varepsilon} & , \text{Inactive layer} \end{cases} \quad (7.28)$$

under the assumption of Kelvin–Voigt damping — the reader is referred to [122] for a formulation that employs more comprehensive viscoelastic Boltzmann damping relations. As illustrated for the stress profile depicted in Figure 7.14, the moment arm at height  $z$  in the unimorph has length  $z - z_n$  so the total moment is given by

$$M = \int_{-h_I}^{h_A} b(z - z_n) \sigma dz. \quad (7.29)$$

To specify  $z_n$ , it is noted that at equilibrium the balance of forces, under Assumption 4 of Section 7.2 which posits a linear strain profile  $\varepsilon(z) = \kappa(z - z_n)$  in the absence of in-plane strains, yields

$$\int_{-h_I}^0 \kappa b Y_I (z - z_n) dz + \int_0^{h_A} \kappa b Y_A (z - z_n) dz = 0. \quad (7.30)$$

This gives the neutral line relation

$$z_n = \frac{Y_A h_A^2 - Y_I h_I^2}{2(Y_A h_A + Y_I h_I)}.$$

Analogous neutral surface representations for PZT-based unimorphs are determined in [295, 393].

*Effective Parameters and Moment Components*

The stress relation (7.28) has the form

$$\sigma = \sigma_e + \sigma_d + \sigma_{ext}$$

where  $\sigma_e, \sigma_d$  and  $\sigma_{ext}$  denote the elastic, damping and external components. Similarly, we can decompose the total moment into analogous components

$$M = M_e + M_d + M_{ext}.$$

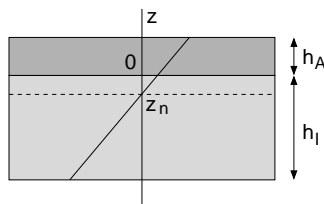


**Figure 7.14.** Geometry used to compute the neutral line  $z_n$ .

Since the strategy in thin beam theory is to represent all moments and forces through the thickness of the structure by resultants at the neutral line, it is necessary to specify these resultants either directly, in terms of the geometry and properties of constituent materials, or in terms of effective parameters for the combined structure. The latter approach provides the capability for incorporating material properties that are known (e.g., stiffness properties) while providing a general framework for the identification of unknown parameters (e.g., damping parameters).

We consider first the moment generated by the elastic component  $\sigma_e$  of the constitutive relation (7.28). To determine an effective Young's modulus  $Y$  for the composite structure, the general moment is equated to the components,

$$\int_{-h_I}^{h_A} bY\kappa(z - z_n)^2 dz = \int_{-h_I}^0 bY_I\kappa(z - z_n)^2 dz + \int_0^{h_A} bY_A\kappa(z - z_n)^2 dz,$$

to yield

$$Y = \frac{Y_I[(h_I + z_n)^3 - z_n^3] + Y_A[(h_A - z_n)^3 + z_n^3]}{(h_A - z_n)^3 + (h_I + z_n)^3}. \quad (7.31)$$

For thin beams, the relation

$$\kappa = -\frac{\partial^2 w}{\partial x^2} \quad (7.32)$$

provides a first-order approximation to the change in curvature — see Section 7.6 for details — so the elastic component of the moment is

$$\begin{aligned} M_e &= -\int_{-h_I}^{h_A} bY \frac{\partial^2 w}{\partial x^2} (z - z_n)^2 dz \\ &= -YI \frac{\partial^2 w}{\partial x^2} \end{aligned} \quad (7.33)$$

where

$$I = \frac{b}{3} [(h_A - z_n)^3 + (h_I + z_n)^3]. \quad (7.34)$$

Through (7.31) and (7.34), the effective Young's modulus and generalized moment of inertia for the composite structure can be specified in terms of the geometry and Young's moduli for the constituent materials. Alternatively, the combined parameter  $YI$  can be treated as unknown and estimated through a least squares fit to data.

A similar analysis can be employed for the damping component of the moment. However, since values of the damping coefficients for the constituent materials are typically unavailable, we directly consider the moment relation

$$M_d = -cI \frac{\partial^3 w}{\partial x^2 \partial t} \quad (7.35)$$

where the parameter  $cI$  is considered unknown and is determined through inverse problem techniques.

Finally, the external moment is given by

$$\begin{aligned} M_{ext} &= - \int_0^{h_A} bY_A(z - z_n) \frac{d_{31}}{h_A} V(t) dz \\ &= k_p V(t) \end{aligned} \quad (7.36)$$

where

$$k_p = \frac{bY_A d_{31}}{2h_A} [z_n^2 - (h_A - z_n)^2]. \quad (7.37)$$

### Strong Formulation of the Model with Boundary and Initial Conditions

The fixed-end condition at  $x = 0$  enforces zero transverse displacement and slope which yields the boundary condition

$$w(t, 0) = \frac{\partial w}{\partial x}(t, 0) = 0.$$

Free-end conditions are characterized by the lack of a shear stress or moment; hence use of (7.27) to eliminate the former yields the boundary condition

$$M(t, \ell) = \frac{\partial M}{\partial x}(t, \ell) = 0.$$

Finally, the initial displacements and velocities are defined to be

$$w(0, x) = w_0(x) \quad , \quad \frac{\partial w}{\partial t}(0, x) = w_1(x).$$

The strong formulation of the Euler-Bernoulli model with linear inputs is thus

$$\begin{aligned} \rho \frac{\partial^2 w}{\partial t^2} + \gamma \frac{\partial w}{\partial t} - \frac{\partial^2 M}{\partial x^2} &= f(t, x) \\ w(t, 0) = \frac{\partial w}{\partial x}(t, 0) &= 0 \\ M(t, \ell) = \frac{\partial M}{\partial x}(t, \ell) &= 0 \\ w(0, x) = w_0(x) \quad , \quad \frac{\partial w}{\partial t}(0, x) &= w_1(x) \end{aligned} \quad (7.38)$$

where  $\rho$  is given by (7.26) and  $M = M_e + M_d + M_{ext}$  has the elastic, damping and external components defined in (7.33), (7.35) and (7.36).

### Weak Formulation of the Model — Linear Inputs

The elastic and damping components  $M_e$  and  $M_d$  yield fourth-order derivatives in (7.38) whereas differentiation of  $M_{ext}$  yields Dirac behavior at  $x = \ell$ . To

avoid ensuing approximation difficulties, it is advantageous to consider a weak or variational formulation of the model developed either through integration by parts or Hamiltonian (energy) principles analogous to those detailed in Section 7.3.2 for the rod model. We summarize the former approach and refer the reader to [34] for details illustrating the construction of a beam model using variational principles.

We consider states  $w(t, \cdot)$  in the state space

$$X = L^2(0, \ell)$$

and test functions  $\phi$  in

$$V = H_0^2(0, \ell) = \{\phi \in H^2(0, \ell) \mid \phi(0) = \phi'(0) = 0\}.$$

The inner products

$$\langle \psi, \phi \rangle_X = \int_0^\ell \rho \psi \phi dx$$

$$\langle \psi, \phi \rangle_V = \int_0^\ell YI \psi'' \phi'' dx$$

follow from the kinetic and strain (potential) energy components of the variational formulation — e.g., compare the inner products (7.16) and (7.17) for the rod model with the intermediate weak formulation (7.23) derived from the kinetic and potential energy relations (7.20).

Multiplication of (7.38) by test functions  $\phi \in V$  and integration by parts yields the weak formulation

$$\int_0^\ell \rho \frac{\partial^2 w}{\partial t^2} \phi dx + \int_0^\ell \gamma \frac{\partial w}{\partial t} \phi dx - \int_0^\ell M \frac{d^2 \phi}{dx^2} dx = \int_0^\ell f \phi dx$$

or

$$\begin{aligned} \int_0^\ell \rho \frac{\partial^2 w}{\partial t^2} \phi dx + \int_0^\ell \gamma \frac{\partial w}{\partial t} \phi dx + \int_0^\ell YI \frac{\partial^2 w}{\partial x^2} \frac{d^2 \phi}{dx^2} dx \\ + \int_0^\ell cI \frac{\partial^3 w}{\partial x^2 \partial t} \frac{d^2 \phi}{dx^2} dx = \int_0^\ell f \phi dx + \int_0^\ell k_p V(t) \frac{d^2 \phi}{dx^2} dx \end{aligned} \tag{7.39}$$

of the beam model for the unimorph. Approximation techniques for the model in this form are discussed in Section 8.2.

#### Weak Formulation of the Model — Nonlinear Inputs

The development for nonlinear and hysteretic inputs is analogous and follows simply by employing the nonlinear constitutive (7.3) rather than (7.1) when computing the moment (7.36). This yields

$$\begin{aligned} \int_0^\ell \rho \frac{\partial^2 w}{\partial t^2} \phi dx + \int_0^\ell \gamma \frac{\partial w}{\partial t} \phi dx + \int_0^\ell YI \frac{\partial^2 w}{\partial x^2} \frac{d^2 \phi}{dx^2} dx + \int_0^\ell cI \frac{\partial^3 w}{\partial x^2 \partial t} \frac{d^2 \phi}{dx^2} dx \\ = \int_0^\ell f \phi dx + [k_1(P(E) - P_R) + k_2(P(E) - P_R)^2] \int_0^\ell \frac{d^2 \phi}{dx^2} dx \end{aligned} \tag{7.40}$$

which must hold for all  $\phi \in V$ . The nonlinear  $E$ - $P$  dependence is quantified by (7.3) or (2.114). The constants  $k_1$  and  $k_2$  have representations analogous to  $k_p$  in (7.37) but are treated as parameters to be estimated through a least squares fit since  $a_1$  and  $a_2$  from (7.3) are unknown.

### Device Characterization

To illustrate attributes of the beam model when characterizing the PVDF-polyimide unimorph depicted in Figure 7.13, we summarize results from [122]. The experimental data consists of tip displacement measurements produced with 1 Hz peak input voltages of 25 V, 50 V, 75 V and 100 V as shown in Figure 7.15. Because these voltages are in a pre-switching range for PVDF, the linear input model was employed using the parameters summarized in Table 7.1. The relations (7.26), (7.31) and (7.34) were used to compute initial values for the effective parameters  $\rho$  and  $Y$ . Final values for all of the parameters were obtained through a least squares fit to the 100 V data and the resulting model was used to predict the tip displacement in response to 25 V, 50 V and 75 V inputs.

It is noted from Figure 7.15 that the model fit and predictions are very accurate in this linear regime. However, the resulting internal damping parameter

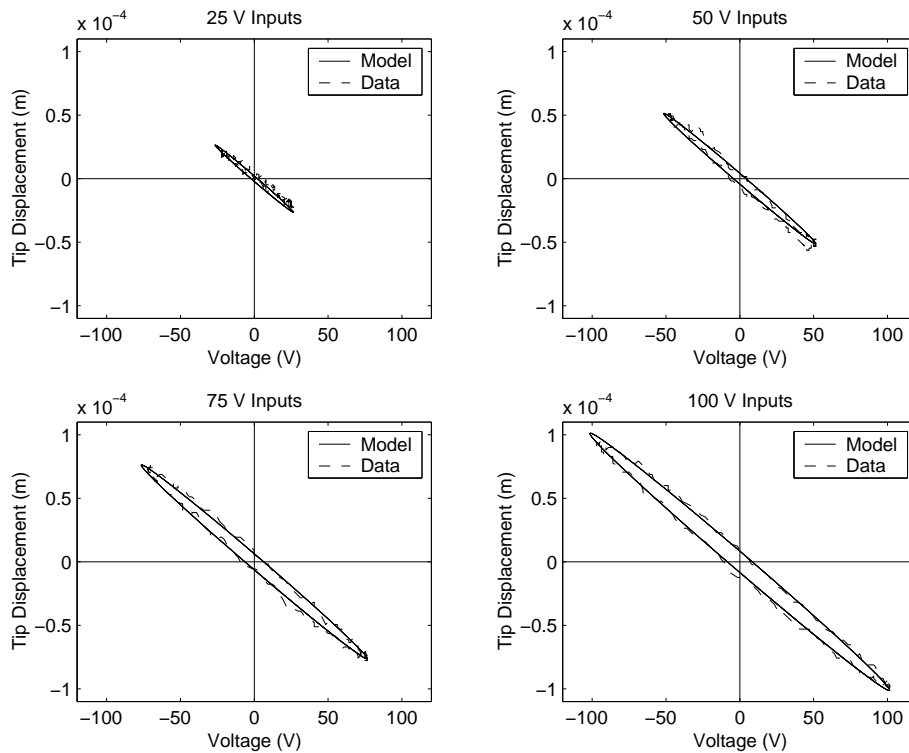


**Figure 7.15.** Experimental data and model fit at 100 V, and model predictions at 25 V, 50 V and 75 V.

Symbol	Units	Experimental Range	Employed in Model
$\ell$	m	0.03	0.03
$b$	m	0.013	0.013
$h_A$	m	$52 \times 10^{-6}$	$52 \times 10^{-6}$
$h_I$	m	$125 \times 10^{-6}$	$137 \times 10^{-6}$
$\rho_A$	kg/m <sup>3</sup>	$1.78 \times 10^3$	$1.78 \times 10^3$
$\rho_I$	kg/m <sup>3</sup>	$1.3 \times 10^3$	$1.3 \times 10^3$
$Y_A$	N/m <sup>2</sup>	$2.0 \times 10^9 - 2.6 \times 10^9$	$2.0 \times 10^9$
$Y_I$	N/m <sup>2</sup>	$2.5 \times 10^9 - 2.8 \times 10^9$	$2.7 \times 10^9$
$cI$	N·s/m <sup>2</sup>		$2.2848 \times 10^{-7}$
$\gamma$	N·s/m <sup>2</sup>		0.005
$d_{31}$	C/N	$20 \times 10^{-12} - 27 \times 10^{-12}$	$20 \times 10^{-12}$

**Table 7.1.** *Experimental parameter ranges and values employed in the model.*

$cI = 2.2848 \times 10^{-7}$  is only two orders of magnitude smaller than the stiffness parameter  $YI = 1.7250 \times 10^{-5}$ . This is significantly larger than damping values estimated for elastic materials which are often five orders of magnitude less than corresponding stiffness parameters — e.g., see pages 134, 147 of [33]. These large damping coefficients reflect the viscoelastic nature of the unimorph, and the development of models and approximation techniques which incorporate Boltzmann damping constitute an active research area.

### 7.4.2 Uniform Beam with Surface-Mounted PZT Patches

Construction of the unimorph model illustrates issues associated with determination of the neutral line and effective density and stiffness parameters for a composite, asymmetric structure. To demonstrate some of the simplifications which result for symmetric beams and the quantification of piecewise inputs, we consider the thin beam with surface-mounted patches depicted in Figure 7.13(b). For simplicity, we consider a single patch pair but note that extension to multiple pairs is achieved in an analogous manner as detailed in Section 7.5 for a thin plate. We initially consider linear operating regimes for which application of diametrically opposite voltages generate pure bending moments and transverse motion. This is in contrast to equal voltages which generate in-plane motion, quantified using the techniques of Section 7.3, or general voltages which produce both in-plane and out-of-plane motion.<sup>31</sup>

We retain the notation convention established in Section 7.4.1 and let the subscript  $I$  denote beam material properties (e.g., properties of aluminum or steel) and let the subscript  $A$  denote PZT properties. The thickness coordinate  $z$  is configured so that  $z = 0$  corresponds with the beam centerline as depicted in Figure 7.16.

<sup>31</sup>We note that in high drive regimes, opposite fields to the patch pairs produce both bending and in-plane motion due to the asymmetry of the  $E$ - $\epsilon$  relation about  $E = 0$  as illustrated in Figure 2.10(b). These coupled effects are considered in Section 7.5.

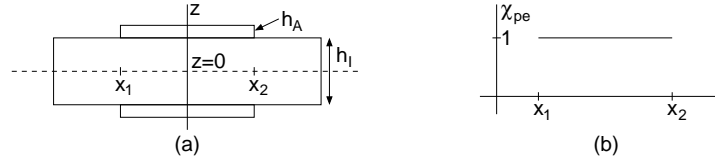


**Figure 7.16.** (a) Coordinate system for moment computation and (b) characteristic function  $\chi_{pe}$  which delineates the region with surface-mounted patches.

**Force and Moment Balancing**

Forces and moments are balanced in a manner identical to that used to construct equations of motion for the unimorph. This yields

$$\rho \frac{\partial^2 w}{\partial t^2} + \gamma \frac{\partial w}{\partial t} - \frac{\partial^2 M}{\partial x^2} = f \tag{7.41}$$

where the linear density  $\rho$  is given by

$$\rho(x) = \begin{cases} 2h_A b \rho_A + h_I b \rho_I & , \quad x \in [x_1, x_2] \\ h_I b \rho_I & , \quad x \in [0, x_1) \cup (x_2, \ell] \end{cases}$$

and  $[x_1, x_2]$  is the region covered by the patches. To consolidate notation, we employ the characteristic equation

$$\chi_{pe}(x) = \begin{cases} 1 & , \quad x \in [x_1, x_2] \\ 0 & , \quad x \in [0, x_1) \cup (x_2, \ell], \end{cases}$$

depicted in Figure 7.16(b), to formulate the density as

$$\rho(x) = h_I b \rho_I + 2\chi_{pe}(x) h_A b \rho_A. \tag{7.42}$$

**Moment Evaluation**

The conservation principles used to compute the neutral line  $z_n$ , effective stiffness  $YI$ , and external coupling parameter  $k_p$  are the same as those employed in Section 7.4.1 for the unimorph so we simply summarize here the final expressions for the thin beam geometry.

Force balancing in a manner analogous to (7.30) yields the centerline

$$z_n = 0$$

for the neutral line. This is consistent with the symmetry of the structure.

The elastic, damping and external moments

$$M_e = -YI(x) \frac{\partial^2 w}{\partial x^2} \quad , \quad M_d = -cI(x) \frac{\partial^3 w}{\partial x^2 \partial t} \quad , \quad M_{ext} = k_p(x)V(t) \tag{7.43}$$

have the same form as the unimorph moments (7.33), (7.35) and (7.36). However, the geometry-dependent coefficients differ and are given by

$$\begin{aligned}
 YI(x) &= Y_I \frac{h_I^3 b}{12} + Y_A c_3 \chi_{pe}(x) \\
 cI(x) &= c_I \frac{h_I^3 b}{12} + c_A c_3 \chi_{pe}(x) \\
 k_p(x) &= \frac{2Y_A d_{31} c_2}{h_A} \chi_{pe}(x)
 \end{aligned}
 \tag{7.44}$$

where

$$\begin{aligned}
 c_2 &= b \int_{h_I/2}^{h_I/2+h_A} (z - z_n) dz = \frac{b}{2} \left[ \left( \frac{h_I}{2} + h_A \right)^2 - \left( \frac{h_I}{2} \right)^2 \right] \\
 c_3 &= b \int_{h_I/2}^{h_I/2+h_A} (z - z_n)^2 dz = \frac{b}{3} \left[ \left( \frac{h_I}{2} + h_A \right)^3 - \left( \frac{h_I}{2} \right)^3 \right].
 \end{aligned}
 \tag{7.45}$$

### Strong and Weak Forms of the Beam Model

Because the general equations of motion (7.41) and moment relations (7.43) are identical to those for the unimorph, the strong and weak forms of the models also agree, with geometry differences incorporated through the parameters  $\rho$ ,  $YI$ ,  $cI$  and  $k_p$  defined in (7.42) and (7.44). Hence the strong formulation of the model is given by (7.38) where it is noted that differentiation of the spatially-dependent parameters yields Dirac distributions at the patch edges. This is alleviated in the weak formulations (7.39) and (7.40) which simply involve differing material coefficients in the regions covered by and devoid of patches. When implementing the numerical methods of Section 8.2, one needs to ensure that the spline or finite element grid coincides with the patch edges to retain optimal convergence rates.

## 7.5 Plate Models

The rod and beam models developed in Sections 7.3 and 7.4 quantify the in-plane and out-of-plane motion of structures whose width is sufficiently small compared with the length that suitable accuracy is obtained by considering motion only as a function of length. In this section, we summarize the development of 2-D plate models quantifying the in-plane and out-of-plane motion in both the  $x$  and  $y$ -coordinates.

### 7.5.1 Rectangular Plate

We consider a plate of length  $\ell$ , width  $a$ , and thickness  $h_I$  and let  $\Omega = [0, \ell] \times [0, a]$  denote the support of the plate. We assume that  $N_A$  PZT patch pairs having thickness  $h_A$  are mounted on the surface of the plate with edges parallel to the  $x$  and

$y$ -axes as depicted in Figure 7.17. The regions covered by the patches are denoted by  $\Omega_1, \dots, \Omega_{N_A}$ . As in previous sections, the subscripts  $I$  and  $A$  on the density  $\rho$ , Young's modulus  $Y$ , and Kelvin–Voigt damping parameter  $c$  designate plate and patch values. The air damping coefficient is denoted by  $\gamma$  and the displacements of the reference surface in the  $x$ ,  $y$  and  $z$  directions are respectively denoted by  $u$ ,  $v$  and  $w$ . Finally, distributed forces are denoted by  $\mathbf{f} = f_x \hat{\mathbf{i}}_x + f_y \hat{\mathbf{i}}_y + f_n \hat{\mathbf{i}}_n$ .

### Force and Moment Balancing

When balancing forces and moments for an infinitesimal plate element, it is advantageous to employ the resultants in differential form and having the orientation depicted in Figure 7.18.<sup>32</sup> The differential notation is equivalent in the limit to the resultant convention employed in Sections 7.3 and 7.4 but simplifies both the 2-D balance of forces and moments and formulation of the deformed reference surface when constructing the nonlinear von Kármán plate model as summarized in Section 7.8.

#### Force Balancing

The balance of forces in the  $x$ -direction in combination with Newton's second law yields

$$\rho \frac{\partial^2 u}{\partial t^2} dx dy = \left( N_x + \frac{\partial N_x}{\partial x} dx \right) dy - N_x dy + \left( N_{yx} + \frac{\partial N_{yx}}{\partial y} dy \right) dx - N_{yx} dx + \hat{f}_x dx dy$$

which implies that

$$\rho \frac{\partial^2 u}{\partial t^2} - \frac{\partial N_x}{\partial x} - \frac{\partial N_{yx}}{\partial y} = f_x. \tag{7.46}$$

The equilibrium equations

$$\rho \frac{\partial^2 v}{\partial t^2} - \frac{\partial N_y}{\partial y} - \frac{\partial N_{xy}}{\partial x} = f_y \quad , \quad \rho \frac{\partial^2 w}{\partial t^2} - \frac{\partial Q_x}{\partial x} - \frac{\partial Q_y}{\partial y} = f_n \tag{7.47}$$

<sup>32</sup>See Footnote 30 on page 316 for discussion regarding the moment convention.

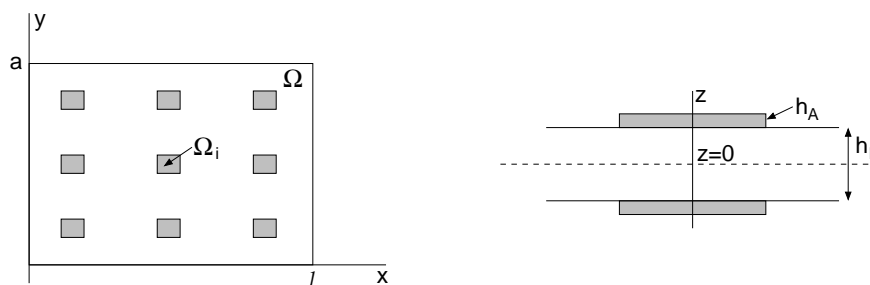


**Figure 7.17.** Plate of length  $\ell$ , width  $a$ , and thickness  $h_I$  with PZT actuators of thickness  $h_A$  covering the regions  $\Omega_1, \dots, \Omega_{N_A}$ . Due to symmetry, the neutral surface  $z_n$  corresponds with the centerline  $z = 0$ .

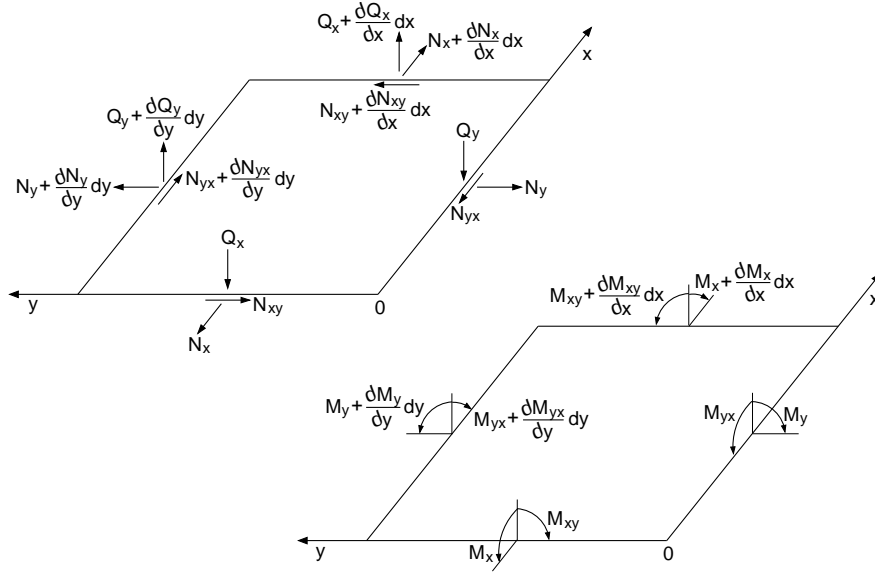


**Figure 7.18.** Force and moment resultants for the infinitesimal plate element.

in the  $y$  and  $z$ -directions are derived in a similar manner. In all of these relations, the composite density is given by

$$\rho(x, y) = \rho_I h_I + 2 \sum_{i=1}^{N_A} \chi_{pe_i}(x, y) \rho_A h_A \quad (7.48)$$

where the characteristic function

$$\chi_{pe_i}(x, y) = \begin{cases} 1 & , (x, y) \in \Omega_i \\ 0 & , (x, y) \notin \Omega_i \end{cases} \quad (7.49)$$

isolates the region covered the the  $i^{th}$  patch pair.

**Moment Balancing**

Moments are balanced with respect to a reference point which we choose as the point 0 in Figure 7.18. The balancing of moments with respect to  $y$  yields

$$\begin{aligned} & \left( M_x + \frac{\partial M_x}{\partial x} dx \right) dy - M_x dy - \left( Q_x + \frac{\partial Q_x}{\partial x} dx \right) dy dx \\ & + \left( M_{yx} + \frac{\partial M_{yx}}{\partial y} dy \right) dx - M_{yx} dx + Q_y \frac{dx}{2} dx \\ & - \left( Q_y + \frac{\partial Q_y}{\partial y} dy \right) dx \frac{dx}{2} + \hat{f}_n dx dy \frac{dx}{2} = 0. \end{aligned}$$

Retention of first-order terms in accordance with Assumption 2 of Section 7.2 yields the equilibrium equation

$$\frac{\partial M_x}{\partial x} + \frac{\partial M_{yx}}{\partial y} - Q_x = 0. \quad (7.50)$$

In a similar manner, the relations

$$\frac{\partial M_y}{\partial y} + \frac{\partial M_{xy}}{\partial x} - Q_y = 0 \quad (7.51)$$

and

$$N_{xy} - N_{yx} = 0 \quad (7.52)$$

are determined by balancing moments with respect to  $x$  and  $z$ . It will be shown that due to the symmetry of the stress tensor,  $N_{xy} = N_{yx}$  so (7.52) is automatically satisfied.

The uncoupled equations of motion can then be formulated as

$$\begin{aligned} \rho \frac{\partial^2 u}{\partial t^2} - \frac{\partial N_x}{\partial x} - \frac{\partial N_{yx}}{\partial y} &= f_x \\ \rho \frac{\partial^2 v}{\partial t^2} - \frac{\partial N_y}{\partial y} - \frac{\partial N_{xy}}{\partial x} &= f_y \\ \rho \frac{\partial^2 w}{\partial t^2} - \frac{\partial^2 M_x}{\partial x^2} - \frac{\partial^2 M_y}{\partial y^2} - \frac{\partial^2 M_{yx}}{\partial x \partial y} - \frac{\partial^2 M_{xy}}{\partial x \partial y} &= f_n. \end{aligned} \quad (7.53)$$

We next formulate the strain-displacement and stress-strain relations necessary to pose (7.53) in terms of the state variables  $u$ ,  $v$  and  $w$ .

### Resultant Formulation

The definitions of the force and moment resultants are the same as the 1-D definitions employed in Sections 7.3 and 7.4 when deriving rod and beam equations so we simply summarize here requisite 2-D relations. For the considered symmetric geometry, the reference surface  $z_n$  is the unperturbed middle surface so  $z_n = 0$ . Extension of the model to nonsymmetric structures is accomplished using theory analogous to that of Section 7.4.1.

### Stress-Strain Relations

We summarize first constitutive relations which relate the normal strains  $\varepsilon_x, \varepsilon_y$  and shear strains  $\varepsilon_{xy}, \varepsilon_{yx}$  at arbitrary points in the plate to normal stresses  $\sigma_x, \sigma_y$  and shear stresses  $\sigma_{xy}, \sigma_{yx}$  having the orientation shown in Figure 7.19. This is accomplished using (7.2) or (7.4) with  $\alpha = x$  and  $\beta = y$ . As detailed in [33, 291], symmetry of the stress tensor dictates that  $\sigma_{xy} = \sigma_{yx}$  so we focus on relations for the first three pairs. Finally, we focus initially on the linear input relations (7.2), which provide suitable accuracy for a number of smart material applications, but note that identical analysis applies for the nonlinear input relations (7.4).

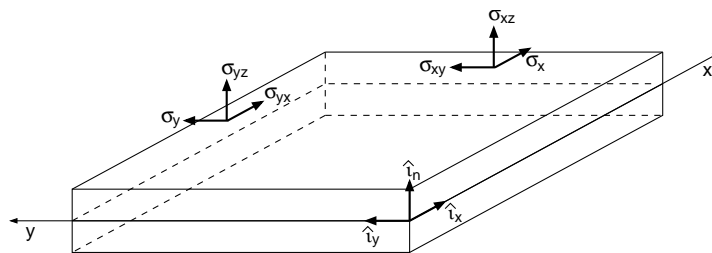


**Figure 7.19.** Orientation of normal stresses  $\sigma_x, \sigma_y$  and shear stresses  $\sigma_{xy}, \sigma_{yx}, \sigma_{xz}, \sigma_{yz}$ . The convention for normal and shear strains is analogous.

From the first relation in (7.2), it follows that

$$\sigma_x = \begin{cases} \sigma_{xI} & , \text{ Plate } (|z| < \frac{h_I}{2}) \\ \sigma_{xA} & , \text{ Patch } (\frac{h_I}{2} \leq |z| \leq \frac{h_I}{2} + h_A) \end{cases}$$

where

$$\begin{aligned} \sigma_{xI} &= \frac{Y_I}{1 - \nu_I^2} (\varepsilon_x + \nu_I \varepsilon_y) + \frac{c_I}{1 - \nu_I^2} (\dot{\varepsilon}_x + \nu_I \dot{\varepsilon}_y) \\ \sigma_{xA} &= \frac{Y_A}{1 - \nu_A^2} (\varepsilon_x + \nu_A \varepsilon_y) + \frac{c_A}{1 - \nu_A^2} (\dot{\varepsilon}_x + \nu_A \dot{\varepsilon}_y) - \frac{Y_A d_{31}}{h_A (1 - \nu_A)} V. \end{aligned} \tag{7.54}$$

The relations for  $\sigma_y$  and  $\sigma_{xy} = \sigma_{yx}$  follow in a similar manner. Nonlinear input relations are obtained through identical analysis using the polarization relation (7.4).

### Strain-Displacement Relations

A fundamental tenet of thin beam, plate and shell theory is that motion is quantified in terms of displacements and rotation of the reference surface. To accomplish, we let  $e_x, e_y$  and  $e_{xy}, e_{yx}$  respectively denote normal and shear strains of the reference surface  $z_n$ . Moreover,  $\kappa_x, \kappa_y$  and  $\kappa_{xy}$  respectively denote changes in the curvature and twist of the reference surface.

By invoking Assumption 4 of Section 7.2, the strains  $\varepsilon_x, \varepsilon_y, \varepsilon_{xy}$  at arbitrary positions  $z$  in the plate can be expressed as

$$\begin{aligned} \varepsilon_x &= e_x + \kappa_x z \\ \varepsilon_y &= e_y + \kappa_y z \\ \varepsilon_{xy} &= e_{xy} + \kappa_{xy} z. \end{aligned} \tag{7.55}$$

As depicted in Figure 7.20, the first term in each relation quantifies in-plane strains whereas the second characterizes strains due to bending.

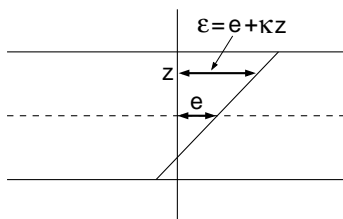


**Figure 7.20.** Representative strain profile comprised of an in-plane component  $e$  and bending component  $\kappa z$ .

Extension of the strain definition (7.11) and curvature relation (7.32) to 2-D subsequently yields the kinematic relations

$$e_x = \frac{\partial u}{\partial x} \quad , \quad e_y = \frac{\partial v}{\partial y} \quad , \quad e_{xy} = \frac{\partial v}{\partial x} + \frac{\partial u}{\partial y} \quad (7.56)$$

$$\kappa_x = -\frac{\partial^2 w}{\partial x^2} \quad , \quad \kappa_y = -\frac{\partial^2 w}{\partial y^2} \quad , \quad \kappa_{xy} = -2\frac{\partial^2 w}{\partial x \partial y}.$$

The combination of (7.55) and (7.56) provides relations which quantify the general strains employed in stress-strain relations — e.g., (7.54) — in terms of displacement properties of the reference surface.

#### Force and Moment Resultants — General Relations

The force resultants  $N_x, N_y, N_{xy} = N_{yx}$  and moment resultants  $M_x, M_y, M_{xy} = M_{yx}$  are defined in a manner analogous to (7.9) and (7.29). Inclusion of the patch properties and inputs yields the general relations

$$\begin{aligned} \begin{bmatrix} N_x \\ N_y \\ N_{xy} \end{bmatrix} &= \int_{-h_I/2}^{h_I/2} \begin{bmatrix} \sigma_{x_I} \\ \sigma_{y_I} \\ \sigma_{xy_I} \end{bmatrix} dz + \sum_{i=1}^{N_A} \chi_{pe_i}(x, y) \left( \int_{h_I/2}^{h_I/2+h_A} \begin{bmatrix} \sigma_{x_A} \\ \sigma_{y_A} \\ \sigma_{xy_A} \end{bmatrix} dz \right. \\ &\quad \left. + \int_{-h_I/2-h_A}^{-h_I/2} \begin{bmatrix} \sigma_{x_A} \\ \sigma_{y_A} \\ \sigma_{xy_A} \end{bmatrix} dz \right) \\ \begin{bmatrix} M_x \\ M_y \\ M_{xy} \end{bmatrix} &= \int_{-h_I/2}^{h_I/2} \begin{bmatrix} \sigma_{x_I} \\ \sigma_{y_I} \\ \sigma_{xy_I} \end{bmatrix} z dz + \sum_{i=1}^{N_A} \chi_{pe_i}(x, y) \left( \int_{h_I/2}^{h_I/2+h_A} \begin{bmatrix} \sigma_{x_A} \\ \sigma_{y_A} \\ \sigma_{xy_A} \end{bmatrix} z dz \right. \\ &\quad \left. + \int_{-h_I/2-h_A}^{-h_I/2} \begin{bmatrix} \sigma_{x_A} \\ \sigma_{y_A} \\ \sigma_{xy_A} \end{bmatrix} z dz \right) \end{aligned}$$

where the characteristic function is defined in (7.49). From (7.54), it is observed that the stresses have elastic, damping, and external components; hence the resultants

can be expressed as

$$\begin{aligned}
 N_x &= N_{x_e} + N_{x_d} + N_{x_{ext}} & , & \quad M_x = M_{x_e} + M_{x_d} + M_{x_{ext}} \\
 N_y &= N_{y_e} + N_{y_d} + N_{y_{ext}} & , & \quad M_y = M_{y_e} + M_{y_d} + M_{y_{ext}} \\
 N_{xy} &= N_{xy_e} + N_{xy_d} + N_{xy_{ext}} & , & \quad M_{xy} = M_{xy_e} + M_{xy_d} + M_{xy_{ext}}
 \end{aligned} \tag{7.57}$$

where the subscripts  $e, d$  and  $ext$  respectively indicate elastic, damping and external components.

*Force and Moment Resultants — Elastic Components*

For the case under consideration, the symmetry of patch pairs simplifies the resultant formulation and yields

$$\begin{aligned}
 N_{x_e} &= \frac{Y_I h_I}{1 - \nu_I^2} (e_x + \nu_I e_y) + \frac{2Y_A h_A}{1 - \nu_A^2} (e_x + \nu_A e_y) \sum_{i=1}^{N_A} \chi_{pe_i}(x, y) \\
 N_{y_e} &= \frac{Y_I h_I}{1 - \nu_I^2} (e_y + \nu_I e_x) + \frac{2Y_A h_A}{1 - \nu_A^2} (e_y + \nu_A e_x) \sum_{i=1}^{N_A} \chi_{pe_i}(x, y) \\
 N_{xy_e} &= \frac{Y_I h_I}{2(1 + \nu_I)} e_{xy} + \frac{Y_A h_A}{1 + \nu_A} e_{xy} \sum_{i=1}^{N_A} \chi_{pe_i}(x, y) \\
 M_{x_e} &= \frac{Y_I h_I^3}{12(1 - \nu_I^2)} (\kappa_x + \nu_I \kappa_y) + \frac{2Y_A c_3}{1 - \nu_A^2} (\kappa_x + \nu_A \kappa_y) \sum_{i=1}^{N_A} \chi_{pe_i}(x, y) \\
 M_{y_e} &= \frac{Y_I h_I^3}{12(1 - \nu_I^2)} (\kappa_y + \nu_I \kappa_x) + \frac{2Y_A c_3}{1 - \nu_A^2} (\kappa_y + \nu_A \kappa_x) \sum_{i=1}^{N_A} \chi_{pe_i}(x, y) \\
 M_{xy_e} &= \frac{Y_I h_I^3}{24(1 + \nu_I)} \kappa_{xy} + \frac{Y_A c_3}{1 + \nu_A} \kappa_{xy} \sum_{i=1}^{N_A} \chi_{pe_i}(x, y)
 \end{aligned} \tag{7.58}$$

where  $e_x, e_y, e_{xy}, \kappa_x, \kappa_y, \kappa_{xy}$  are defined in (7.56) and  $c_3 = \int_{h_I/2}^{h_I/2+h_A} (z - z_n)^2 dz$  is given in (7.45). For more general constructs, the same techniques are applied but the final expressions will reflect geometry-dependencies.

*Force and Moment Resultants — Internal Damping Components*

The resultant components that incorporate the Kelvin–Voigt damping have the same form as the elastic components but involve the temporal derivatives of

strains and rotations; for example

$$\begin{aligned}
 N_{x_d} &= \frac{Y_I h_I}{1 - \nu_I^2} (\dot{e}_x + \nu_I \dot{e}_y) + \frac{2Y_A h_A}{1 - \nu_A^2} (\dot{e}_x + \nu_A \dot{e}_y) \sum_{i=1}^{N_A} \chi_{pe_i}(x, y) \\
 M_{x_d} &= \frac{Y_I h_I^3}{12(1 - \nu_I^2)} (\dot{\kappa}_x + \nu_I \dot{\kappa}_y) + \frac{2Y_A c_3}{1 - \nu_A^2} (\dot{\kappa}_x + \nu_A \dot{\kappa}_y) \sum_{i=1}^{N_A} \chi_{pe_i}(x, y)
 \end{aligned}
 \tag{7.59}$$

with analogous expressions for  $N_{y_d}$ ,  $N_{xy_d}$ ,  $M_{y_d}$  and  $M_{xy_d}$ .

*Force and Moment Resultants — External Components*

Consider first the external components that result from the linear input relations (7.2) when voltages  $V_{1i}(t)$  and  $V_{2i}(t)$  are respectively applied to the inner and outer patches in the  $i^{th}$  pair. Integration through the patch thickness yields

$$\begin{aligned}
 N_{x_{ext}} = N_{y_{ext}} &= \frac{-Y_A d_{31}}{1 - \nu_A} \sum_{i=1}^{N_A} [V_{1i}(t) + V_{2i}(t)] \chi_{pe_i}(x, y) \\
 N_{xy_{ext}} = N_{yx_{ext}} &= 0 \\
 M_{x_{ext}} = M_{y_{ext}} &= \frac{-Y_A d_{31} c_2}{h_A (1 - \nu_A)} \sum_{i=1}^{N_A} [V_{1i}(t) + V_{2i}(t)] \chi_{pe_i}(x, y) \\
 M_{xy_{ext}} = M_{yx_{ext}} &= 0
 \end{aligned}
 \tag{7.60}$$

where  $c_2 = \int_{h_I/2}^{h_I/2+h_A} (z - z_n) dz$  is defined in (7.45).

It is observed that if equal voltages  $V_i(t) = V_{1i}(t) = V_{2i}(t)$  are applied to the patches, then

$$\begin{aligned}
 N_{x_{ext}} = N_{y_{ext}} &= \frac{-2Y_A d_{31}}{1 - \nu_A} \sum_{i=1}^{N_A} V_i(t) \chi_{pe_i}(x, y) \\
 N_{xy_{ext}} = N_{yx_{ext}} = M_{x_{ext}} = M_{y_{ext}} = M_{xy_{ext}} = M_{yx_{ext}} &= 0
 \end{aligned}
 \tag{7.61}$$

which produces solely in-plane motion. Alternatively, if  $V_i(t) = V_{1i}(t) = -V_{2i}(t)$ , only bending moments

$$M_{x_{ext}} = M_{y_{ext}} = \frac{-2Y_A d_{31} c_2}{h_A (1 - \nu_A)} \sum_{i=1}^{N_A} V_i(t) \chi_{pe_i}(x, y)
 \tag{7.62}$$

are produced and the plate will exhibit transverse or out-of-plane motion. This is analogous to the drive regimes which provide in-plane and out-of-plane motion in the rod and beam models discussed in Sections 7.3 and 7.4.

The formulation of the external resultants for the nonlinear input relations (7.4) is analogous and yields

$$N_{x_{ext}} = N_{y_{ext}} = \frac{-h_A}{1 - \nu_A} \sum_{i=1}^{N_A} [a_1(P_{1i}(t) + P_{2i}(t) - 2P_R) + a_2((P_{1i}(t) - P_R)^2 + (P_{2i}(t) - P_R)^2)] \chi_{pe_i}(x, y) \quad (7.63)$$

$$M_{x_{ext}} = M_{y_{ext}} = \frac{-c_2}{1 - \nu_A} \sum_{i=1}^{N_A} [a_1(P_{1i}(t) - P_{2i}(t) - 2P_R) + a_2((P_{1i}(t) - P_R)^2 - (P_{2i}(t) - P_R)^2)] \chi_{pe_i}(x, y)$$

where  $P_{1i}, P_{2i}$  are the polarizations modeled by (7.4) or (2.114) in response to input fields  $E_{1i}, E_{2i}$  applied to the inner and outer patches in each pair. We note that in this case,  $E_i = E_{1i} = E_{2i}$  and  $E_i = E_{1i} = -E_{2i}$  do not produce solely in-plane force and out-of-plane bending due the asymmetry of the  $E$ - $\varepsilon$  relation about  $E = 0$  — e.g., see Figure 2.10(b). For low drive levels, however, the  $E$ - $\varepsilon$  relation is approximately linear which leads to (7.61) and (7.62) resulting from the linear input model.

### Boundary Conditions and Strong Model Formulation

Appropriate boundary conditions are determined by the requirement that no work is performed along the plate edge. To illustrate, consider the edge  $x = 0$ ,  $0 \leq y \leq a$ . The work during deformation can be expressed as

$$W = \int_0^a [N_x u + N_{xy} v + Q_x w + M_{xy} \theta_y + M_x \theta_x] dy \quad (7.64)$$

where the rotations of the normal to the reference surface are approximated by

$$\theta_x = \frac{\partial w}{\partial x} \quad , \quad \theta_y = \frac{\partial w}{\partial y}.$$

Integration by parts gives

$$\int_0^a \left[ N_x u + N_{xy} v + \left( Q_x - \frac{\partial M_{xy}}{\partial y} \right) w + M_x \frac{\partial w}{\partial x} \right] dy + M_{xy} w \Big|_0^a = 0$$

which yields the boundary conditions

$$u = 0 \quad \text{or} \quad N_x = 0$$

$$v = 0 \quad \text{or} \quad N_{xy} = 0$$

$$w = 0 \quad \text{or} \quad Q_x - \frac{\partial M_{xy}}{\partial y} = 0$$

$$\frac{\partial w}{\partial x} = 0 \quad \text{or} \quad M_x = 0$$

and  $M_{xy} w \Big|_0^a = 0$ .

Analogous conditions hold for edges parallel to the  $y$ -axis. We point out that the first condition in each relation constitutes an *essential boundary condition* which must be enforced when constructing spaces of test functions  $V$  whereas the second is a *natural boundary condition* that is automatically satisfied by solutions to the weak formulation of the model.

Common boundary conditions employed when modeling smart material systems include the following.

(a) Clamped or fixed edge:

$$u = v = w = \frac{\partial w}{\partial x} = 0$$

(b) Free edge:

$$N_x = N_{xy} = \left( Q_x + \frac{\partial M_{xy}}{\partial y} \right) = M_x = 0$$

(c) Simply supported edge, not free to move:

$$u = v = w = M_x = 0$$

(d) Simply supported edge, free to move in  $x$  direction:

$$u = w = M_x = N_x = 0$$

The *shear diaphragm* condition (d) is popular from a theoretical perspective since it admits analytic solution for plates devoid of patches. For applications, however, the boundary conditions (a)–(c) typically provide a better approximation to physical conditions, thus necessitating the use of approximation techniques of the type discussed in Section 8.3.

For physical clamping conditions which dissipate energy, boundary conditions analogous to (7.13) can be developed through force balancing as summarized in Section 7.5.2 and detailed in [291].

The strong formulation of the model is then given by (7.53) with the general resultants specified by (7.57) and elastic, damping and external components specified by (7.58), (7.59) and (7.60) or (7.63).

### Weak Model Formulation

From the perspective of approximation, the strong formulation of the model poses the same difficulties noted in Sections 7.3 and 7.4; namely, spatial differentiation of piecewise constant material parameters and inputs yields Dirac distributions and derivatives of Dirac distributions at actuator boundaries. This can severely impede the convergence of approximation techniques applied directly to the strong model formulation.

These difficulties are eliminated in weak formulations of the model obtained either through energy principles analogous to those detailed in Section 7.3.2 or direct integration by parts. The state  $\xi(t) = (u(t, \cdot, \cdot), v(t, \cdot, \cdot), w(t, \cdot, \cdot))$  is considered in the state space

$$X = L^2(\Omega) \times L^2(\Omega) \times L^2(\Omega)$$

where  $\Omega = [0, \ell] \times [0, a]$  denotes the plate region. The space of test functions is taken to be

$$V = H_b^1(\Omega) \times H_b^1(\Omega) \times H_b^2(\Omega)$$

where  $H_b^1$  and  $H_b^2$  are subsets of  $H^1$  and  $H^2$  restricted to those functions which satisfy essential boundary conditions.

A weak formulation is

$$\begin{aligned} \int_{\Omega} \left\{ \rho \frac{\partial^2 u}{\partial t^2} \phi_1 + N_x \frac{\partial \phi_1}{\partial x} + N_{yx} \frac{\partial \phi_1}{\partial y} - f_x \phi_1 \right\} d\omega &= 0 \\ \int_{\Omega} \left\{ \rho \frac{\partial^2 v}{\partial t^2} \phi_2 + N_y \frac{\partial \phi_2}{\partial y} + N_{xy} \frac{\partial \phi_2}{\partial x} - f_y \phi_2 \right\} d\omega &= 0 \\ \int_{\Omega} \left\{ \rho \frac{\partial^2 w}{\partial t^2} \phi_3 - M_x \frac{\partial^2 \phi_3}{\partial x^2} - 2M_{xy} \frac{\partial^2 \phi_3}{\partial x \partial y} - M_y \frac{\partial^2 \phi_3}{\partial y^2} - f_n \phi_3 \right\} d\omega &= 0 \end{aligned} \tag{7.65}$$

which must be satisfied for all  $\Phi = (\phi_1, \phi_2, \phi_3) \in V$ . The resultants are given by (7.57) with components defined in (7.58), (7.59) and (7.60) or (7.63).

As will be noted in Section 8.3, the approximation of  $u$  and  $v$  can be accomplished with linear finite elements whereas cubic Hermite elements or cubic B-splines are required to accommodate the second derivatives in the equation for  $w$ .

The differential equations are uncoupled, even for general voltages/fields and nonlinear and hysteretic input regimes. This is in contrast to the *nonlinear* von Kármán model summarized in Section 7.8 which incorporates coupling between in-plane and out-of-plane motion. As noted previously, only  $u$  and  $v$  vibrations are produced when equal voltages  $V_i(t) = V_{1i}(t) = V_{2i}(t)$  are applied to the linear input relations whereas transverse motion modeled by the  $w$  relation is generated by diametrically out-of-phase voltages  $V_i(t) = V_{1i}(t) = -V_{2i}(t)$ . In high drive regimes, all three components of the motion are excited due to the asymmetry of the  $E$ - $\varepsilon$  relation about  $E = 0$  as manifested by the external resultant relations (7.63).

### 7.5.2 Circular Plate Model

Circular plates with circular or sectoral patches comprise a second common geometry in smart material applications. For modeling purposes, we consider a plate of radius  $a$  and thickness  $h_I$  with surface-mounted patches of thickness  $h_A$  placed in pairs as depicted in Figure 7.17(b). The region  $\Omega = [0, a] \times [0, 2\pi]$  delineates the plate region and the  $N_A$  regions covered by patch pairs are indicated by  $\Omega_i$ .

The fundamental principles employed for model development are the same as those detailed in Section 7.5.1 for rectangular plates and we summarize here only the primary relations to illustrated geometry-induced differences. Details regarding the theory of circular plates can be found in [33, 291]. Finally, we consider only transverse vibrations since they comprise the primary response in many applications employing circular plates having fully clamped edges.

### Force and Moment Balancing

The balance of moments with respect to  $r$  and  $\theta$  yields

$$\begin{aligned} \frac{1}{r} \frac{\partial M_\theta}{\partial \theta} + \frac{\partial M_{r\theta}}{\partial r} + \frac{2}{r} M_{r\theta} - Q_\theta &= 0 \\ \frac{1}{r} M_r + \frac{\partial M_r}{\partial r} - \frac{1}{r} M_\theta + \frac{1}{r} \frac{\partial M_{\theta r}}{\partial \theta} - Q_r &= 0 \end{aligned}$$

whereas force balancing yields

$$\rho \frac{\partial^2 w}{\partial t^2} - \frac{1}{r} Q_r - \frac{\partial Q_r}{\partial r} - \frac{1}{r} \frac{\partial Q_\theta}{\partial \theta} = f_n.$$

The synthesis of these relations yields the dynamic model

$$\rho \frac{\partial^2 w}{\partial t^2} - \frac{\partial^2 M_r}{\partial r^2} - \frac{2}{r} \frac{\partial M_r}{\partial r} + \frac{1}{r} \frac{M_\theta}{\partial r} - \frac{2}{r} \frac{\partial^2 M_{r\theta}}{\partial r \partial \theta} - \frac{2}{r^2} \frac{\partial M_{r\theta}}{\partial \theta} - \frac{1}{r^2} \frac{\partial^2 M_\theta}{\partial \theta^2} = f_n.$$

The density  $\rho$  has the form (7.48) to incorporate the differing material properties in regions covered by the patches.

### Resultant Evaluation

The constitutive relations (7.2) and (7.4) and general strain relations (7.55) are independent of geometry so we employ them directly modulo a change of coordinates from  $(x, y)$  to  $(r, \theta)$ . Since we are considering only transverse vibrations, we have  $e_r = e_\theta = e_{r\theta} = 0$  for the reference surface strains and hence only consider the curvature changes

$$\begin{aligned} \kappa_r &= -\frac{\partial^2 w}{\partial r^2} \\ \kappa_\theta &= -\frac{1}{r} \frac{\partial w}{\partial r} - \frac{1}{r^2} \frac{\partial^2 w}{\partial \theta^2} \\ \kappa_{r\theta} &= -\frac{\partial}{\partial r} \left( \frac{\partial w}{\partial \theta} \right) \end{aligned} \tag{7.66}$$

in the kinematic relations (7.55). The elastic, damping and external components in the general resultant relations

$$\begin{aligned} M_r &= M_{r_e} + M_{r_d} + M_{r_{ext}} \\ M_\theta &= M_{\theta_e} + M_{\theta_d} + M_{\theta_{ext}} \\ M_{r\theta} &= M_{r\theta_e} + M_{r\theta_d} + M_{r\theta_{ext}} \end{aligned} \tag{7.67}$$

are defined as follows.

*Elastic Components*

The elastic components of the bending resultants are

$$M_{r_e} = \frac{Y_I h_I^3}{12(1 - \nu_I^2)} (\kappa_r + \nu_I \kappa_\theta) + \frac{2Y_A c_3}{1 - \nu_A^2} (\kappa_r + \nu_A \kappa_\theta) \sum_{i=1}^{N_A} \chi_{pe_i}(r, \theta)$$

$$M_{y_{\theta_e}} = \frac{Y_I h_I^3}{12(1 - \nu_I^2)} (\kappa_\theta + \nu_I \kappa_r) + \frac{2Y_A c_3}{1 - \nu_A^2} (\kappa_\theta + \nu_A \kappa_r) \sum_{i=1}^{N_A} \chi_{pe_i}(r, \theta)$$

$$M_{r_{\theta_e}} = \frac{Y_I h_I^3}{24(1 + \nu_I)} \kappa_{r\theta} + \frac{Y_A c_3}{1 + \nu_A} \kappa_{r\theta} \sum_{i=1}^{N_A} \chi_{pe_i}(r, \theta)$$

where  $\kappa_r, \kappa_\theta$  and  $\kappa_{r\theta}$  are defined in (7.66) and  $c_3 = \int_{h_I/2}^{h_I/2+h_A} (z - z_n)^2 dz$  is given by (7.45).

*Damping Components*

The damping components involve strain rates rather than strains and are

$$M_{r_d} = \frac{c_I h_I^3}{12(1 - \nu_I^2)} (\dot{\kappa}_r + \nu_I \dot{\kappa}_\theta) + \frac{2c_A c_3}{1 - \nu_A^2} (\dot{\kappa}_r + \nu_A \dot{\kappa}_\theta) \sum_{i=1}^{N_A} \chi_{pe_i}(r, \theta)$$

$$M_{\theta_d} = \frac{c_I h_I^3}{12(1 - \nu_I^2)} (\dot{\kappa}_\theta + \nu_I \dot{\kappa}_r) + \frac{2c_A c_3}{1 - \nu_A^2} (\dot{\kappa}_\theta + \nu_A \dot{\kappa}_r) \sum_{i=1}^{N_A} \chi_{pe_i}(r, \theta)$$

$$M_{r_{\theta_d}} = \frac{c_I h_I^3}{24(1 + \nu_I)} \dot{\kappa}_{r\theta} + \frac{c_A c_3}{1 + \nu_A} \dot{\kappa}_{r\theta} \sum_{i=1}^{N_A} \chi_{pe_i}(r, \theta)$$

*External Components*

The external components are analogous to (7.60) and (7.63) for the rectangular plate. Hence for linear and nonlinear inputs they are

$$M_{r_{ext}} = M_{\theta_{ext}} = \frac{-Y_A d_{31} c_2}{h_A (1 - \nu_A)} \sum_{i=1}^{N_A} [V_{1i}(t) + V_{2i}(t)] \chi_{pe_i}(r, \theta)$$

and

$$M_{r_{ext}} = M_{\theta_{ext}} = \frac{-c_2}{1 - \nu_A} \sum_{i=1}^{N_A} [a_1 (P_{1i}(t) - P_{2i}(t) - 2P_R) + a_2 ((P_{1i}(t) - P_R)^2 - (P_{2i}(t) - P_R)^2)] \chi_{pe_i}(r, \theta).$$

In both cases, the external twisting moments  $M_{r_\theta} = M_{\theta_r}$  are zero.

### Boundary Conditions

For physical devices with ideal clamps, zero slope and displacement are maintained around the plate perimeter yielding the fixed-edge condition

$$w(t, a, \theta) = \frac{\partial w}{\partial r}(t, a, \theta) = 0. \tag{7.68}$$

In applications, however, perfectly fixed-edge conditions are difficult to maintain and energy dissipation through the clamps often produces measured frequencies that are lower than predicted by (7.68). To incorporate dissipative edge motion, boundary deformations and rotations are considered to be governed by damped, elastic springs in a manner analogous to that employed when constructing the rod boundary condition (7.13). As detailed in [32,291], this yields the boundary moment conditions

$$\begin{aligned} \frac{1}{a}M_r(t, a, \theta) + \frac{\partial M_r}{\partial r}(t, a, \theta) \\ = -k_a w(t, a, \theta) - c_a \frac{\partial w}{\partial t}(t, a, \theta) - \rho \frac{\partial^2 w}{\partial t^2}(t, a, \theta) \end{aligned} \tag{7.69}$$

$$M_r(t, a, \theta) = k_p \frac{\partial w}{\partial r}(t, a, \theta) + c_p \frac{\partial^2 w}{\partial r \partial t}(t, a, \theta).$$

It is observed that if one divides by the stiffness coefficients  $k_a$  and  $k_p$  and takes  $k_a \rightarrow \infty$ ,  $k_p \rightarrow \infty$ , the dissipative boundary conditions (7.69) converge to the fixed-edge conditions (7.68). Alternatively, one obtains free-edge conditions in the absence of elastic, damping or inertial edge effects.

### Weak Model Formulation

Consider the circular plate model with the fixed-edge conditions (7.68). The state space and space of test functions are taken to be

$$X = L^2(\Omega)$$

and

$$V = H_0^2(\Omega) = \left\{ \phi \in H^2(\Omega) \mid \phi(a, \theta) = \frac{\partial \phi}{\partial r}(a, \theta) = 0 \right\} \tag{7.70}$$

with the usual inner products.

The weak or variational formulation of the model is

$$\begin{aligned} \int_{\Omega} \rho \frac{\partial^2 w}{\partial t^2} \phi_3 d\omega + \int_{\Omega} M_r \frac{\partial^2 \phi_3}{\partial r^2} d\omega + \int_{\Omega} \frac{1}{r^2} M_{\theta} \left( r \frac{\partial \phi_3}{\partial r} + \frac{\partial^2 \phi_3}{\partial \theta^2} \right) d\omega \\ + 2 \int_{\Omega} \frac{1}{r^2} M_{r\theta} \left( r \frac{\partial^2 \phi_3}{\partial r \partial \theta} - \frac{\partial \phi_3}{\partial \theta} \right) d\omega = \int_{\Omega} f_n \phi_3 d\omega \end{aligned} \tag{7.71}$$

which must be satisfied for all  $\phi_3 \in V$ . The differential is  $d\omega = r d\theta dr$ . Details regarding the weak model formulations for the dissipative boundary conditions (7.69) can be found in [32].

**Model Validation**

To illustrate the performance of the dynamic circular plate model (7.71), we consider the characterization of a circular aluminum plate with a single piezoceramic patch surface-mounted at the center of the plate as depicted in Figure 7.21. The plate had clamped boundary conditions, a radius of 9 in and a thickness of 0.05 in, and the PZT patch had a radius of 0.75 in and a thickness of 0.007 in (7 mils). Because the patch is small compared with the plate, in-plane motion due to the geometric asymmetry in the region covered by the patch is negligible and we consider only transverse vibrations generated by centered and noncentered strikes with an impact hammer. However, the patch contributions to the density (7.48) and resultant relations (7.67) are retained in the model, and it is illustrated in [33] that differing material properties are estimated in the region  $\Omega_i$  covered by the patch during model identification. Details regarding this example can be found in [30,33] and we provide here only a summary of two dynamic responses.

*Axisymmetric Response*

We consider first the characterization of axisymmetric dynamics excited by a centered strike with a soft-headed impact hammer. The resulting time history and frequency response measured with the centered accelerometer  $A_c = (0'', 0)$  are plotted in Figure 7.22. The measured force from the impact hammer was input to the discretized circular plate relation to obtain the modeled response. The frequency plot illustrates that four axisymmetric modes, having frequencies of 59.3, 227.8, 516.4 and 917.7 Hz were excited in the experiment. The model accurately quantifies the low frequency dynamics but overdamps at high frequencies which is characteristic of the Kelvin–Voigt damping model.

For numerous applications, however, the high frequency dynamics typically have low magnitude and are highly damped, thus minimizing their impact on control design. Moreover, for structural acoustic applications, high frequency structural modes exhibit minimal coupling with acoustic modes and hence they provide

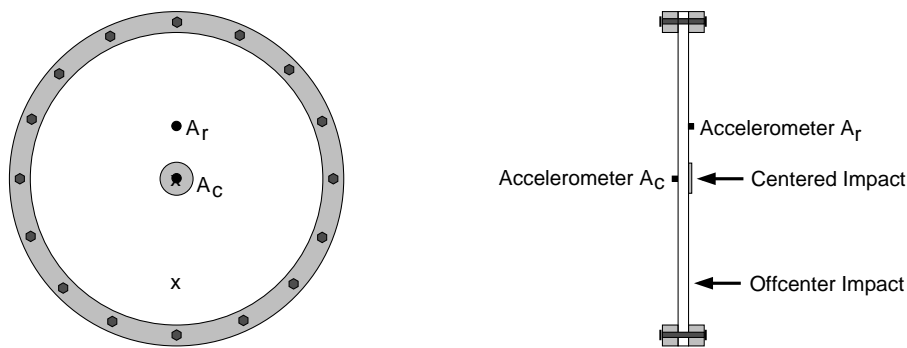


**Figure 7.21.** *Clamped circular plate with a single, centered, piezoceramic patch. Inputs were provided by centered and noncentered hammer impacts with acceleration measured at  $A_c = (0'', 0)$  and  $A_r = (2'', 0)$ .*

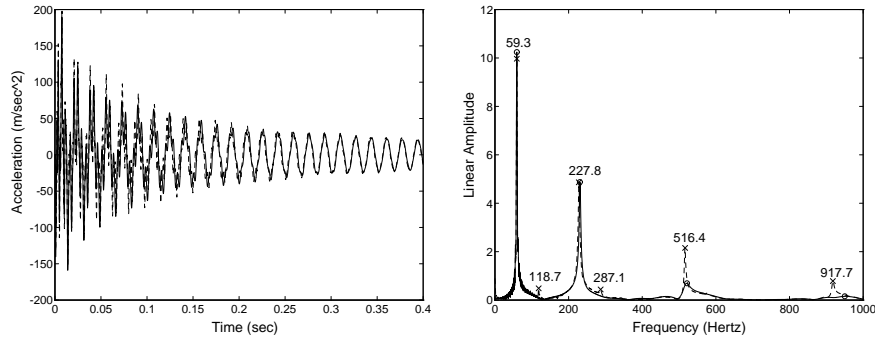


**Figure 7.22.** Time history and frequency content at  $A_c = (0'', 0)$  in response to a centered hammer impact: data (x - - -) and model (o —).

negligible contribution to structure-borne noise. Finally, feedback mechanisms can accommodate high frequency model limitations in model-based control designs. It is illustrated in [31, 33] that the circular plate model constructed in this manner can thus be employed for model-based LQG control design using the piezoceramic patch as an actuator.

*Nonaxisymmetric Response*

For axisymmetric regimes, the plate model (7.71) reduces to one spatial dimension. To demonstrate the 2-D nature of the model, we also illustrate the characterization of plate dynamics excited by a noncentered impact using a hard-tipped hammer at the point  $(7.27'', 0)$  depicted in Figure 7.21. The measured and modeled response at the point  $A_r = (2'', 0)$  are plotted in Figure 7.23. It is observed that the model accurately characterizes the  $(n, m) = (0, 0), (0, 2), (0, 3), (1, 1), (1, 2), (2, 0), (2, 1),$  and  $(0, 4)$  modes while underdamping the  $(1, 0)$  and  $(0, 1)$  modes and

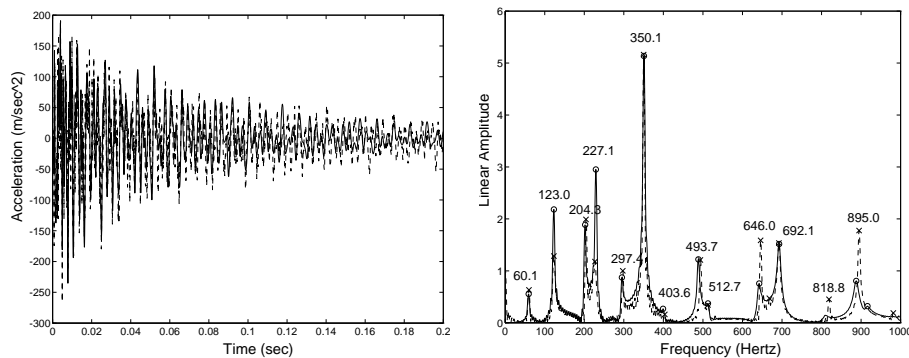


**Figure 7.23.** Time history and frequency content at  $A_r = (2'', 0)$  in response to a noncentered impact at  $(7.27'', 0)$ : data (x - - -) and model (o —).

overdamping higher frequency modes. Despite the limitation of the Kelvin–Voigt damping relation, the model accurately characterizes eight modes which provides ample accuracy for model-based control design.

## 7.6 Shell Models – General Development

The rod, beam and plate models developed in previous sections comprise special cases of shell models. This class of structures also includes the cylindrical, bi-spherical and general shell configurations arising in the AFM, structural acoustic, THUNDER, and jet engine applications depicted in Figure 7.1. A comprehensive discussion of model development for shells transcends the scope of this chapter and we provide here only a summary of the theory with the goal of providing readers with a framework from which to start when constructing models for specific smart material applications. Details regarding general shell theory can be found in Dym [145], Flügge [164], Love [301], Markuš [318], Novozhilov [364], Soedel [453] and Timoshenko and Woinowsky-Krieger [480] whereas discussion focused on piezoelectric shells or shells with piezoelectric actuators is provided in [485–487].

The analysis in Section 7.5 of in-plane and out-of-plane motion for plate structures illustrates the moment and force balancing principles, constitutive stress-strain relations, and kinematic strain-displacement tenets used to construct models for 2-D composite structures comprised of both active and inactive components. The extensions required to incorporate curvature-induced coupling are geometric in nature and do not affect the fundamental constitutive behavior. Hence to simplify the discussion, we consider in this section the passive dynamics of undamped, homogeneous structures. Once the general geometric relations are established, the inclusion of damping and external inputs follows in a manner analogous to that detailed in Section 7.5 for plates. This will be further illustrated in Section 7.7 where the special cases of cylindrical shells and curved beams are considered.

### 7.6.1 Shell Coordinates

We consider a homogeneous thin structure of width  $h$  so that the reference surface  $z_n$  coincides with the unperturbed middle surface,  $z_n = 0$ , as depicted in Figure 7.24. From Assumption 4 of Section 7.2, it follows that the behavior at any point in the shell is quantified in terms of the motion of the reference surface so we begin there when specifying coordinates. Consider an orthogonal, curvilinear coordinate system on the reference surface chosen to coincide with lines of principle curvature. The third coordinate direction is chosen perpendicular to the reference surface through the shell thickness. The coordinates in the three directions are denoted  $\alpha, \beta$  and  $z$ . If we designate the reference surface by

$$z_n = r(\alpha, \beta),$$

arbitrary points in the shell can be specified by

$$R(\alpha, \beta, z) = r(\alpha, \beta) + z\hat{i}_n$$

where  $\hat{i}$  is the unit vector normal to the reference surface.

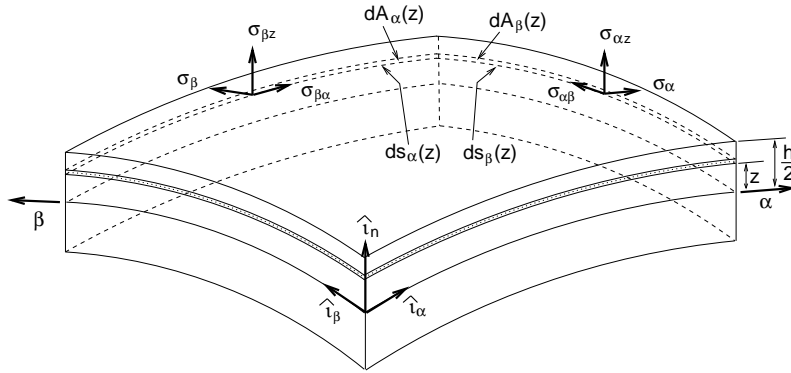


**Figure 7.24.** *Fundamental shell element in the  $(\alpha, \beta)$  coordinate system.*

The radii of curvature in the  $\alpha$  and  $\beta$  directions are denoted by  $R_\alpha$  and  $R_\beta$  and Lamé constants  $A$  and  $B$  are defined by

$$A^2 = \frac{\partial r}{\partial \alpha} \cdot \frac{\partial r}{\partial \alpha} \quad , \quad B^2 = \frac{\partial r}{\partial \beta} \cdot \frac{\partial r}{\partial \beta}.$$

As detailed in [145, 292], the squared length of a differential length element is

$$\begin{aligned} (ds)^2 &= dR \cdot dR \\ &= A^2(1 + z/R_\alpha)^2(d\alpha)^2 + B^2(1 + z/R_\beta)^2(d\beta)^2 + (dz)^2. \end{aligned}$$

Hence a differential shell element at height  $z$  has edges of length

$$\begin{aligned} ds_\alpha(z) &= A(1 + z/R_\alpha)d\alpha \\ ds_\beta(z) &= B(1 + z/R_\beta)d\beta \end{aligned} \tag{7.72}$$

and faces of area

$$\begin{aligned} dA_\alpha(z) &= A(1 + z/R_\alpha)d\alpha dz \\ dA_\beta(z) &= B(1 + z/R_\beta)d\beta dz \end{aligned}$$

as depicted in Figure 7.24.

### 7.6.2 Force and Moment Balancing

Consider force and moment resultants having the orientation depicted in Figure 7.25 and let external forces be denoted by

$$\mathbf{f} = f_\alpha \hat{\mathbf{i}}_\alpha + f_\beta \hat{\mathbf{i}}_\beta + f_n \hat{\mathbf{i}}_n.$$

The displacements in the  $\alpha, \beta$  and  $z$  directions are denoted by  $u, v$  and  $w$ .

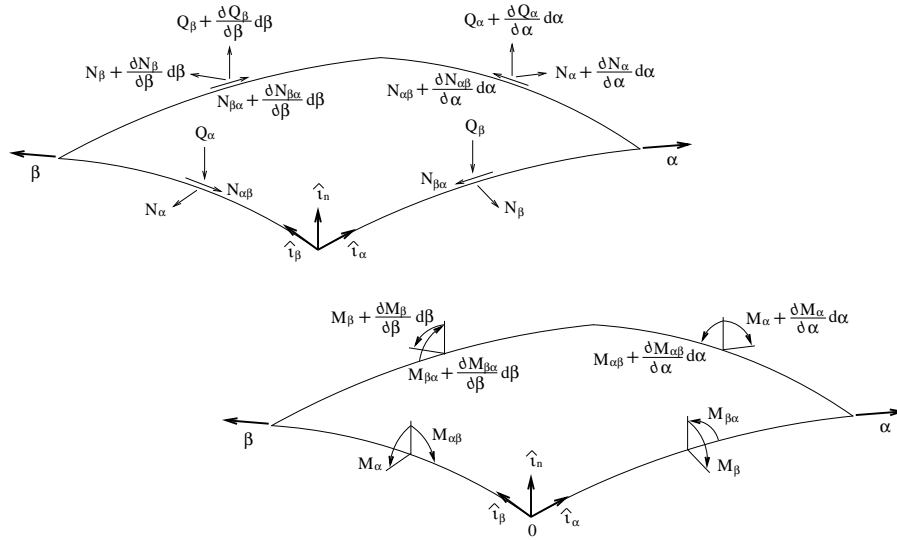


**Figure 7.25.** Force and moment resultants in shell coordinates.

Force balancing in a manner analogous to that detailed in Section 7.5.1 yields

$$\begin{aligned} \rho h AB \frac{\partial^2 u}{\partial t^2} &= \frac{\partial}{\partial \alpha} (BN_\alpha) + \frac{\partial}{\partial \beta} (AN_{\beta\alpha}) + \frac{\partial A}{\partial \beta} N_{\alpha\beta} \\ &\quad - \frac{\partial B}{\partial \alpha} N_\beta + \frac{AB}{R_\alpha} Q_\alpha + AB f_\alpha \\ \rho h AB \frac{\partial^2 v}{\partial t^2} &= \frac{\partial}{\partial \beta} (AN_\beta) + \frac{\partial}{\partial \alpha} (BN_{\alpha\beta}) + \frac{\partial B}{\partial \alpha} N_{\beta\alpha} \\ &\quad - \frac{\partial A}{\partial \beta} N_\alpha + \frac{AB}{R_\beta} Q_\beta + AB f_\beta \end{aligned} \quad (7.73)$$

$$\rho h AB \frac{\partial^2 w}{\partial t^2} = -\frac{AB}{R_\alpha} N_\alpha - \frac{AB}{R_\beta} N_\beta + \frac{\partial}{\partial \alpha} (BQ_\alpha) + \frac{\partial}{\partial \beta} (AQ_\beta) + AB f_n$$

whereas moment balancing yields

$$\begin{aligned} \frac{\partial}{\partial \alpha} (BM_\alpha) + \frac{\partial}{\partial \beta} (AM_{\beta\alpha}) + \frac{\partial A}{\partial \beta} M_{\alpha\beta} - \frac{\partial B}{\partial \alpha} M_\beta - ABQ_\alpha + AB\hat{m}_\beta &= 0 \\ \frac{\partial}{\partial \beta} (AM_\beta) + \frac{\partial}{\partial \alpha} (BM_{\alpha\beta}) + \frac{\partial B}{\partial \alpha} M_{\beta\alpha} - \frac{\partial A}{\partial \beta} M_\alpha - ABQ_\beta + AB\hat{m}_\alpha &= 0 \end{aligned} \quad (7.74)$$

$$N_{\alpha\beta} - N_{\beta\alpha} + \frac{M_{\alpha\beta}}{R_\alpha} - \frac{M_{\beta\alpha}}{R_\beta} = 0.$$

The relations (7.73) and (7.74) combine to form a strong formulation for shell models. We next specify the resultants in terms of reference surface strains and rotations.

### 7.6.3 Strain-Displacement Relations

Following the convention established in previous sections, we let  $\sigma_\alpha, \sigma_\beta$  denote normal forces and  $\sigma_{\alpha\beta} = \sigma_{\beta\alpha}, \sigma_{\alpha z}, \sigma_{\beta z}$  denote shear forces having the orientation shown in Figure 7.24. Similarly, we let  $\varepsilon_\alpha, \varepsilon_\beta, \varepsilon_z$  and  $\varepsilon_{\alpha\beta}, \varepsilon_{\alpha z}, \varepsilon_{\beta z}$  denote normal and shear strains at arbitrary points in the shell. Finally,  $e_\alpha, e_\beta, e_{\alpha\beta}$  denote normal and shear strains in the reference surface and  $\kappa_\alpha, \kappa_\beta, \kappa_{\alpha\beta}$  designate reference surface changes in curvature.

Strain-displacement relations for shells are derived from 3-D elasticity relations with various simplifications resulting from the hypotheses of Section 7.2. The simplifications typically involve when and where terms  $\frac{z}{R_\alpha}$  and  $\frac{z}{R_\beta}$  are neglected and various assumptions in this regard have led to a number of shell theories. The reader is referred to [33, 292] for a more comprehensive treatment and comparison of these theories and we focus solely on the simplified Donnell–Mushtari model and more accurate Byrne–Flügge–Lur’ye theory. The former is a subset of the latter and throughout the discussion, we underline terms in the Byrne–Flügge–Lur’ye theory that are neglected in the Donnell–Mushtari model.

It is an interesting commentary on the evolution of scientific investigations that several of the theories (e.g., Donnell–Mushtari and Byrne–Flügge–Lur’ye) advanced in parallel despite being investigated in isolation. Hence a number of the prominent theories have hyphenated designations.

We begin by posing 3-D elasticity relations in terms of shell coordinates. Letting  $U, V$  and  $W$  denote displacements in the  $\alpha, \beta$  and  $z$  directions at arbitrary points in the shell, this yields the general strain-displacement relations

$$\begin{aligned}
 \varepsilon_\alpha &= \frac{1}{1+z/R_\alpha} \left( \frac{1}{A} \frac{\partial U}{\partial \alpha} + \frac{V}{AB} \frac{\partial A}{\partial \beta} + \frac{W}{R_\alpha} \right) \\
 \varepsilon_\beta &= \frac{1}{1+z/R_\beta} \left( \frac{1}{B} \frac{\partial V}{\partial \beta} + \frac{U}{AB} \frac{\partial B}{\partial \alpha} + \frac{W}{R_\beta} \right) \\
 \varepsilon_z &= \frac{\partial W}{\partial z} \\
 \varepsilon_{\alpha\beta} &= \frac{A(1+z/R_\alpha)}{B(1+z/R_\beta)} \frac{\partial}{\partial \beta} \left[ \frac{U}{A(1+z/R_\alpha)} \right] \\
 &\quad + \frac{B(1+z/R_\beta)}{A(1+z/R_\alpha)} \frac{\partial}{\partial \alpha} \left[ \frac{V}{B(1+z/R_\beta)} \right] \\
 \varepsilon_{\alpha z} &= \frac{1}{A(1+z/R_\alpha)} \frac{\partial W}{\partial \alpha} + A(1+z/R_\alpha) \frac{\partial}{\partial z} \left[ \frac{U}{A(1+z/R_\alpha)} \right] \\
 \varepsilon_{\beta z} &= \frac{1}{B(1+z/R_\beta)} \frac{\partial W}{\partial \beta} + B(1+z/R_\beta) \frac{\partial}{\partial z} \left[ \frac{V}{B(1+z/R_\beta)} \right]
 \end{aligned} \tag{7.75}$$

— see [145, 292] for details.

To simplify these relations, we now invoke Hypothesis 4 of Section 2.2 which posits that lines originally normal to the reference surface remain straight and normal during deformation. We first employ the assumption that deformations are linear in the thickness direction to pose displacements at arbitrary points

$$\begin{aligned} U(\alpha, \beta, z) &= u(\alpha, \beta) + z\theta_\alpha(\alpha, \beta) \\ V(\alpha, \beta, z) &= v(\alpha, \beta) + z\theta_\beta(\alpha, \beta) \\ W(\alpha, \beta, z) &= w(\alpha, \beta) \end{aligned} \tag{7.76}$$

in terms of the displacements  $u, v, w$  and rotations  $\theta_\alpha, \theta_\beta$  of the reference surface — e.g., see Figure 7.26. Secondly, the assumption that fibers remain normal and unextended implies that transverse shear strains  $\varepsilon_{\alpha z}, \varepsilon_{\beta z}$  and normal strains  $\varepsilon_z$  are negligible; hence

$$\varepsilon_{\alpha z} = \varepsilon_{\beta z} = \varepsilon_z = 0. \tag{7.77}$$

The substitution of (7.76) into (7.75) and enforcement of (7.77) yields the relations

$$\theta_\alpha = \frac{u}{R_\alpha} - \frac{1}{A} \frac{\partial w}{\partial \alpha}, \quad \theta_\beta = \frac{v}{R_\beta} - \frac{1}{B} \frac{\partial w}{\partial \beta} \tag{7.78}$$

for the rotations. Note that for thick structures with significant rotation, the Kirchhoff assumption, and hence (7.77), are relaxed and strain-displacement relations are formulated in terms of  $\theta_\alpha, \theta_\beta$  as detailed for shells in [453] and plates in Section 7.8.1.

For thin structures, employment of (7.78) and (7.76) in (7.75) yields the expressions

$$\begin{aligned} \varepsilon_\alpha &= \frac{1}{(1 + z/R_\alpha)} (e_\alpha + z\kappa_\alpha) \\ \varepsilon_\beta &= \frac{1}{(1 + z/R_\beta)} (e_\beta + z\kappa_\beta) \\ \varepsilon_{\alpha\beta} &= \frac{1}{(1 + z/R_\alpha)(1 + z/R_\beta)} \left[ \left( 1 - \frac{z^2}{R_\alpha R_\beta} \right) e_{\alpha\beta} \right. \\ &\quad \left. + z \left( 1 + \frac{z}{2R_\alpha} + \frac{z}{2R_\beta} \right) \kappa_{\alpha\beta} \right]. \end{aligned} \tag{7.79}$$

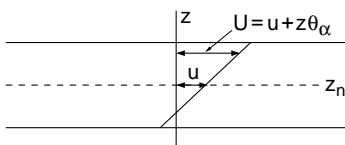


**Figure 7.26.** Formulation of the displacement  $U$  in terms of the reference surface displacement  $u$  and rotation  $\theta_\alpha$  when  $R_\alpha = \infty$ .

relating strains at an arbitrary point in the shell to reference surface strains

$$e_\alpha = \frac{1}{A} \frac{\partial u}{\partial \alpha} + \frac{v}{AB} \frac{\partial A}{\partial \beta} + \frac{w}{R_\alpha}$$

$$e_\beta = \frac{1}{B} \frac{\partial v}{\partial \beta} + \frac{u}{AB} \frac{\partial B}{\partial \alpha} + \frac{w}{R_\beta}$$

$$e_{\alpha\beta} = \frac{A}{B} \frac{\partial}{\partial \beta} \left( \frac{u}{A} \right) + \frac{B}{A} \frac{\partial}{\partial \alpha} \left( \frac{v}{B} \right)$$

and changes in curvature

$$\kappa_\alpha = \frac{1}{A} \frac{\partial \theta_\alpha}{\partial \alpha} + \frac{\theta_\beta}{AB} \frac{\partial A}{\partial \beta}$$

$$\kappa_\beta = \frac{1}{B} \frac{\partial \theta_\beta}{\partial \beta} + \frac{\theta_\alpha}{AB} \frac{\partial B}{\partial \alpha}$$

$$\kappa_{\alpha\beta} = \frac{A}{B} \frac{\partial}{\partial \beta} \left( \frac{\theta_\alpha}{A} \right) + \frac{B}{A} \frac{\partial}{\partial \alpha} \left( \frac{\theta_\beta}{B} \right) + \frac{1}{R_\alpha} \left( \frac{1}{B} \frac{\partial u}{\partial \beta} - \frac{v}{AB} \frac{\partial B}{\partial \alpha} \right)$$

$$+ \frac{1}{R_\beta} \left( \frac{1}{A} \frac{\partial v}{\partial \alpha} - \frac{u}{AB} \frac{\partial A}{\partial \beta} \right).$$

(7.80)

In combination, relations (7.78)–(7.80) quantify the strain-displacement behavior in the Byrne–Flügge–Lur’ye model whereas the underlined terms are neglected in the Donnell–Mushtari model.

### 7.6.4 Stress-Strain Behavior

The constitutive relations (7.2) and (7.4) are independent of geometry and hence are directly applicable to general shell models. When combined with (7.78)–(7.80), this quantifies the stress-strain behavior for linear and nonlinear inputs. To clarify the discussion, we will neglect the damping and external components in the subsequent general shell development. Their inclusion is straight-forward as illustrated in Section 7.5 for the rectangular plate model.

### 7.6.5 Force and Moment Resultants

Force resultants are computed by equating the total force on the face of the differential element depicted in Figure 7.24 with an equivalent resultant acting on the reference surface. To illustrate, consider the force resultant due to the normal stress  $\sigma_\alpha$ . Because the force acting on the area  $dA_\beta(z) = ds_\beta(z)dz$  of the element is  $\sigma_\alpha dA_\beta(z)$ , equating the total force with a resultant acting along the arclength  $ds_\beta = Bd\beta$  of the middle surface yields

$$N_\alpha ds_\beta = \int_{-h/2}^{h/2} \sigma_\alpha ds_\beta(z) dz.$$

From the relation (7.72) for  $ds_\beta(z)$ , it follows that

$$N_\alpha = \int_{-h/2}^{h/2} \sigma_\alpha \left(1 + \frac{z}{R_\beta}\right) dz$$

where  $N_\alpha$  has units of force per unit length of middle or reference surface.

The full set of resultants, corresponding to stresses acting on faces perpendicular to the  $\alpha$ -axis, can be expressed as

$$\begin{bmatrix} N_\alpha \\ N_{\alpha\beta} \\ Q_\alpha \end{bmatrix} = \int_{-h/2}^{h/2} \begin{bmatrix} \sigma_\alpha \\ \sigma_{\alpha\beta} \\ \sigma_{\alpha z} \end{bmatrix} \left(1 + \frac{z}{R_\beta}\right) dz .$$

Similarly, force resultants accommodating stresses perpendicular to the  $\beta$ -axis are

$$\begin{bmatrix} N_\beta \\ N_{\beta\alpha} \\ Q_\beta \end{bmatrix} = \int_{-h/2}^{h/2} \begin{bmatrix} \sigma_\beta \\ \sigma_{\beta\alpha} \\ \sigma_{\beta z} \end{bmatrix} \left(1 + \frac{z}{R_\alpha}\right) dz . \quad (7.81)$$

Moment resultants having units of moment per unit length of reference surface include the moment arm  $z$  and have the general form

$$\begin{aligned} \begin{bmatrix} M_\alpha \\ M_{\alpha\beta} \end{bmatrix} &= \int_{-h/2}^{h/2} \begin{bmatrix} \sigma_\alpha \\ \sigma_{\alpha\beta} \end{bmatrix} \left(1 + \frac{z}{R_\beta}\right) z dz \\ \begin{bmatrix} M_\beta \\ M_{\beta\alpha} \end{bmatrix} &= \int_{-h/2}^{h/2} \begin{bmatrix} \sigma_\beta \\ \sigma_{\beta\alpha} \end{bmatrix} \left(1 + \frac{z}{R_\alpha}\right) z dz. \end{aligned} \quad (7.82)$$

When evaluating the expressions, various geometric series approximations to the term  $\frac{1}{1+z/R_i}$ ,  $i = \alpha, \beta$ , in (7.79) are invoked before integration. Based on the assumption that  $\frac{z}{R_i} < 1$ , the term is neglected in the Donnell–Mushtari theory whereas terms of degree greater than three are neglected in the Byrne–Flügge–Lur’ye model. In the absence of damping or external forces or moments, the latter case yields

$$\begin{aligned} N_\alpha &= \frac{Yh}{1-\nu^2} \left[ e_\alpha + \nu e_\beta - \frac{h^2}{12} \left( \frac{1}{R_\alpha} - \frac{1}{R_\beta} \right) \left( \kappa_\alpha - \frac{e_\alpha}{R_\alpha} \right) \right] \\ N_\beta &= \frac{Yh}{1-\nu^2} \left[ e_\beta + \nu e_\alpha - \frac{h^2}{12} \left( \frac{1}{R_\beta} - \frac{1}{R_\alpha} \right) \left( \kappa_\beta - \frac{e_\beta}{R_\beta} \right) \right] \\ N_{\alpha\beta} &= \frac{Yh}{2(1+\nu)} \left[ e_{\alpha\beta} - \frac{h^2}{12} \left( \frac{1}{R_\alpha} - \frac{1}{R_\beta} \right) \left( \frac{\kappa_{\alpha\beta}}{2} - \frac{e_{\alpha\beta}}{R_\alpha} \right) \right] \\ N_{\beta\alpha} &= \frac{Yh}{2(1+\nu)} \left[ e_{\alpha\beta} - \frac{h^2}{12} \left( \frac{1}{R_\beta} - \frac{1}{R_\alpha} \right) \left( \frac{\kappa_{\alpha\beta}}{2} - \frac{e_{\alpha\beta}}{R_\beta} \right) \right] \end{aligned} \quad (7.83)$$

and

$$\begin{aligned}
 M_\alpha &= \frac{Yh^3}{12(1-\nu^2)} \left[ \kappa_\alpha + \nu\kappa_\beta - \underbrace{\left( \frac{1}{R_\alpha} - \frac{1}{R_\beta} \right) e_\alpha}_{\text{neglected}} \right] \\
 M_\beta &= \frac{Yh^3}{12(1-\nu^2)} \left[ \kappa_\beta + \nu\kappa_\alpha - \underbrace{\left( \frac{1}{R_\beta} - \frac{1}{R_\alpha} \right) e_\beta}_{\text{neglected}} \right] \\
 M_{\alpha\beta} &= \frac{Yh^3}{24(1+\nu)} \left[ \kappa_{\alpha\beta} - \underbrace{\frac{e_{\alpha\beta}}{R_\alpha}}_{\text{neglected}} \right] \\
 M_{\beta\alpha} &= \frac{Yh^3}{24(1+\nu)} \left[ \kappa_{\alpha\beta} - \underbrace{\frac{e_{\alpha\beta}}{R_\beta}}_{\text{neglected}} \right]
 \end{aligned} \tag{7.84}$$

where underlined terms are neglected in the Donnell–Mushtari model. We point out that even though the symmetry of the stress tensor dictates that  $\sigma_{\alpha\beta} = \sigma_{\beta\alpha}$ ,  $N_{\alpha\beta} \neq N_{\beta\alpha}$  and  $M_{\alpha\beta} \neq M_{\beta\alpha}$  unless  $R_\alpha = R_\beta$  or higher-order terms are neglected.

### 7.6.6 Boundary Conditions

Boundary conditions can be specified using either Newtonian (force and moment balancing) principles analogous to those employed for rods in Section 7.3 or energy (work) relations similar to (7.64). As detailed on page 27 of [292], appropriate boundary conditions along edges  $\alpha_1$  and  $\alpha_2$  are

$$\begin{aligned}
 u &= 0 \quad \text{or} \quad N_\alpha = 0 \\
 v &= 0 \quad \text{or} \quad N_{\alpha\beta} + \frac{M_{\alpha\beta}}{R_\beta} = 0 \\
 w &= 0 \quad \text{or} \quad Q_\alpha + \frac{1}{B} \frac{\partial M_{\alpha\beta}}{\partial \beta} = 0 \\
 \theta_\alpha &= 0 \quad \text{or} \quad M_\alpha = 0
 \end{aligned} \tag{7.85}$$

and  $M_{\alpha\beta}w|_{\beta_1}^{\beta_2} = 0$ . Note that if  $\beta$  is a closed curve (as will be the case with a cylindrical shell), then this last condition is satisfied identically. Analogous conditions along  $\beta_1$  and  $\beta_2$  edges are obtained by reversing the roles of  $\alpha$  and  $\beta$  in (7.85).

## 7.7 Shell Models – Special Cases

The relations (7.73), with stress-strain behavior quantified by (7.2) or (7.4), resultants given by (7.83) and (7.84), and strain-displacement relations (7.79), provide a strong model formulation for general shell geometries. As noted in the introduction to the chapter, these relations are very general and include rod, beam and plate models as subsets. In this section, we illustrate the manner through which specific choices of the radii  $R_\alpha, R_\beta$  and Lamé parameters  $A, B$  yield plate, cylindrical

shell, and curved beam models. For clarity, we consider the low-order Donnell–Mushtari relations but note that similar analysis applies with the more accurate Byrne–Flügge–Lur’ye model.

### 7.7.1 Plate Model

To obtain a rectangular plate model, we take

$$\begin{aligned}\alpha &= x & \beta &= y \\ A &= 1 & B &= 1 \\ R_\alpha &= \infty & R_\beta &= \infty\end{aligned}\tag{7.86}$$

in the relations of Section 7.6. It is observed that (7.73) and (7.74), obtained through force and moment balancing, reduce to (7.46), (7.47) and (7.50)–(7.52) whereas the resultant expressions (7.83) and (7.84) reduce to the elastic plate components of (7.58). In a similar manner, the strain-displacement relations for the two geometries are made equivalent by the parameter choices (7.86). Hence the plate is simply a thin shell with no curvature in the undeformed state.

### 7.7.2 Cylindrical Shell Model — AFM Stage

As illustrated in Figure 7.1, cylindrical shells arise in smart material applications ranging from nanopositioning in an atomic force microscope (AFM) to control of structure-borne noise in structural acoustic cavities. For clarity, we illustrate the development of a cylindrical shell model in the context of the piezoceramic AFM stage depicted in Figure 7.1(a). The extension of the theory to composite shells with surface-mounted patches is analogous to that provided in Section 7.5 for plates.

We focus on characterizing the component of the actuator employed for transverse or axial placement of the sample relative to the microcantilever. For modeling purposes, we consider a shell of radius  $R$ , length  $\ell$ , and thickness  $h$  with clamped boundary conditions at one end and dissipating elastic conditions at the other end. Because the shell is solely comprised of PZT, we omit subscripts on the material properties. For simplicity, we summarize the Donnell–Mushtari model but note that the Byrne–Flügge–Lur’ye relations are derived in an analogous manner.

We consider the axial direction to be along the  $x$ -axis and employ the parameters

$$\begin{aligned}\alpha &= x & \beta &= \theta \\ A &= 1 & B &= R \\ R_\alpha &= \infty & R_\beta &= R\end{aligned}$$

in the general shell relations summarized in Section 7.6.

**Strong Model Formulation**

Combination of the relations (7.73) and (7.74) with these parameter choices yields the dynamic model

$$\begin{aligned}
 R\rho h \frac{\partial^2 u}{\partial t^2} - R \frac{\partial N_x}{\partial x} - \frac{\partial N_{x\theta}}{\partial \theta} &= Rf_x \\
 R\rho h \frac{\partial^2 v}{\partial t^2} - \frac{\partial N_\theta}{\partial \theta} - R \frac{\partial N_{x\theta}}{\partial x} &= Rf_\theta \\
 R\rho h \frac{\partial^2 w}{\partial t^2} - R \frac{\partial^2 M_x}{\partial x^2} - \frac{1}{R} \frac{\partial^2 M_\theta}{\partial \theta^2} - 2 \frac{M_{x\theta}}{\partial x \partial \theta} + N_\theta &= Rf_n.
 \end{aligned}
 \tag{7.87}$$

The force and moment resultants

$$\begin{aligned}
 N_x &= \frac{Yh}{1-\nu^2}(e_x + \nu e_\theta) + \frac{ch}{1-\nu^2}(\dot{e}_x + \nu \dot{e}_\theta) - \frac{h}{1-\nu}[a_1(P - P_R) + a_2(P - P_R)^2] \\
 N_\theta &= \frac{Yh}{1-\nu^2}(e_\theta + \nu e_x) + \frac{ch}{1-\nu^2}(\dot{e}_\theta + \nu \dot{e}_x) - \frac{h}{1-\nu}[a_1(P - P_R) + a_2(P - P_R)^2] \\
 N_{x\theta} &= \frac{Yh}{2(1+\nu)}e_{x\theta} + \frac{ch}{2(1+\nu)}\dot{e}_{x\theta}
 \end{aligned}
 \tag{7.88}$$

and

$$\begin{aligned}
 M_x &= \frac{Yh^3}{12(1-\nu^2)}(\kappa_x + \nu \kappa_\theta) + \frac{ch^3}{12(1-\nu^2)}(\dot{\kappa}_x + \nu \dot{\kappa}_\theta) \\
 M_\theta &= \frac{Yh^3}{12(1-\nu^2)}(\kappa_\theta + \nu \kappa_x) + \frac{ch^3}{12(1-\nu^2)}(\dot{\kappa}_\theta + \nu \dot{\kappa}_x) \\
 M_{x\theta} &= \frac{Yh^3}{24(1+\nu)}\kappa_{x\theta} + \frac{ch^3}{24(1+\nu)}\dot{\kappa}_{x\theta}
 \end{aligned}
 \tag{7.89}$$

include elastic, damping and external components analogous to (7.58)–(7.63) for the plate. Note that we have employed the nonlinear input relations (7.4) when quantifying the external component since the characterization of hysteresis and constitutive nonlinearities can prove crucial when specifying nanoscale displacements. It is observed that in the Donnell–Mushtari theory, poling in a  $d_{31}$  manner to produce transverse or axial motion yields null moments since the terms  $\frac{z}{R}$  are considered negligible compared with unity. For low drive regimes where the behavior is approximately linear, one can alternatively employ the linear input relation (7.2). Finally, the midsurface strains and changes in curvature are

$$\begin{aligned}
 e_x &= \frac{\partial u}{\partial x} \quad , \quad e_\theta = \frac{1}{R} \frac{\partial v}{\partial \theta} + \frac{w}{R} \quad , \quad e_{x\theta} = \frac{\partial v}{\partial x} + \frac{1}{R} \frac{\partial u}{\partial \theta} \\
 \kappa_x &= -\frac{\partial^2 w}{\partial x^2} \quad , \quad \kappa_\theta = -\frac{1}{R^2} \frac{\partial^2 w}{\partial \theta^2} \quad , \quad \kappa_{x\theta} = -\frac{2}{R} \frac{\partial^2 w}{\partial x \partial \theta}.
 \end{aligned}
 \tag{7.90}$$

A comparison between (7.87)–(7.90) and the corresponding plate relations reveals that a number of the terms are equivalent if one equates  $dy$  and  $Rd\theta$ . However, the presence of the term  $\frac{w}{R}$  in the strain relation for  $e_\theta$  produces a curvature-induced coupling between displacements not found in models for flat structures. This impacts both the dynamics quantified by the model and associated approximate techniques for model simulation. It is also noted that if one equates the differentials  $dy$  and  $Rd\theta$  and takes  $R \rightarrow \infty$ , the Donnell–Mushtari shell model reduces to the plate model.

The boundary conditions for the fixed-end at  $x = 0$  are taken to be

$$u = v = w = \frac{\partial w}{\partial x} = 0$$

whereas the conditions

$$\begin{aligned} N_x = -m \frac{\partial^2 u}{\partial t^2} \quad , \quad N_{x\theta} + \frac{M_{x\theta}}{R} = 0 \\ Q_x + \frac{1}{R} \frac{\partial M_{x\theta}}{\partial \theta} = 0 \quad , \quad M_x = 0 \end{aligned}$$

are employed at  $x = \ell$ . The first resultant condition incorporates the inertial force due to the mass  $m$  of the piezoceramic actuator employed for lateral translation along with the mass of the sample.

### Weak Model Formulation

To reduce smoothness requirements for approximation and eliminate the Dirac behavior of external inputs at  $x = \ell$ , we also consider a weak formulation of the model. The state is taken to be  $\xi(t) = (u(t, \cdot, \cdot), v(t, \cdot, \cdot), w(t, \cdot, \cdot), u(t, \ell, \cdot))$  in the state space

$$X = L^2(\Omega) \times L^2(\Omega) \times L^2(\Omega) \times L^2(0, 2\pi)$$

where

$$\Omega = [0, \ell] \times [0, 2\pi]$$

denotes the shell region. The space of test functions is specified as

$$V = \{ \Phi = (\phi_1, \phi_2, \phi_3, \eta) \in X \mid \phi_1 \in H_0^1(\Omega), \phi_2 \in H_0^1(\Omega), \phi_3 \in H_0^2(\Omega) \}$$

where  $\eta(\theta) = \phi_1(\ell, \theta)$  and

$$\begin{aligned} H_0^1(\Omega) &= \{ \phi \in H^1(\Omega) \mid \phi(0, \theta) = 0 \} \\ H_0^2(\Omega) &= \{ \phi \in H^2(\Omega) \mid \phi(0, \theta) = \phi'(0, \theta) = 0 \}. \end{aligned} \tag{7.91}$$

Through either variation principles analogous to those in Section 7.3.2 — e.g., see [33] — or integration by parts, one obtains the weak formulation of the

thin shell model,

$$\begin{aligned}
 \int_{\Omega} \left\{ R\rho h \frac{\partial^2 u}{\partial t^2} \phi_1 + RN_x \frac{\partial \phi_1}{\partial x} + N_{x\theta} \frac{\partial \phi_1}{\partial \theta} - Rf_x \phi_1 \right\} d\omega &= 0 \\
 \int_{\Omega} \left\{ R\rho h \frac{\partial^2 v}{\partial t^2} \phi_2 + N_{\theta} \frac{\partial \phi_2}{\partial \theta} + RN_{x\theta} \frac{\partial \phi_2}{\partial x} - Rf_{\theta} \phi_2 \right\} d\omega &= 0 \\
 \int_{\Omega} \left\{ R\rho h \frac{\partial^2 w}{\partial t^2} \phi_3 - RM_x \frac{\partial^2 \phi_3}{\partial x^2} - 2M_{x\theta} \frac{\partial^2 \phi_3}{\partial x \partial \theta} - \frac{1}{R} M_{\theta} \frac{\partial^2 \phi_3}{\partial \theta^2} \right. \\
 \left. + N_{\theta} \phi_3 - Rf_n \phi_3 \right\} d\omega &= 0,
 \end{aligned} \tag{7.92}$$

which must be satisfied for all  $\Phi \in V$ . The resultants are given by (7.88) and (7.89) with midsurface strains and changes in curvature designated in (7.90). Numerical methods for approximating solutions to (7.92) are discussed in Section 8.5.

### 7.7.3 Curved Beam Model

The narrow THUNDER transducer shown in Figure 7.4(c) is curved in the region covered by PZT and hence exhibits curvature-induced coupling between in-plane and out-of-plane motion. Moreover, it is sufficiently narrow that motion in the width (longitudinal) direction is negligible. Hence it behaves as a thin beam with coupled circumferential and transverse dynamics.

Thin beam models for such curved geometries can be obtained directly from previous shell models. As detailed in [491], the geometry in the patch region has been experimentally verified to have nearly constant radius of curvature in  $\theta$  with negligible curvature in  $x$ , as predicted by thermomechanical theory, so we start with the Donnell–Mushtari cylindrical shell model summarized in Section 7.7.2. More accurate Byrne–Flügge–Lur’ye relations can be constructed by retaining higher-order terms in the manner indicated in previous sections.

We initially consider a homogeneous thin beam having width  $b$ , thickness  $h$ , and constant radius of curvature  $R$  as depicted in Figure 7.27. The circumferential and transverse displacements are denoted by  $v$  and  $w$ .

From (7.87), it follows that a strong formulation of the curved beam model for this geometry is

$$\begin{aligned}
 R\rho h \frac{\partial^2 v}{\partial t^2} - \frac{\partial N_{\theta}}{\partial \theta} &= Rf_{\theta} \\
 R\rho h \frac{\partial^2 w}{\partial t^2} - \frac{1}{R} \frac{\partial^2 M_{\theta}}{\partial \theta^2} + N_{\theta} &= Rf_n
 \end{aligned} \tag{7.93}$$

where the resultants are defined in (7.88) and (7.89). To illustrate the manner through which curvature-induced coupling between  $v$  and  $w$  components is introduced, consider the undamped case ( $c = 0$ ) in the absence of voltage or field inputs.

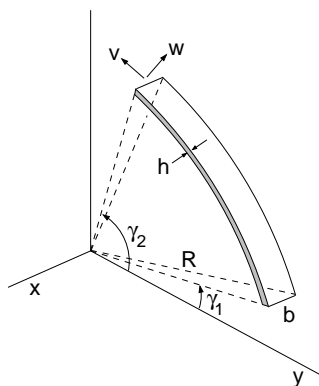


**Figure 7.27.** Curved beam in which circumferential and transverse motion are coupled due to curvature.

In this case, the resultants are

$$N_\theta = Yh \left( \frac{1}{R} \frac{\partial v}{\partial \theta} + \frac{w}{R} \right)$$

$$M_\theta = -\frac{Yh^3}{12R^2} \frac{\partial^2 w}{\partial \theta^2}.$$

Hence  $w$ -dependence is introduced in the equation of motion for  $v$  through the term  $\frac{w}{R}$  whereas  $v$ -dependence in the second relation of (7.93) is introduced through the strain  $\frac{\partial v}{\partial \theta}$ .

To construct a corresponding variational or weak formulation, we consider states  $\xi(t) = (v(t, \cdot), w(t, \cdot))$  in the state space

$$X = L^2(\Omega) \times L^2(\Omega)$$

where  $\Omega = [\gamma_1, \gamma_2]$ . The space of test functions is

$$V = H_b^2(\Omega) \times H_b^2(\Omega)$$

where the subscript  $b$  indicates subsets of the spaces  $H^1(\Omega)$  and  $H^2(\Omega)$  comprised of functions that satisfy essential boundary conditions. A weak formulation is then

$$\int_{\gamma_1}^{\gamma_2} \left\{ R\rho h \frac{\partial^2 v}{\partial t^2} \phi_1 + N_\theta \frac{d\phi_1}{d\theta} - Rf_\theta \phi_1 \right\} d\omega = 0$$

$$\int_{\gamma_1}^{\gamma_2} \left\{ R\rho h \frac{\partial^2 w}{\partial t^2} \phi_2 + N_\theta \phi_2 - \frac{1}{R} M_\theta \frac{d^2 \phi_2}{d\theta^2} - Rf_n \phi_2 \right\} = 0$$

which must be satisfied for all  $(\phi_1, \phi_2) \in V$ .

### 7.7.4 Flat Beam Model

The uncoupled rod equations quantifying in-plane motion and flat beam equations characterizing out-of-plane motion were derived in Sections 7.3 and 7.4. They also follow directly from the general shell models with  $\beta = y$ ,  $B = 1$  and  $R_\beta = \infty$  which implies that differentials  $Rd\theta$  in the curved beam model are replaced by  $dy$  and  $R \rightarrow \infty$  to yield the *uncoupled* relations

$$\rho h \frac{\partial^2 v}{\partial t^2} - \frac{\partial N_y}{\partial y} = f_y$$

$$\rho h \frac{\partial^2 w}{\partial t^2} - \frac{\partial^2 M_y}{\partial y^2} = f_n.$$

In the absence of damping or inputs, the resultants are

$$N_y = Yh \frac{\partial v}{\partial y}, \quad M_y = -\frac{Yh^3}{12} \frac{\partial^2 w}{\partial y^2}$$

which are also uncoupled. The in-plane relation is exactly the undamped rod model (7.14) whereas the transverse expression is the undamped beam model (7.38). The inclusion of damping and input components yields the complete rod and beam models developed in Sections 7.3 and 7.4.

## 7.8 Timoshenko, Mindlin–Reissner, and von Kármán Models

The rod, beam, plate and shell models, developed in previous sections, are based on Assumptions 1–4 of Section 7.2. In this section, we relax various assumptions to obtain the linear Mindlin–Reissner and Timoshenko models, which incorporate shear deformations and rotational effects, and the nonlinear von Kármán relations.

### 7.8.1 Mindlin–Reissner Plate and Timoshenko Beam Models

The fourth hypothesis of Section 7.2 asserts that normal lines to the reference surface remain normal during bending. As illustrated in Figure 7.28, this is reasonable for thin structures with moderate rotational effects but fails in thick structures with significant rotation due to nonnegligible transverse shear deformations.<sup>33</sup> The Mindlin–Reissner and Timoshenko models result when Assumption 4 is relaxed to allow transverse shear strains while retaining the assumption that filaments remain straight and unstrained during deformation.

#### Mindlin–Reissner Plate Model

For simplicity, we consider a homogeneous plate of thickness  $h$  in the absence of damping ( $c = 0$ ) and inputs ( $V = E = 0$ ). The extensions to include these effects are analogous to those detailed in Sections 7.5.1.

<sup>33</sup>This is easily illustrated by noting how a thick paperback book bends as compared with bending of a thin book.

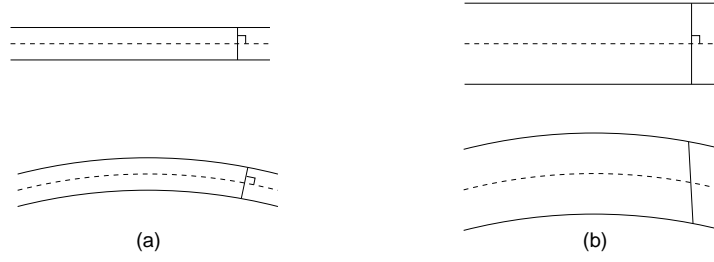


**Figure 7.28.** Behavior of normal lines to the reference surface during bending. (a) Lines remain normal in thin structures with moderate rotation and (b) non-normal response in thick structures due to transverse shear strains.

To formulate the model, we take  $\alpha = x, A = 1, R_\alpha = \infty, \beta = y, B = 1$  and  $R_\beta = \infty$  in the general shell relations (7.75)–(7.80) to obtain the strain-displacement relations

$$\begin{aligned} \varepsilon_x &= e_x + z\kappa_x \quad , \quad \varepsilon_y = e_y + z\kappa_y \\ \varepsilon_{xy} &= e_{xy} + z\kappa_{xy} \quad , \quad \varepsilon_{xz} = \frac{\partial w}{\partial x} + \theta_x \quad , \quad \varepsilon_{yz} = \frac{\partial w}{\partial y} + \theta_y \end{aligned} \tag{7.94}$$

where  $\theta_x, \theta_y$  are rotations of the reference surface and

$$\begin{aligned} e_x &= \frac{\partial u}{\partial x} \quad , \quad e_y = \frac{\partial v}{\partial y} \quad , \quad e_{xy} = \frac{\partial u}{\partial y} + \frac{\partial v}{\partial x} \\ \kappa_x &= \frac{\partial \theta_x}{\partial x} \quad , \quad \kappa_y = \frac{\partial \theta_y}{\partial y} \quad , \quad \kappa_{xy} = \frac{\partial \theta_x}{\partial y} + \frac{\partial \theta_y}{\partial x} . \end{aligned} \tag{7.95}$$

Note that if Kirchhoff’s hypothesis is invoked so that  $\varepsilon_{xz} = \varepsilon_{yz} = 0$  in (7.94), then the kinematic relations (7.95) are the same as the thin plate relations (7.56). However, retention of these terms eliminates one of the contradictions arising from the assumption of all four postulates [292].

The force and moment resultants

$$\begin{aligned} N_x &= \frac{Yh}{1-\nu^2} \left( \frac{\partial u}{\partial x} + \nu \frac{\partial v}{\partial y} \right) \quad , \quad M_x = \frac{Yh^3}{12(1-\nu^2)} \left( \frac{\partial \theta_x}{\partial x} + \nu \frac{\partial \theta_y}{\partial y} \right) \\ N_y &= \frac{Yh}{1-\nu^2} \left( \frac{\partial v}{\partial y} + \nu \frac{\partial u}{\partial x} \right) \quad , \quad M_y = \frac{Yh^3}{12(1-\nu^2)} \left( \frac{\partial \theta_y}{\partial y} + \nu \frac{\partial \theta_x}{\partial x} \right) \\ N_{xy} &= \frac{Yh}{2(1+\nu)} \left( \frac{\partial u}{\partial y} + \frac{\partial v}{\partial x} \right) \quad , \quad M_{xy} = \frac{Yh^3}{24(1+\nu)} \left( \frac{\partial \theta_y}{\partial x} + \frac{\partial \theta_x}{\partial y} \right) \end{aligned} \tag{7.96}$$

follow from (7.83) and (7.84) whereas the shear resultants

$$Q_x = \frac{K^2 Yh}{2(1+\nu)} \left( \frac{\partial w}{\partial x} + \theta_x \right) \quad , \quad Q_y = \frac{K^2 Yh}{2(1+\nu)} \left( \frac{\partial w}{\partial y} + \theta_y \right)$$

are provided by (7.81) and (7.82). The constant  $K^2$  compensates for the fact that the outer surface of the plate cannot support a shear stress. Whereas averaging values can be used to compute theoretical values for  $K^2$ , in applications it is typically treated as a parameter to be estimated.

Force balancing in the manner detailed in Section 7.5.1 yields the dynamic equations

$$\begin{aligned} \rho h \frac{\partial^2 u}{\partial t^2} - \frac{\partial N_x}{\partial x} - \frac{\partial N_{yx}}{\partial y} &= f_x \\ \rho h \frac{\partial^2 v}{\partial t^2} - \frac{\partial N_y}{\partial y} - \frac{\partial N_{xy}}{\partial x} &= f_y \\ \rho h \frac{\partial^2 w}{\partial t^2} - \frac{\partial Q_x}{\partial x} - \frac{\partial Q_y}{\partial y} &= f_n \end{aligned}$$

while inclusion of rotational inertia when balancing moments yields

$$\begin{aligned} \frac{\rho h^3}{12} \frac{\partial^2 \theta_x}{\partial t^2} &= \frac{\partial M_x}{\partial x} + \frac{\partial M_{xy}}{\partial y} - Q_x \\ \frac{\rho h^3}{12} \frac{\partial^2 \theta_y}{\partial t^2} &= \frac{\partial M_y}{\partial y} + \frac{\partial M_{xy}}{\partial x} - Q_y. \end{aligned} \tag{7.97}$$

It is observed that the relaxation of the Kirchhoff hypothesis and inclusion of rotational inertia affects only the transverse relation. It is detailed in [291, 453] that inclusion of shear deformations decreases the stiffness whereas the rotational inertia increases mass effects. Both serve to decrease modeled frequencies and in a number of applications, including those with multiple frequencies, the Reissner–Mindlin plate model provides better accuracy than the Kirchhoff plate model developed in Section 7.5.

### Timoshenko Beam Model

The 1-D analogue of the Mindlin–Reissner plate model is the Timoshenko beam model. Since it follows directly from (7.94)–(7.97) when one considers transverse displacements in addition to longitudinal displacements in either  $x$  or  $y$ , we do not repeat the relations. The advantages that the Timoshenko model provide over the Euler–Bernoulli model developed in Section 7.4 are the same as those provided by the Mindlin–Reissner plate model.

### 7.8.2 von Kármán Plate Model

As a result of Assumption 2 of Section 7.2, kinematic and equilibrium relations for the rod, beam, plate and shell models developed in previous sections, were considered with respect to the *unperturbed* reference surface. Furthermore, high-order strain-displacement terms were neglected in accordance with the assumption of small displacements. The results of Assumption 2 are twofold: (i) the models exhibit *linear* state-dependence, and (ii) the modeling relations for in-plane and out-of-plane motion are *decoupled* for flat structures ( $R_\alpha = R_\beta = \infty$ ).

In this section, we relax this assumption to accommodate large displacements of the type often exhibited by THUNDER transducers and MEMs of the type depicted in Figure 7.4. This yields the nonlinear von Kármán plate model in which longitudinal and transverse displacements are coupled.

To clarify the discussion, we again consider a homogeneous plate of thickness  $h$  for which damping and external voltages or fields are neglected; hence the reference surface coincides with the middle surface so  $z_n = 0$  and moments contain only elastic components. Extension of the model to incorporate damping, linear and nonlinear inputs, and geometric nonhomogeneities follow in the manner detailed in Section 7.5.1.

The first extension to accommodate displacements that are large compared with the thickness is to balance forces and moments with regard to the *deformed* reference surface depicted in Figure 7.29. When defining the deformation, it is typical to approximate the sine of rotation angles by changes in the slope.

**Force and Moment Balancing**

As detailed in [291, 480], balancing of transverse forces yields the nonlinear relations

$$\begin{aligned} \rho h \frac{\partial^2 w}{\partial t^2} &= \frac{\partial Q_x}{\partial x} + \frac{\partial Q_y}{\partial y} + \frac{\partial}{\partial x} \left( N_x \frac{\partial w}{\partial x} \right) + \frac{\partial}{\partial y} \left( N_y \frac{\partial w}{\partial y} \right) \\ &+ \frac{\partial}{\partial x} \left( N_{xy} \frac{\partial w}{\partial y} \right) + \frac{\partial}{\partial y} \left( N_{xy} \frac{\partial w}{\partial x} \right) + f_n \end{aligned}$$

when third-order differential terms are neglected. Similarly, balancing forces in the

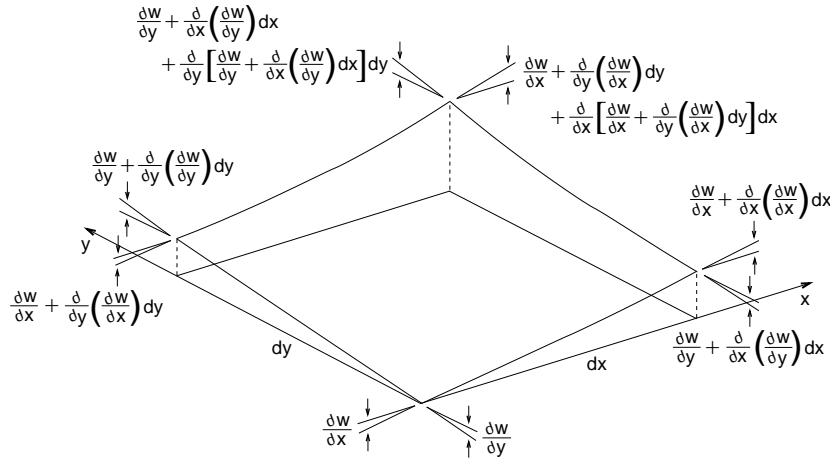


**Figure 7.29.** Deformed reference surface for a thin plate.

$x$  and  $y$  directions yields the in-plane relations

$$\rho h \frac{\partial^2 u}{\partial t^2} = \frac{\partial N_x}{\partial x} + \frac{\partial N_{xy}}{\partial y} - \frac{\partial}{\partial x} \left( Q_x \frac{\partial w}{\partial x} \right) - \frac{\partial}{\partial y} \left( Q_y \frac{\partial w}{\partial x} \right) + f_x$$

$$\rho h \frac{\partial^2 v}{\partial t^2} = \frac{\partial N_y}{\partial y} + \frac{\partial N_{xy}}{\partial x} - \frac{\partial}{\partial y} \left( Q_y \frac{\partial w}{\partial y} \right) - \frac{\partial}{\partial x} \left( Q_x \frac{\partial w}{\partial y} \right) + f_y.$$

It is observed that these nonlinear equations reduce to the linear model (7.46) and (7.47) if high-order terms are neglected.

The incorporation of rotational inertia but neglect of high-order terms yields

$$\frac{\rho h^3}{12} \frac{\partial^3 w}{\partial x \partial t^2} = Q_x - \frac{\partial M_x}{\partial x} - \frac{\partial M_{yx}}{\partial y} \tag{7.98}$$

$$\frac{\rho h^3}{12} \frac{\partial^3 w}{\partial y \partial t^2} = Q_y - \frac{\partial M_y}{\partial y} - \frac{\partial M_{xy}}{\partial x}$$

when moments are balanced. These are a simplification of the Mindlin–Reissner relations (7.97) based on the assumption that  $\varepsilon_{xz} = \varepsilon_{yz} = 0$ , and hence  $\theta_x = -\frac{\partial w}{\partial x}$ ,  $\theta_y = -\frac{\partial w}{\partial y}$ , in accordance with Assumption 2 of Section 7.2. It is observed that (7.98) reduces to (7.50) and (7.51) if rotational inertia is neglected.

### Force and Moment Resultants

To accommodate large displacements, quadratic terms are retained in the strain-displacement relations

$$\varepsilon_x = \frac{\partial u}{\partial x} + \frac{1}{2} \left( \frac{\partial w}{\partial x} \right)^2, \quad \varepsilon_y = \frac{\partial v}{\partial y} + \frac{1}{2} \left( \frac{\partial w}{\partial y} \right)^2, \quad \varepsilon_{xy} = \frac{\partial v}{\partial x} + \frac{\partial u}{\partial y} + \frac{\partial w}{\partial x} \frac{\partial w}{\partial y}$$

which yields the force resultants

$$N_x = \frac{Eh}{1-\nu^2} \left[ \frac{\partial u}{\partial x} + \nu \frac{\partial v}{\partial y} + \frac{1}{2} \left( \frac{\partial w}{\partial x} \right)^2 + \frac{\nu}{2} \left( \frac{\partial w}{\partial y} \right)^2 \right]$$

$$N_y = \frac{Eh}{1-\nu^2} \left[ \frac{\partial v}{\partial y} + \nu \frac{\partial u}{\partial x} + \frac{1}{2} \left( \frac{\partial w}{\partial y} \right)^2 + \frac{\nu}{2} \left( \frac{\partial w}{\partial x} \right)^2 \right]$$

$$N_{xy} = \frac{Eh}{2(1+\nu)} \left[ \frac{\partial u}{\partial y} + \frac{\partial v}{\partial x} + \frac{\partial w}{\partial x} \frac{\partial w}{\partial y} \right].$$

The moment resultants remain the same as those defined in linear theory — e.g., see (7.57) and (7.58) or (7.96) with  $\theta_x = -\frac{\partial w}{\partial x}$ ,  $\theta_y = -\frac{\partial w}{\partial y}$ .

We note that in this nonlinear von Kármán model, the longitudinal and transverse displacements are coupled due to the curvature of the deformed reference surface and the retention of high-order terms in the kinematic relations. As expected,

the model reduces to the linear Kirchhoff model developed in Section 7.5 under the assumption of small displacements.

The reader is directed to [291] for further discussion regarding properties of the von Kármán model and to [277] for a derivation of the model using energy principles.

## 7.9 THUNDER Models

To illustrate principles developed throughout this chapter, we discuss issues pertaining to characterization of initial shapes and displacements generated by THUNDER transducers. We note that this is an active research topic and the model discussed here should be interpreted as initial formulations to illustrate issues rather than final frameworks which fully characterize the complex behavior of the devices. Limitations and open research questions will be indicated at various points in the discussion.

We consider a narrow THUNDER device of the type illustrated in Figure 7.4 and 7.30(a) which exhibits negligible curvature and motion in the width direction. One end is clamped while the other is constrained to slide freely in the horizontal direction as depicted in Figure 7.30(d). For specificity, we consider a physical transducer comprised of a stainless steel backing strip, an adhesive Layer of LaRC Si, a PZT layer, and a protective top coating of LaRC Si. The steel has dimensions 0.5 in  $\times$  2.5 in  $\times$  0.015 in and the centered PZT is 0.5 in  $\times$  1.5 in  $\times$  0.008 in. The mean thickness of the LaRC Si is 0.001 in. We include the specific constituent materials and dimensions to indicate a prototypical size but note that the modeling principles are generic and hence apply to a range of compounds and dimensions.

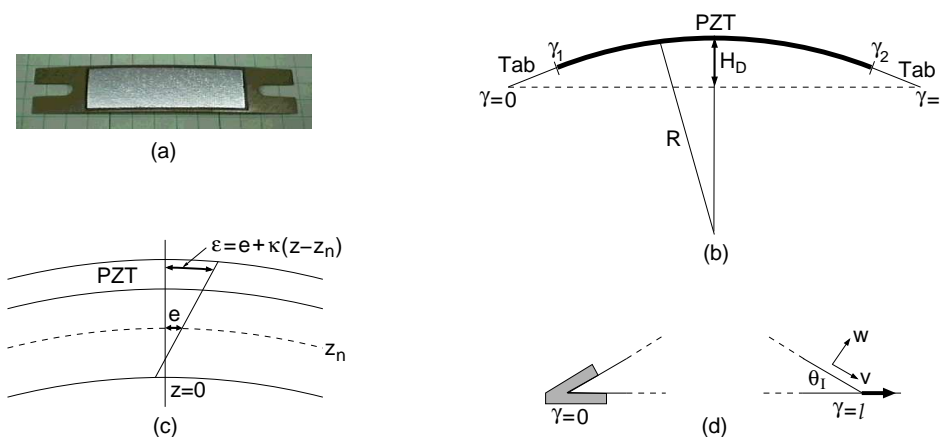


**Figure 7.30.** (a) Narrow THUNDER transducer and (b) geometry comprised of flat tabs and a circular arc having radius of curvature  $R$  in the region  $[\gamma_1, \gamma_2]$  covered by PZT. (c) Reference surface and decomposition of strains  $\epsilon$  into an in-plane component  $e$  and a bending component  $\kappa(z - z_n)$ . (d) Fixed-end condition at  $\gamma = 0$  and sliding end at  $\gamma = l$ .

The geometry employed for model development is established in Figure 7.29(b) and (c). The coordinate for arclength is denoted by  $\gamma$  where  $\gamma = x$  in the flat tabs and  $\gamma = R\theta$  in the curved region covered by PZT. The ends of the PZT are delineated by  $\gamma_1$  and  $\gamma_2$ , and the entire transducer has length  $\ell$  and width  $b$ . Material properties and dimensions of the backing layer, LaRC Si adhesive, and PZT are respectively indicated by the subscripts  $I$ ,  $S$  and  $A$ . We orient the thickness coordinate so that  $z = 0$  corresponds to the outer edge of the backing material.

There are two related but distinct phases of model development. In the first, thermal, elastic and electromechanical forces are balanced to quantify the shape of the device as a function of constituent materials and manufacturing conditions. This is important both for device characterization and the inverse problem of constructing transducers having prescribed geometries and attributes. Secondly, curved and flat beam relations are coupled to construct dynamic models which quantify in-plane and out-of-plane displacements due to input fields.

To simplify the discussion, we focus primarily on models having linear state dependence and linear or nonlinear inputs. However, we caution the reader that the linear theory has limited applicability for large displacements and high drive regimes. Furthermore, the nonlinear input relations rely on the assumption that stresses do not exceed the critical stress  $\sigma_c$  which delineates the initiation of stress-induced switching. These relations must also be extended to incorporate the stress-dependent electromechanical behavior shown in Figure 1.6(c).

## 7.9.1 Linear State Dependence

### Actuator Geometry

During the manufacturing process, the constituent materials are heated in a vacuum to approximately 325 °C under a pressure of 241.3 kPa. During the cooling process, the LaRC Si solidifies at approximately 270 °C and subsequent cooling produces curvature in the composite structure due to the differing thermal coefficients of the constituent materials. Because the Curie point of PZT5A (350 °C) is in the proximity of the peak manufacturing temperature, the device is subsequently reoled after cooling. This increases the radius of curvature  $R$  and hence decreases the dome height  $H_D$  of the physical device.

To consolidate notation, we let the indices  $i = 1, \dots, 4$  respectively correspond to the ordered subscripts  $I, S, A, S$  indicating the constituent materials as shown in Figure 7.31. The thermal coefficients are generically denoted by  $\alpha$ , and  $e$  and  $\kappa$  respectively denote the reference surface strain and change in curvature. Finally, we define

$$H_i = \sum_{j=1}^i h_j \quad (7.99)$$

to indicate the  $z$  values that delineate the various layers — i.e.,  $H_0 = 0$ ,  $H_1 = h_I$ ,  $H_2 = h_I + h_S$ ,  $H_3 = h_I + h_S + H_A$  and  $H_4 = h_I + h_S + H_A + H_S$ .

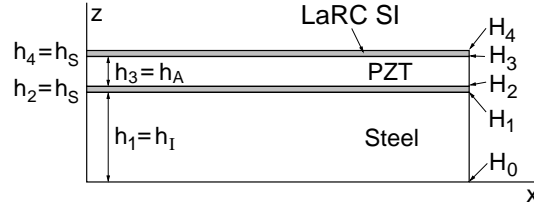


**Figure 7.31.** Orientation employed when quantifying the transducer geometry.

Under the assumption that strains are proportion to  $\Delta T$  during cooling, the strain  $\varepsilon(z)$  at a height  $z$  in the composite can be expressed as

$$\varepsilon(z) = \frac{\sigma(z)}{Y(z)} + \alpha(z)\Delta T - \frac{3}{2}\nu\lambda_s\delta(z) \quad (7.100)$$

where  $Y(z) = Y_i$  and  $\alpha(z) = \alpha_i$  for  $z$  in the  $i$ th layer,  $\nu$  is the Poisson ratio and  $\lambda_s$  is the saturation electrostriction. The third term on the right hand side quantifies strains due to dipole rotation during repoling using analysis similar to that employed for magnetostrictive materials in Section 4.1.8. The Kronecker delta

$$\delta = \begin{cases} 1, & \text{if } z \text{ in PZT layer} \\ 0, & \text{otherwise} \end{cases}$$

isolates the electromechanical strains due to repoling to the PZT layer.

Additionally, the assumption that strains are linear through the thickness yields the relation

$$\varepsilon(z) = e + \kappa(z - z_n)$$

which is illustrated in Figure 7.30(c). The neutral or reference surface is specified through the force balance

$$\sum_{i=1}^4 \int_{h_i} Y(z)\kappa(z - z_n) dz = 0 \quad (7.101)$$

which is analogous to (7.30) employed when computing the neutral surface for the unimorph. Evaluation of (7.101) yields

$$z_n = \frac{\sum_{i=1}^4 h_i^2 Y_i + 2 \sum_{i=2}^4 h_i Y_i H_i}{2 \sum_{i=1}^4 h_i Y_i}$$

where  $H_i$  is defined in (7.99).

To determine the neutral surface strain  $e$  and curvature change  $\kappa$ , forces and moments are balanced through the layers to provide the constraints

$$b \sum_{i=1}^4 \int_{h_j} \sigma dz = 0 \quad , \quad b \sum_{i=1}^4 \int_{h_j} z \sigma dz = 0$$

where

$$\sigma(z) = \left[ e + \kappa(z - z_n) - \alpha(z)\Delta T + \frac{3}{2}\nu\lambda_s\delta(z) \right] Y(z).$$

This yields the  $2 \times 2$  system

$$A\mathcal{E} = f \tag{7.102}$$

where  $\mathcal{E} = [e, \kappa]^T$  and

$$A = \begin{bmatrix} \sum_{i=1}^4 Y_i(H_i - H_{i-1}) & \sum_{i=1}^4 Y_i \left[ \frac{1}{2}(H_i^2 - H_{i-1}^2) - z_n(H_i - H_{i-1}) \right] \\ \sum_{i=1}^4 \frac{1}{2}Y_i(H_i^2 - H_{i-1}^2) & \sum_{i=1}^4 Y_i \left[ \frac{1}{3}(H_i^3 - H_{i-1}^3) - \frac{z_n}{2}(H_i^2 - H_{i-1}^2) \right] \end{bmatrix}$$

$$f = \begin{bmatrix} \sum_{i=1}^4 Y_i(\alpha_i\Delta T - 3/2\delta\nu\lambda_s)(H_i - H_{i-1}) \\ \sum_{i=1}^4 \frac{1}{2}Y_i(\alpha_i\Delta T - 3/2\delta\nu\lambda_s)(H_i^2 - H_{i-1}^2) \end{bmatrix}.$$

We note that when constructing  $A$  and  $f$ , some properties such as layer thicknesses and Young's moduli for steel and PZT can be directly measured or obtained from manufacturer specifications whereas other parameters — e.g., thermal coefficients and moduli for LaRC Si and the saturation electrostriction  $\lambda_s$  — are estimated through a least squares fit to the data.

For a given set of material properties and dimensions, solution of (7.102) yields  $e$  and  $\kappa$  and hence provides the radius of curvature

$$R = \frac{1}{\kappa}.$$

In experiments, however, one typically measures the dome height  $H_D$  depicted in Figure 7.29(b). For a transducer having flat tabs of length  $\gamma_t$  and PZT-covered region with arclength  $\gamma_s$ , it is shown in [77] that the dome height and radius of curvature are related by the expression

$$H_D = R \left[ 1 - \cos\left(\frac{\gamma_s}{2R}\right) \right] + \gamma_t \sin\left(\frac{\gamma_s}{2R}\right).$$

The performance of the model when predicting dome heights associated with various constituent materials is illustrated in [25, 77, 509].

It is noted that the previous analysis predicts a constant radius of curvature  $R$  through the region covered by PZT and flat tabs outside that region. These predictions have been experimentally validated in [491].

### Displacement Model

The previous component of the model predicts the radius of curvature  $R$  and dome height  $H_D$  as a function of material properties and manufacturing conditions. Here we construct a dynamic model by combining the relations for a curved beam having radius of curvature  $R$  and flat beam expressions for the tabs. To simplify the discussion, we make the assumption that the LaRC Si layers have negligible

effect on the dynamics and neglect their contribution. The extension of the model to include these adhesive layers is straight-forward.

To delineate the region covered by the patch, we define the characteristic function

$$\chi_{pe}(\gamma) = \begin{cases} 1 & , \quad \gamma_1 \leq \gamma \leq \gamma_2 \\ 0 & , \quad \text{otherwise} \end{cases}$$

where  $\gamma = x$  in the tabs and  $\gamma = R\theta$  in the patch region.

Under the assumption that rotational inertia and shear deformations are negligible, the longitudinal and transverse displacements  $v$  and  $w$  are quantified by the dynamic equations

$$\rho(\gamma) \frac{\partial^2 v}{\partial t^2} - \frac{\partial N_\gamma}{\partial \gamma} = 0 \tag{7.103}$$

$$\rho(\gamma) \frac{\partial^2 w}{\partial t^2} - \frac{\partial^2 M_\gamma}{\partial \gamma^2} + \frac{1}{R} N_\gamma \chi_{pe}(\gamma) = f_n$$

as specified in (7.93). Here  $f_n$  denotes applied normal loads and

$$\rho(\gamma) = \rho_I h_I + \rho_A h_A \chi_{pe}(\gamma).$$

The resultant expressions

$$N_\gamma = \int_0^{h_I} \sigma(z) dz + \int_{h_I}^{h_I+h_A} \sigma(z) dz$$

$$M_\gamma = \int_0^{h_I} z\sigma(z) dz + \int_{h_I}^{h_I+h_A} z\sigma(z) dz$$

with the constitutive relations

$$\sigma(z) = Y(z)\varepsilon + c(z)\dot{\varepsilon} - [a_1 P + a_2 P^2] \chi_{pe}(\gamma) \delta(z)$$

$$\varepsilon(z) = e + \kappa(z - z_n)$$

yields

$$N_\gamma = [Y_I h_I + Y_A h_A \chi_{pe}(\gamma)] e_\gamma + [Y_I c_1 + Y_A c_2 \chi_{pe}(\gamma)] \kappa$$

$$+ [c_I h_I + c_A h_A \chi_{pe}(\gamma)] \dot{e}_\gamma + [c_I c_1 + c_A c_2 \chi_{pe}(\gamma)] \dot{\kappa}$$

$$- h_A \chi_{pe}(\gamma) [a_1 (P(E) - P_R) + a_2 (P(E) - P_R)^2]$$

$$M_\gamma = [Y_I h_I^2/2 + Y_A c_3 \chi_{pe}(\gamma)] e_\gamma + [Y_I c_4 + Y_A c_5 \chi_{pe}(\gamma)] \kappa$$

$$+ [c_I h_I^2/2 + c_A c_3 \chi_{pe}(\gamma)] \dot{e}_\gamma + [c_I c_4 + c_A c_5 \chi_{pe}(\gamma)] \dot{\kappa}$$

$$- c_2 \chi_{pe}(\gamma) [a_1 (P(E) - P_R) + a_2 (P(E) - P_R)^2]$$

(7.104)

where

$$c_1 = \frac{H_1^2}{2} - H_1 z_n \quad , \quad c_2 = \left( \frac{H_2^2}{2} - \frac{H_1^2}{2} \right) - (H_2 - H_1) z_n$$

$$c_3 = \frac{H_2^2}{2} - \frac{H_1^2}{2} \quad , \quad c_4 = \frac{H_1^3}{3} - \frac{H_1^2}{2} z_n \quad , \quad c_5 = \left( \frac{H_2^3}{3} - \frac{H_1^3}{3} \right) - \left( \frac{H_2^2}{2} - \frac{H_1^2}{2} \right) z_n$$

and

$$H_1 = h_I \quad , \quad H_2 = h_I + h_A.$$

The nonlinear and hysteretic  $E$ - $P$  relation is quantified by (7.3) or (2.114) and the reference surface strains and curvature changes are given by

$$e_\gamma = \frac{\partial u}{\partial \gamma} + \frac{w}{R} \chi_{pe}(\gamma) \quad , \quad \kappa_\gamma = -\frac{\partial^2 w}{\partial \gamma^2}. \quad (7.105)$$

In combination, (7.103)–(7.105) provide a strong formulation of the model.

### Boundary Conditions

Recall that the transducer is assumed to have a fixed or clamped-end condition at  $\gamma = 0$  and a sliding-end condition at  $\gamma = \ell$ . This yields the boundary conditions

$$v(t, 0) = 0 \quad , \quad w(t, 0) = \frac{\partial w}{\partial \gamma}(t, 0) = 0$$

$$w(t, \ell) = v(t, \ell) \tan(\phi_I) \quad , \quad M_\gamma(t, \ell) = N_\gamma(t, \ell) = 0$$

where  $\phi_I$  denotes the initial angle at  $\gamma = \ell$  as depicted in Figure 7.30(d). As detailed in [25, 509], the condition  $N_\gamma(t, \ell)$  results from simplification of the physical constraint  $N_\gamma(t, \ell) = -Q_\gamma(t, \ell) \tan(\theta_C)$ ,  $\theta_C = \theta_I + \frac{\partial w}{\partial \gamma}$ , based upon the assumption that  $Q_\gamma$  is negligible.

### Weak Model Formulation

Consider states  $(v(t, \cdot), w(t, \cdot))$  in the state space

$$X = L^2(0, \ell) \times L^2(0, \ell).$$

The space of test functions is

$$V = \left\{ (\phi_1, \phi_2) \in H^1(0, \ell) \times H^2(0, \ell) \mid \phi_1(0) = 0, \phi_2(0) = \phi_2'(0) = 0, \right. \\ \left. \phi_2(\ell) = \phi_1(\ell) \tan(\theta_I) \right\}.$$

For all  $(\phi_1, \phi_2) \in V$ , a weak formulation of the model is

$$\int_0^\ell \left\{ \rho(\gamma) \frac{\partial^2 v}{\partial t^2} \phi_1 + N_\gamma \frac{d\phi_1}{d\gamma} \right\} d\gamma = 0 \\ \int_0^\ell \left\{ \rho(\gamma) \frac{\partial^2 w}{\partial t^2} \phi_2 + \frac{1}{R} N_\theta \phi_2 \chi_{pe}(\gamma) - M_\gamma \frac{d^2 \phi_2}{d\gamma^2} - f_n \phi_2 \right\} d\gamma = 0 \quad (7.106)$$

where  $N_\gamma$  and  $M_\gamma$  are specified in (7.104). We note that the weak formulation requires continuity of  $v, w$  and  $\frac{\partial w}{\partial \gamma}$  at the junctions  $\gamma_1$  and  $\gamma_2$  but accommodates discontinuities in higher derivatives.

### 7.9.2 Nonlinear State Dependence

The linear models developed in Section 7.9.1 should be used with caution in high drive regimes since they are based on the assumption of small displacements. To extend the framework to accommodate large displacements, which are a hallmark of the transducer, one can employ the nonlinear von Kármán theory summarized in Section 7.8.2. This includes two nonlinear effects: (i) formulation of the balance laws in terms of the deformed reference surface, and (ii) retention of quadratic terms in the strain-displacement relations.

Balancing forces and moments on the reference surface yields

$$\begin{aligned} \rho(\gamma) \frac{\partial^2 v}{\partial t^2} &= \frac{\partial N_\gamma}{\partial \gamma} - \frac{\partial}{\partial \gamma} \left[ \left( k_1 \frac{\partial^3 w}{\partial \gamma \partial t^2} + \frac{\partial M_\gamma}{\partial \gamma} \right) \frac{\partial w}{\partial \gamma} \right] \\ \rho(\gamma) \frac{\partial^2 w}{\partial t^2} &= k_1 \frac{\partial^4 w}{\partial \gamma^2 \partial t^2} - \frac{\partial^2 M_\gamma}{\partial \gamma^2} + \frac{\partial}{\partial \gamma} \left( N_\gamma \frac{\partial w}{\partial \gamma} \right) + f_n \end{aligned} \tag{7.107}$$

when relations analogous to (7.98) are used to eliminate the shear force resultant  $Q_\gamma$ . The retention of quadratic strain-displacement terms yields the reference surface strain relation

$$e_\gamma = \frac{\partial u}{\partial \gamma} + \frac{1}{2} \left( \frac{\partial w}{\partial \gamma} \right)^2 + \frac{w}{R} \chi_{pe}(\gamma) \tag{7.108}$$

which is employed in the resultant expressions (7.104).

Nonlinear models employing strain-displacement relations of the form (7.108) have been constructed in [231–233] to characterize aspects of THUNDER and RAINBOW behavior. These models, which assume uniform curvature throughout the device and linear input behavior, illustrate that inclusion of geometric nonlinearities produces a flattening in the modeled shape as compared with the linear case. The experimental validation of (7.107) with nonlinear inputs and extension of the hysteresis models to incorporate stress-induced dipole switching constitutes and active research area.

## 7.10 Abstract Model Formulation

To facilitate well-posedness analysis, convergence analysis of approximation techniques, and infinite-dimensional control design, it is advantageous to pose models in an abstract Hilbert space formulation. We illustrate this for the beam model developed in Section 7.4 and cylindrical shell model from Section 7.7.2. Detailed analysis regarding well-posedness, convergence and control criteria can be found in [33] and included references.

### 7.10.1 Beam Model

Consider the state and test function spaces

$$X = L^2(0, \ell)$$

$$V = H_0^2(0, \ell) = \{\phi \in H^2(0, \ell) \mid \phi(0) = \phi'(\ell) = 0\}$$

with the inner products

$$\langle \psi, \phi \rangle_X = \int_0^\ell \rho \psi \phi \, dx$$

$$\langle (YI)\psi, \phi \rangle_V = \int_0^\ell YI \psi'' \phi'' \, dx.$$

It is observed that  $V$  is densely and continuously embedded in  $X$  with  $|\phi|_X \leq c|\phi|_V$ ; this is expressed by  $V \hookrightarrow X$ . Moreover, when one defines conjugate dual spaces  $X^*$  and  $V^*$  — e.g.,  $V^*$  denotes the linear space of all conjugate linear continuous functionals on  $V$  — two observations are important: (i)  $X^*$  can be identified with  $X$  through the Riesz map, and (ii)  $X^* \hookrightarrow V^*$ . Hence the two spaces comprise what is termed a Gelfand triple  $V \rightarrow X \cong X^* \hookrightarrow V^*$  with pivot space  $X$  and duality pairing (duality product)  $\langle \cdot, \cdot \rangle_{V^*, V}$ . The latter is defined as the extension by continuity of the inner product  $\langle \cdot, \cdot \rangle_X$  from  $V \times X$  to  $V^* \times X$ . Hence elements  $v^* \in V^*$  have the representation  $v^*(v) = \langle v^*, v \rangle_{V^*, V}$ .

Consider the weak formulation of the model (7.39),

$$\int_0^\ell \rho \frac{\partial^2 w}{\partial t^2} \phi \, dx + \int_0^\ell \gamma \frac{\partial w}{\partial t} \phi \, dx + \int_0^\ell YI \frac{\partial^2 w}{\partial x^2} \frac{d^2 \phi}{dx^2} \, dx + \int_0^\ell cI \frac{\partial^3 w}{\partial x^2 \partial t} \frac{d^2 \phi}{dx^2} \, dx$$

$$= \int_0^\ell f \phi \, dx + [a_1(P(E) - P_R) + a_2(P(E) - P_R)^2] \int_0^\ell \frac{d^2 \phi}{dx^2} \, dx$$
(7.109)

which must hold for all  $\phi \in V$ .

#### Abstract Second-Order Formulation

We begin by defining stiffness and damping sesquilinear forms  $\sigma_i : V \times V \rightarrow \mathbb{C}$ ,  $i = 1, 2$ , by

$$\sigma_1(\psi, \phi) = \langle (YI)\psi, \phi \rangle_V$$

$$\sigma_2(\psi, \phi) = \langle (cI)\psi, \phi \rangle_V + \frac{1}{\rho} \langle \gamma \psi, \phi \rangle_X$$
(7.110)

where  $\langle (cI)\psi, \phi \rangle_V$  differs from  $\langle (YI)\psi, \phi \rangle_V$  only in the sense that the Young's modulus is replaced by the Kelvin–Voigt damping parameter. It can be directly verified that the stiffness form satisfies

- (H1)  $|\sigma_1(\psi, \phi)| \leq c_1 |\psi|_V |\phi|_V$ , for some  $c_1 \in \mathbb{R}$  (Bounded)
- (H2)  $\operatorname{Re} \sigma_1(\psi, \psi) \geq c_2 |\psi|_V^2$ , for some  $c_2 > 0$  ( $V$ -Elliptic)
- (H3)  $\sigma_1(\psi, \phi) = \overline{\sigma_1(\phi, \psi)}$  (Symmetric)

for all  $\psi, \phi \in V$ . Moreover, the damping term  $\sigma_2$  satisfies

$$(H4) \quad |\sigma_2(\psi, \phi)| \leq c_3 |\psi|_V |\phi|_V, \text{ for some } c_3 \in \mathbb{R} \quad (\text{Bounded}) \tag{7.111}$$

$$(H5) \quad \text{Re } \sigma_2(\psi, \psi) \geq c_4 |\psi|_V^2, \text{ for some } c_4 > 0 \quad (V\text{-Elliptic}).$$

The input space is taken to be the Hilbert space  $U = \mathbb{R}$  and the input operator  $B : U \rightarrow V^*$  is defined by

$$\langle [B(E)](t), \phi \rangle_{V^*, V} = [a_1[P(E(t)) - P_R] + a_2[P(E(t)) - P_R]^2] \int_0^\ell \phi'' dx. \tag{7.112}$$

It is observed that  $B$  can be expressed as

$$[B(E)](t) = [b(E)](t) \cdot g, \quad g \in V^* \tag{7.113}$$

where

$$\begin{aligned} [b(E)](t) &= [P(E(t)) - P_R] + a_2[P(E(t)) - P_R]^2 \\ g(\phi) &= \int_0^\ell \phi'' dx. \end{aligned} \tag{7.114}$$

If we let  $\tilde{f} = \frac{f}{\rho}$ , the model (7.109) can be written in the abstract variational formulation

$$\begin{aligned} \langle \ddot{w}(t), \phi \rangle_{V^*, V} + \sigma_2(\dot{w}(t), \phi) + \sigma_1(w(t), \phi) &= \langle [B(E)](t) + \tilde{f}, \phi \rangle_{V^*, V} \\ w(0) = w_0, \quad \dot{w}(0) = w_1 \end{aligned} \tag{7.115}$$

for all  $\phi \in V$ .

Alternatively, one can define the operators  $A_i \in \mathcal{L}(V, V^*)$ ,  $i = 1, 2$ , by

$$\langle A_i \phi_1, \phi_2 \rangle_{V^*, V} = \sigma_i(\phi_1, \phi_2) \tag{7.116}$$

and formulate the model in operator form as

$$\begin{aligned} \ddot{w}(t) + A_2 \dot{w}(t) + A_1 w(t) &= [B(E)](t) + \tilde{f}(t) \\ w(0) = w_0, \quad \dot{w}(0) = w_1 \end{aligned} \tag{7.117}$$

in the dual space  $V^*$ . This formulation illustrates the analogy between the infinite-dimensional, strongly damped elastic model and familiar finite-dimensional relations.

**Model Well-Posedness**

As a prelude to establishing the well-posedness of the beam model with hysteretic  $E$ - $P$  relations, we provide a lemma which quantifies the smoothness of the input operator. In the next section, this lemma is also employed when establishing the equivalence of solutions.

**Lemma 7.10.1.** *Consider continuous field inputs  $E \in C[0, T]$ . The input operator  $B$  defined by (7.112) then satisfies*

$$B(E) \in L^2(0, T; V^*). \tag{7.118}$$

*Proof.* In Appendix B.3, we establish that for continuous input fields,  $P \in C[0, T]$  which implies that  $b$  defined by (7.114) satisfies  $b(\cdot) : C[0, T] \rightarrow C[0, T]$ . Hence the norm

$$\|[B(E)](t)\|_{V^*} = \sup_{v \in V} \frac{|[b(E)](t) \cdot g(v)|}{\|v\|_V}$$

exists for each  $t \in [0, T]$ . Since  $\|[B(E)](t)\|_{V^*} = |[b(E)](t)| \cdot \|g\|_{V^*}$ , it follows that

$$\|B(E)\|_{L^2(0, T; V^*)}^2 \leq \max_{t \in [0, T]} \{|[b(E)](t)|^2\} \cdot T \cdot \|g\|_{V^*}^2$$

which implies that

$$B(E) \in L^2(0, T; V^*).$$

□

The well-posedness of the model is established by the following theorem whose proof follows directly from Theorem 4.1 of [33] or Theorem 2.1 and Remark 2.1 of [26].

**Theorem 7.10.2.** *Let  $\sigma_1$  and  $\sigma_2$  be given by (7.110) and consider continuous field inputs  $E \in C[0, T]$  and exogenous inputs  $f \in L^2(0, T; V^*)$ . There then exists a unique solution  $w$  to (7.115), or equivalently (7.117), which satisfies*

$$w \in C(0, T; V)$$

$$\dot{w} \in C(0, T; X).$$

### Abstract First-Order Formulation

We also consider an abstract first-order formulation of the model which has mild solutions defined in terms of an analytic  $C_0$ -semigroup. As detailed in Chapter 7 of [33], this provides a framework which facilitates infinite-dimensional control design and subsequent approximation.

Define the product spaces  $\mathcal{X} = V \times X$  and  $\mathcal{V} = V \times V$  with the norms

$$|(\phi_1, \phi_2)|_{\mathcal{X}}^2 = |\phi_1|_V^2 + |\phi_2|_X^2$$

$$|(\phi_1, \phi_2)|_{\mathcal{V}}^2 = |\phi_1|_V^2 + |\phi_2|_V^2$$

so that  $\mathcal{V} \hookrightarrow \mathcal{X} \cong \mathcal{X}^* \hookrightarrow \mathcal{V}^*$  again forms a Gelfand triple with  $\mathcal{V}^* = V \times V^*$ . The state is  $z(t) = (w(t, \cdot), \dot{w}(t, \cdot)) \in \mathcal{X}$ . Letting  $\Phi = (\phi_1, \phi_2)$  and  $\Psi = (\psi_1, \psi_2)$ , the sesquilinear form  $\sigma : \mathcal{V} \times \mathcal{V} \rightarrow \mathbb{C}$  is defined by

$$\sigma(\Psi, \Phi) = -\langle \psi_2, \phi_1 \rangle_V + \sigma_1(\psi_1, \phi_2) + \sigma_2(\psi_2, \phi_2)$$

and the product space forcing terms are formulated as

$$\mathcal{F}(t) = \begin{bmatrix} 0 \\ \tilde{f}(t) \end{bmatrix}, \quad [\mathcal{B}(E)](t) = \begin{bmatrix} 0 \\ [(B(E))](t) \end{bmatrix}.$$

The weak model formulation (7.117) can then be written as the first-order relation

$$\langle \dot{z}(t), \Phi \rangle_{\mathcal{V}^*, \mathcal{V}} + \sigma(z(t), \Phi) = \langle [\mathcal{B}(E)](t) + \mathcal{F}(t), \Phi \rangle_{\mathcal{V}^*, \mathcal{V}}$$

for  $\Phi \in \mathcal{V}$ . Formally, this equivalent to the strong formulation

$$\begin{aligned} \dot{z}(t) &= \mathcal{A}z(t) + [\mathcal{B}(E)](t) + \mathcal{F}(t) \quad \text{in } \mathcal{V}^* \\ z(0) &= z_0 = \begin{bmatrix} w_0 \\ w_1 \end{bmatrix} \end{aligned} \tag{7.119}$$

where the operator  $\mathcal{A}$  is given by

$$\begin{aligned} \text{dom} \mathcal{A} &= \{(\phi_1, \phi_2) \in \mathcal{X} \mid \phi_2 \in V, A_1 \phi_1 + A_2 \phi_2 \in X\} \\ \mathcal{A} &= \begin{bmatrix} 0 & I \\ -A_1 & -A_2 \end{bmatrix}. \end{aligned} \tag{7.120}$$

In a manner analogous to (7.116),  $\mathcal{A}$  can be related to the operator  $\tilde{\mathcal{A}} \in \mathcal{L}(\mathcal{V}, \mathcal{V}^*)$  defined by

$$\langle \tilde{\mathcal{A}}\Psi, \Phi \rangle_{\mathcal{V}^*, \mathcal{V}} = \sigma(\Psi, \Phi).$$

Specifically,  $\mathcal{A}$  is the negative of the restriction to  $\text{dom} \mathcal{A}$  of  $\tilde{\mathcal{A}}$  so that  $\sigma(\Psi, \Phi) = \langle -\mathcal{A}\Psi, \Phi \rangle_{\mathcal{X}}$  for  $\Psi \in \text{dom} \mathcal{A}$ ,  $\Phi \in \mathcal{V} \subset \mathcal{X}$ .

The formulation (7.119) with  $\mathcal{A}$  defined by (7.120) is formally analogous to the first-order formulation of finite-dimensional second-order systems.

Due to the presence of Kelvin–Voigt damping which causes  $\sigma_2$  to satisfy the  $V$ -ellipticity and  $V$ -continuity conditions (H4) and (H5) of (7.111), it is established in Chapter 4 of [33] that  $\sigma$  is  $\mathcal{V}$ -elliptic and  $\mathcal{A}$  generates an analytic semigroup  $\mathcal{T}(t)$  on  $\mathcal{V}, \mathcal{X}$  and  $\mathcal{V}^*$ .<sup>34</sup> From Lemma 7.10.1, it follows that  $B(E) \in L^2(0, T; V^*)$  and hence  $\mathcal{B} \in L^2(0, T; \mathcal{V}^*)$ . Under the assumptions that  $z_0 \in \mathcal{V}^*$  and  $\mathcal{F} \in L^2(0, T; \mathcal{V}^*)$ , a mild solution to (7.119) is given by

$$z(t) = \mathcal{T}(t)z_0 + \int_0^t \mathcal{T}(t-s) ([\mathcal{B}(E)](s) + \mathcal{F}(s)) ds. \tag{7.121}$$

It is illustrated in Section 4.4 of [33] that under these conditions, the mild and weak solutions are equivalent.

<sup>34</sup>The domain defined in (7.120) is actually  $\text{dom}_{\mathcal{X}} \mathcal{A}$ . However, the use of one symbol when denoting semigroups or infinitesimal generators defined on each of the spaces in a Gelfand triple is common in the literature and does not cause ambiguity.

**Remark 7.10.3.** *In the case of weaker damping (e.g., air damping), weakened conditions (H4') and (H5') must be considered which leads to the generation of a  $C_0$ -semigroup  $\mathcal{T}(t)$  on  $\mathcal{X}$  that is not analytic. To accommodate inputs in  $\mathcal{V}^*$ , it is necessary to extend the semigroup to a larger space  $\mathcal{W} = [\text{dom}\mathcal{A}^*]^* \supset \mathcal{V}^*$  using extrapolation space techniques similar to those used by DaPrato and Grisvard [121], Haraux [208] and Weissler [508]. Details regarding this extension and resulting equivalence of solutions can be found in [27, 33].*

### 7.10.2 Shell Model

To illustrate the generality of this approach, we also summarize the abstract formulation of the cylindrical shell model developed in Section 7.7.2. We consider fixed boundary conditions

$$u = v = w = \frac{\partial w}{\partial x} = 0$$

at  $x = 0$  and free end conditions

$$N_x = N_{x\theta} + \frac{M_{x\theta}}{R} = M_x = Q_x + \frac{1}{R} \frac{\partial M_{x\theta}}{\partial \theta} = 0$$

at  $x = \ell$ .

We consider the state  $\xi(t) = (u(t, \cdot, \cdot), v(t, \cdot, \cdot), w(t, \cdot, \cdot))$  in the state space

$$X = L^2(\Omega) \times L^2(\Omega) \times L^2(\Omega)$$

$$\langle \psi, \phi \rangle_X = \int_{\Omega} \rho h \psi_1 \bar{\phi}_1 d\omega + \int_{\Omega} \rho h \psi_2 \bar{\phi}_2 d\omega + \int_{\Omega} \rho h \psi_3 \bar{\phi}_3 d\omega$$

where  $\Omega = [0, \ell] \times [0, 2\pi]$  and  $\psi = (\psi_1, \psi_2, \psi_3)$ ,  $\phi = (\phi_1, \phi_2, \phi_3)$ .<sup>35</sup> The space of test functions is

$$V = H_0^1(\Omega) \times H_0^1(\Omega) \times H_0^2(\Omega)$$

$$\begin{aligned} \langle (Y)\psi, \phi \rangle_V &= \int_{\Omega} \frac{Yh}{1-\nu^2} \left[ (e_x + \nu e_{\theta}) \frac{\bar{\partial\phi_1}}{\partial x} + \frac{1}{2R} (1-\nu) e_{x\theta} \frac{\bar{\partial\phi_1}}{\partial \theta} \right] d\omega \\ &+ \int_{\Omega} \frac{Yh}{1-\nu^2} \left[ (e_{\theta} + \nu e_x) \frac{1}{R} \frac{\bar{\partial\phi_2}}{\partial \theta} + \frac{1}{2} (1-\nu) e_{x\theta} \frac{\bar{\partial\phi_2}}{\partial x} \right] d\omega \\ &+ \int_{\Omega} \frac{Yh}{1-\nu^2} \left[ \frac{1}{R} (e_{\theta} + \nu e_x) \bar{\phi}_3 - \frac{h^2}{12} (\kappa_x + \nu \kappa_{\theta}) \frac{\bar{\partial^2\phi_3}}{\partial x^2} \right. \\ &\quad \left. - \frac{h^2}{12R^2} (\kappa_{\theta} + \nu \kappa_x) \frac{\bar{\partial^2\phi_3}}{\partial \theta^2} - \frac{h^2}{12R} (1-\nu) \kappa_{x\theta} \frac{\bar{\partial^2\phi_3}}{\partial x \partial \theta} \right] d\omega. \end{aligned}$$

<sup>35</sup>As detailed in [130], retention of the complex conjugate in the inner product is necessary when implementing approximation techniques employing complex Fourier bases.

where  $H_0^1(\Omega)$  and  $H_0^2(\Omega)$  are defined in (7.91) and the reference surface strains and changes in curvature are defined in (7.90). We now summarize the abstract formulation of the model (7.92).

As with the beam model, we define sesquilinear forms

$$\begin{aligned}\sigma_1(\psi, \phi) &= \langle (Y)\psi, \phi \rangle_V \\ \sigma_2(\psi, \phi) &= \langle (c)\psi, \phi \rangle_V\end{aligned}$$

which incorporate the stiffness and damping components. The input operator  $B : U \rightarrow V^*$  is defined by

$$\begin{aligned}\langle [B(E)](t), \phi \rangle_{V^*, V} &= a_1 [P(E(T)) - P_R] \frac{h}{1-\nu} \int_{\Omega} \left\{ \frac{\overline{\partial\phi_1}}{\partial x} + \frac{1}{R} \frac{\overline{\partial\phi_2}}{\partial\theta} \right\} d\omega \\ &+ a_2 [P(E(t)) - P_R]^2 \frac{h}{1-\nu} \int_{\Omega} \left\{ \frac{\overline{\partial\phi_1}}{\partial x} + \frac{1}{R} \frac{\overline{\partial\phi_2}}{\partial\theta} \right\} d\omega.\end{aligned}$$

The weak formulation can subsequently be posed as

$$\left\langle \ddot{\xi}(t), \phi \right\rangle_{V^*, V} + \sigma_2(\dot{\xi}(t), \phi) + \sigma_1(\xi(t), \phi) = \langle [B(E)](t) + \widehat{f}, \phi \rangle_{V^*, V}$$

where  $\widehat{f} = \frac{1}{\rho h}(f_x, f_y, f_n)$ . This is the same general abstract variational formulation for second-order systems that was considered in (7.115) for the beam and the remainder of the formulation follows that described in the context of the beam model.